Implementing hybrid ultrasound modalities for high-intensity focused ultrasound monitoring

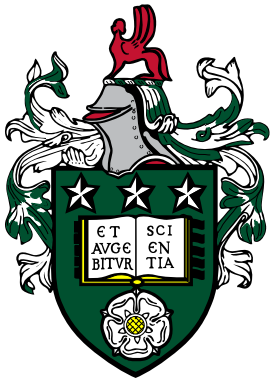

Chunqi Li

Institute of Robotics, Autonomous Systems, and Sensing
School of Electronic and Electrical Engineering
The University of Leeds

Submitted in accordance with the requirements for the degree of

Doctor of Philosophy

July 2022

The PGR confirms that the work submitted is their own, except where work which has formed part of jointly authored publications has been included. The contribution of the PGR and the other authors to this work has been explicitly indicated below. The PGR confirms that appropriate credit has been given within the thesis where reference has been made to the work of others.

Journal paper

Chunqi Li, Harry R Clegg, Thomas M Carpenter, Luzhen Nie, David MJ Cowell, Steven Freear, James R McLaughlan. 'Evaluation of PAM beamformers for high-duty-cycle HIFU applications.' *(UFFC submission).*

Chunqi Li, Harry R Clegg, Thomas M Carpenter, David MJ Cowell, Steven Freear, James R McLaughlan. 'Spectrum equalised beamforming for the interlaced B-mode suffering HIFU interference.' *(In preparation).*

I was responsible for the entirety of these first-author manuscripts including conceptualization, methodology, signal processing, investigation, data curation, writing. Harry R Clegg, Thomas M Carpenter, Luzhen Nie and David MJ Cowell were responsible for the ultrasound hardware and software, and manuscript editing. James R McLaughlan and Steven Freear supervised the project.

Conference paper and presentations

Chunqi Li, Harry R Clegg, Thomas M Carpenter, Luzhen Nie, Steven Freear, David MJ Cowell, James R McLaughlan. Modified passive acoustic mapping with diagnostic-array angular response for cavitation monitoring during HIFU ablation in ex vivo tissue. *2020 IEEE International Ultrasonics Symposium (IUS)* .

Chunqi Li, Harry R Clegg, Thomas M Carpenter, Luzhen Nie, Steven Freear, David MJ Cowell, James R McLaughlan. Apodizing delay and auto-correlation reconstruction algorithm for high-frame-rate ultrasound imaging. *2020 IEEE International Ultrasonics Symposium (IUS).*

Chunqi Li, Harry R Clegg, Thomas M Carpenter, Luzhen Nie, Steven Freear, David MJ Cowell, James R McLaughlan. Mutual convolution of dual modes to enhance passive acoustic mapping for high duty-cycle HIFU exposures monitoring. *2021 IEEE International Ultrasonics Symposium (IUS).*

Chunqi Li, Harry R Clegg, Thomas M Carpenter, Luzhen Nie, Steven Freear, David MJ Cowell, James R McLaughlan. Polar coordinate coherent passive acoustic beamforming for

the modifiable improvement of image quality and field of view. *2021 IEEE International Ultrasonics Symposium (IUS).*

Chunqi Li, Harry R Clegg, Thomas M Carpenter, Steven Freear, David MJ Cowell, James R McLaughlan. The dynamic F-number and shading weights determined by element directivity for passive acoustic mapping. *2022 IEEE International Ultrasonics Symposium (IUS).*

Chunqi Li, Harry R Clegg, Thomas M Carpenter, Steven Freear, David MJ Cowell, James R McLaughlan. Power spectrum equalized passive acoustic mapping. *2022 IEEE International Ultrasonics Symposium (IUS).*

I was responsible for the entirety of these first-author publications including conceptualization, methodology, signal processing, investigation, data curation, writing. Harry R Clegg, Thomas M Carpenter, Luzhen Nie and David MJ Cowell were responsible for the ultrasound hardware and software, and manuscript editing. James R McLaughlan and Steven Freear supervised the project.

Conference abstract and presentations

Chunqi Li, Harry R Clegg, Thomas M Carpenter, Luzhen Nie, Steven Freear, David MJ Cowell, James R McLaughlan. Interleaving passive acoustic mapping with compounded diverging-wave imaging for HIFU treatment monitoring. *2019 The British Medical Ultrasound Society (BMUS).*

I was responsible for conceptualization, methodology, signal processing, investigation, data curation, writing. Harry R Clegg, Thomas M Carpenter, Luzhen Nie and David MJ Cowell were responsible for the ultrasound hardware and software, and abstract editing. James R McLaughlan and Steven Freear supervised the project.

Chapter 2, the results in section 2.2 and section 2.3 that were partially published in BMUS abstract (2019). The power spectrum equalised techniques presented in section 2.4 for B-mode were introduced into passive acoustic mapping for further verification and being accepted by IUS conference (2022).

Chunqi Li, Harry R Clegg, Thomas M Carpenter, Luzhen Nie, Steven Freear, David MJ Cowell, James R McLaughlan. Interleaving passive acoustic mapping with compounded diverging-wave imaging for HIFU treatment monitoring. *2019 The British Medical Ultrasound Society (BMUS).*

Chunqi Li, Harry R Clegg, Thomas M Carpenter, Steven Freear, David MJ Cowell, James R McLaughlan. Power spectrum equalized passive acoustic mapping. *2022 IEEE International Ultrasonics Symposium (IUS).*

Chapter 3, the main results of PAM beamformers were firstly published in BMUS abstract (2019), and developed into journal paper (UFFC submission).

Chunqi Li, Harry R Clegg, Thomas M Carpenter, Luzhen Nie, Steven Freear, David MJ Cowell, James R McLaughlan. Interleaving passive acoustic mapping with compounded diverging-wave imaging for HIFU treatment monitoring. *2019 The British Medical Ultrasound Society (BMUS).*

Chunqi Li, Harry R Clegg, Thomas M Carpenter, Luzhen Nie, Steven Freear, David MJ Cowell, James R McLaughlan. 'Evaluation of PAM beamformers for high-duty-cycle HIFU applications.' *(UFFC submission).*

Chapter 4, the idea about element directivity was originated from Chunqi Li's two IUS conference papers (2020), then summarised and developed into TEA based PAM, and being accepted by the IUS conference (2022).

Chunqi Li, Harry R Clegg, Thomas M Carpenter, Luzhen Nie, Steven Freear, David MJ Cowell, James R McLaughlan. Modified passive acoustic mapping with diagnostic-array angular response for cavitation monitoring during HIFU ablation in ex vivo tissue. *2020 IEEE International Ultrasonics Symposium (IUS)* .

Chunqi Li, Harry R Clegg, Thomas M Carpenter, Luzhen Nie, Steven Freear, David MJ Cowell, James R McLaughlan. Apodizing delay and auto-correlation reconstruction algorithm for high-frame-rate ultrasound imaging. *2020 IEEE International Ultrasonics Symposium (IUS).*

Chunqi Li, Harry R Clegg, Thomas M Carpenter, Steven Freear, David MJ Cowell, James R McLaughlan. The dynamic F-number and shading weights determined by element directivity

for passive acoustic mapping. *2022 IEEE International Ultrasonics Symposium (IUS)*.

Chapter 5, the results were first published in Chunqi Li's two IUS conference papers (2021), then summarized and developed into one chapter.

Chunqi Li, Harry R Clegg, Thomas M Carpenter, Luzhen Nie, Steven Freear, David MJ Cowell, James R McLaughlan. Mutual convolution of dual modes to enhance passive acoustic mapping for high duty-cycle HIFU exposures monitoring. *2021 IEEE International Ultrasonics Symposium (IUS)*.

Chunqi Li, Harry R Clegg, Thomas M Carpenter, Luzhen Nie, Steven Freear, David MJ Cowell, James R McLaughlan. Polar coordinate coherent passive acoustic beamforming for the modifiable improvement of image quality and field of view. *2021 IEEE International Ultrasonics Symposium (IUS)*.

Acknowledgements

This thesis would not exist without the support from our teamwork. I would therefore like to express my sincerest gratitude for all my collaborators.

First and foremost, appreciate for my supervisor Dr. James McLaughlan who provides his continuous guidance and support for my PhD research. Also, many thanks to my supervisor Prof. Steven Freear for his encouragement and help.

My grateful thanks extends to Dr. David Cowell, Dr. Thomas Carpenter and Mr Harry Clegg and everyone else who contributed to the excellent house develop ultrasound platform. Without that, the HIFU monitoring trigger system would not be so perfect.

I am profoundly grateful to my teammates, Dr. Luzhen Nie, Dr. Chris Adams, Dr. Oscar Knights, Dr. Abdulrhman Alshaya, Dr. Asraf Mohamed, Mr Elliott Smith and anyone else I may forget to mention their names, for their accompany and innumerable valuable academic discussions that inspired me a lot on my research.

My heartfelt thanks go to my parents. Thanks for your highest patience, support through the sleepless four years' time of my Ph.D.. Without your spiritual encouragement, I could not be who I am today.

If your friend does not talk with you at all and all his social media has not been updated for a very long time.

Please do not call the police, he is just struggling on the way to finishing his Ph.D. degree, particularly in engineering.

To memorise my past nine years' youthfulness in the acoustic/ultrasound field.

Abstract

High-intensity focused ultrasound (HIFU) therapy is an emerging and versatile technique for clinical non/mini-invasive treatment. Ultrasound methods for HIFU therapy guidance, due to its readily available and cheaper advantages over MRI, that has been intensively explored as a promising technology. This thesis mainly focused on the investigation of a designed hybrid pulse sequence to perform HIFU therapy, and implement its whole journal monitoring via passive acoustic mapping (PAM) and interlaced high frame rate B-mode. For the dual ultrasound modalities, efforts have been devoted to advanced algorithms with computation efficacy to improve the contrast to noise ratio for hyperechogenicity displaying (B-mode) and the source localisation capability (PAM).

In the first contributing chapter, several parameters and factors were firstly investigated on the gel phantoms, and being monitored by interlaced B-mode and passive cavitation detection, such as the optimal duty cycle (95%) of the hybrid pulse sequence and the efficient B-mode modality via phased array. Meanwhile, the power spectrum equalized technique was proposed to decolor the re-aligned data into whiten domain for interlaced B-mode beamforming, and demonstrated an improvement in CNR and CR approximately 69% and 125% increase over the Delay Multiply and Sum (DMAS) algorithm, respectively.

In the second contributing chapter, the DC components generated from the system and passive beamforming process which can be recursively accumulated into great background noise. Therefore, the DC components subtraction was considered in the time-domain Robust Capon beamformer, aim at improving cavitation localization capability. Meanwhile, kinds of techniques were developed into PAM beamformers and illustrated with proposed methods such as eigen-subspace and scaled Wiener. Final experimental results from both BSA and *ex vivo* livers phantoms demonstrated an 86%-94% noise area suppression is achieved by the proposed method, compared to the time exposure acoustic (TEA) algorithm.

In the third contributing chapter, to complement experimental studies, a simulator was built based on the coated-model to provide standardised data for the quantitative analyse of PAM. Then, a pixel-wise F-number and shading weight

(DFSW) strategy was developed from the soft-baffle element directivity model that was introduced into PAM beamforming. Final simulated and experimental results illustrate that the DFSW strategy could improve the PAM image quality, particularly in the near-field with approximately 6 dB enhancement.

In the final contributing chapter, a more clinically relevant HIFU system, with therapeutic and imaging transducers co-aligned was used to evaluate the polar coordinate PAM for a competent monitored field of view, whilst, a mutual convoluted strategy between interlaced B-mode and PAM was developed to improve the PAM image quality. All of these aforementioned techniques were to improve the localisation/imaging of cavitation activity from high duty cycle HIFU exposures, the promising future direction about presented jobs is to monitor the applications such as microbubble drug delivery or microbubble mediated blood-brain barrier opening .etc as the next step.

Contents

List of Tables

List of Figures

List of Acronyms

A-mode Amplitude mode. 1

ARFI Acoustic Radiation Force Impulse. 13

B-mode Brightness mode. 1

BBB Blood–Brain Barrier. 11

CDWI Coherent Divergent Wave Imaging. 39

CEM Cumulative Equivalent Minutes. 7

CPWI Compound Plane Wave Imaging. 39

CT Computation Time. 105

DFSW Dynamic F-number and Shading Weight. 121

DMAS Delay-Multiply-And-Sum. 53

DWI Divergent Wave Imaging. 39

E-RCB Eigensubspace RCB. 83

ED Element Directivity. 121

FOV Field Of View. 38

GPU Graphics Processing Unit. 16

HIFU High-Intensity Focused Ultrasound. 2

ICD Inertial Cavitation Dose. 47

LI Linear Imaging. 39

MRgFUS MRI-guided focused ultrasound surgery. 10

PAM Passive Acoustic Mapping. 10

qCW quasi-Continuous Wave. 83

RCB Robust Capon Beamformer. 83

RCB-DC Robust Capon beamformer with DC reduction. 83

UARP Ultrasound Array Research Platform. 40

WE-RCB Wiener E-RCB. 83

Chapter 1

Introduction

1.1 Minimally invasive therapeutic ultrasound

Ultrasound is the sound or other propagating perturbations to compress and rarefy the medium with the longitudinal pressure (above frequencies of 20 kHz) which has been widely used for diagnostic imaging and therapy (Dictionary, 1989; Leighton, 2007). Over the years, the clinical use of ultrasound for medical diagnosis has witnessed continuous growth (Mason et al., 2005). In the early stages of diagnostic ultrasound, Amplitude mode (A-mode) ultrasonography was applied by a scanning line through the tissue with the echoes displayed on the monitor as a function of depth, and also used for therapeutic ultrasound aimed at specific tumour or calculus to allow for pinpoint accurate focus of the sonification wave energy Goldberg and Lehman (1969). Then, this technique was developed into two dimensions with Brightness mode (B-mode) techniques which composed of bright anatomical information representing the envelope detected ultrasound echoes with real-time high performance Ramalli et al. (2018); Sullivan et al. (1984). The range of current applications for modern ultrasound diagnostic techniques is very wide, including elastography measurements of the stiffness of tissues Tan et al. (2008), two-dimensional (2D)/three-dimensional (3D) monitoring of cavitation activities in the moving tissue structure Escudero et al. (2018) and Doppler imaging of blood flow measurements Hernandez-Andrade et al. (2004).

Improvements in ultrasound techniques, including diagnostic systems and signal processing theories, have accelerated the widespread acceptance of ultrasound as one of the most popular clinical imaging modalities Whittingham (2007). The cost-effectiveness and portability of diagnostic ultrasound systems, along with their

real-time features and non-ionising character, also contribute to the comparative advantages of ultrasound techniques over computerised tomography (CT), magnetic resonance imaging (MRI) and X-ray in clinical adoption.

The applications of using medical ultrasound for diagnostic imaging, which was quickly developed into a different area about high-intensity ultrasound for therapy. The history of high-intensity ultrasound therapy can be traced to the early 1940s. Lynn et al. first reported that focused ultrasound can effectively destroy the target region without affecting the surrounding tissue Lynn et al. (1942). Then, the years since the 1950s have seen the development of focused ultrasound surgery as a non-invasive/minimally invasive treatment technology that uses non-ionising ultrasound waves to heat and damage cancerous tissue ter Haar and Coussios (2007); Ter Haar (2001); Zhou (2011). This method has been applied in clinical surgery and has the potential to replace traditional technology in the treatment of a variety of diseases, especially for cancer Maloney and Hwang (2015); Ter Haar (2007); Ter Haar et al. (2009). The main application in acoustic therapy is the High-Intensity Focused Ultrasound (HIFU), which utilises the physical characteristics of ultrasound, such as the constructive interference between the pressure waves, to concentrate the ultrasonic energy in the focal region. HIFU generally satisfies the specifications of high intensity (1000–10000 W/cm^2), high acoustic power (100–1000 W) and strong focus (100–1000 gain) in the target area Vaezy et al. (2001). During the ultrasound based therapy process, the transient temperature inside the focal region can be above 56°C, resulting in irreversible coagulative necrosis Sibille et al. (1993). In the 1960s, Fry et al. applied acoustic therapy in the field of neurosurgery for the surgical treatment of exposed cancerous brain tissue Fry and Hyatt (1960). Consequently, unlike the ultrasound imaging techniques, the advances in HIFU has been developed relatively slow due to the concerns about treatment monitoring and successful execution, more specifically, such as for the accurate targeting and therapeutic planning, quantitative analysing of ultrasound energy conversion and treatment monitoring.

From the 1970s, the capability of high-intensity ultrasound therapy was improved with the help of more advanced techniques in transducer materials and designs, allowing more versatile research such as in the fields of neuromodulation Khokhlova et al. (2014) and cancer therapy Kremkau (1979). Since then, with further development related to ultrasound techniques in the field of monitoring, hardware system and signal processing, the application of therapeutic ultrasound extended into wider areas, including targeted drug-loading and delivery for solid

tumours in cancer therapy Dromi et al. (2007); Frenkel (2008); Grüll and Langereis (2012); Ranjan et al. (2012), thermal ablation for tumours Diederich (2005); Köhler et al. (2009); Maloney and Hwang (2015), blood-brain barrier disruption Baseri et al. (2010); Hynynen et al. (2001); McDannold et al. (2008) and opening Bing et al. (2009); Hynynen et al. (2003); O'Reilly et al. (2011); Zhao et al. (2018), and histotripsy and lithotripsy with cavitation bio-effects Khokhlova et al. (2015); Maxwell et al. (2011); Wang et al. (2011); Xu et al. (2007). However, in order to translate the ultrasound therapies into clinical more efficiently. More efforts should be paid on the therapeutic monitoring and quantitative analysing the relationship between acoustic feedback information and lesion performance, therefore to control for the treatment efficacy and minimising the unwanted effects.

1.2 Ultrasound bio-effects

The interactions between tissue and propagated ultrasound can result in various mechanisms that cause the beneficial or detrimental features McLaughlan et al. (2010a). In this section, a review of the physical principles about different ultrasound mechanisms along with their associated bio-effects are illustrated.

1.2.1 The ultrasound basics

Nonlinearity

In high-intensity ultrasound applications, nonlinear wave propagation is prevalent. The instantaneous velocity in a compressible medium can be affected by the ratio of particle velocity (u) to the speed of the pressure wave (c), then the positive particle velocity (in the direction of wave propagation) tends to be (c + u), i.e., faster than the part of the waveform travelling in the opposite direction with negative particle velocity (attained with the rarefactional phase) (the schematic process was shown in Figure 1.1 McLaughlan (2008)). Through this process, the original sinusoidal waveform can be deformed and displayed in a 'saw-tooth' geometry which termed as the shockwave Gallego-Juárez (2017). The distance for the distortion of the sinusoidal waveform into shockwave (named as shockwave formation distance x) which can be expressed as:

$$\mathrm{x} = \frac{1}{\beta \mathrm{kM}}. \tag{1.1}$$

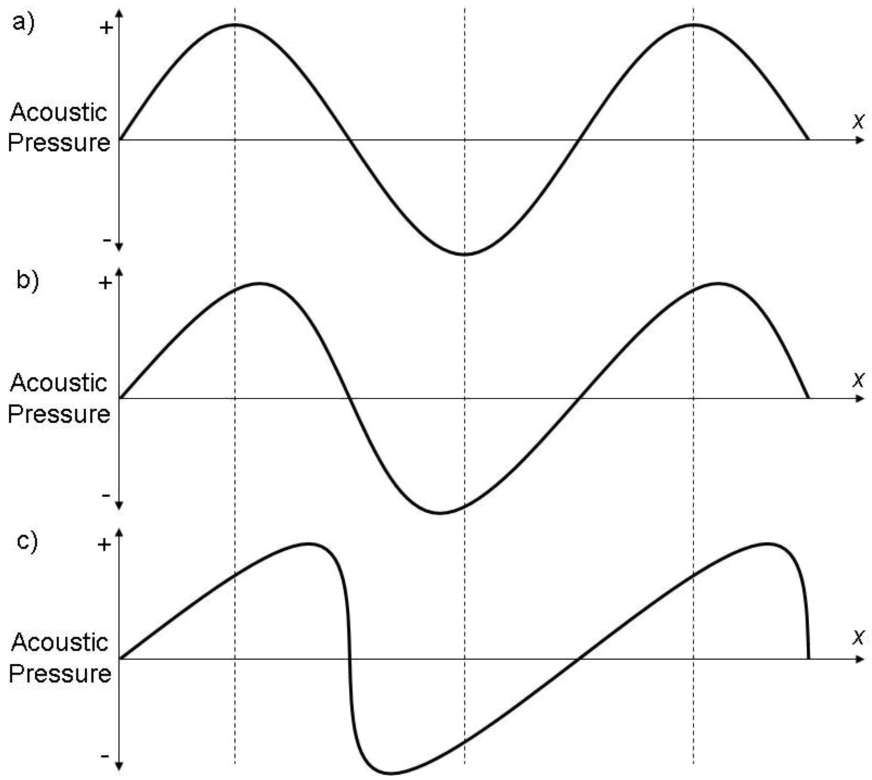

Figure 1.1: A schematic diagram of the development of a 'saw-tooth' from an initially sinusoidal waveform. The waveforms (a), (b) and (c) show the distortion of the wave as it propagates in a medium at increasing distances from the acoustic source.

where M is acoustic Mach number that is equal to $p_0/(\rho_0 c^2)$, the p_0 is the source pressure amplitude, ρ_0 is density of the medium and c is the speed of sound in the medium. β is the nonlinearity coefficient of the propagation path, k is the angular wavenumber of the sinusoidal waveform and being defined as $2\pi/\lambda$, where λ is the wavelength of the waveform. In addition to the impact of propagation distance, the distortion degree of the propagating waveform also increases with signal amplitude, centre frequency and the nonlinearity coefficient of the medium $\frac{B}{A}$, where the values of A and B are the coefficients of the first- and second-order terms of the Taylor series expansion equation Beyer (1975). Moreover, the nonlinearity feature can spread the fundamental ultrasound energy into higher harmonics Kashcheeva et al. (2000). Consequently, the higher harmonics can be more readily attenuated and increases the possibility of pre-focal energy deposition over linear estimations Vaezy et al. (2001). The nonlinearity-related attenuation can have great implications both for the detection and mapping of cavitation activities occurring in ultrasound therapies, as the interested components of acoustic signal being detected for monitoring purposes can be greatly attenuated, such as for the broadband information used for inertial cavitation mapping.

Attenuation

Attenuation in ultrasound is the reduction in energy of the propagating beam as a function of distance through viscoelastic media Duck et al. (2020). A variety of factors can contribute to the attenuation phenomenon including absorption, scattering, reflection, refraction and beam divergence.

(1) The absorption of wave propagation is the conversion of mechanical energy into heat, resulting from macromolecular relaxation, thermal conductivity and viscous loss processes Pauly and Schwan (1971).

(2) Scattering, or reflection, occurs when ultrasound beams strike a structure with a different acoustic impedance of the adjoining tissues Laugier and Haïat (2011); Sehgal and Greenleaf (1984). The difference between scattering and reflection, which is the reflection (specular), indicates whether the surface is smooth by comparing with the ultrasound wavelength, and scattering emerges with irregularities in the surface, and the irregularities are similar to the ultrasound wavelength.

(3) Refraction occurs when the ultrasound wave travels between layers of different density or elasticity, generating different propagation speeds, and the divergence is the spreading out of the ultrasound beam Craster and Guenneau (2012); Jensen (1996).

Of these processes, absorption is usually considered as the dominant one when accounting for the loss of acoustic energy; thus, absorption is commonly used in energy loss estimation.

The level of attenuation (absorption) is a frequency-dependent parameter due to the scale of tissue structure dynamically changing relative to the ultrasound wavelength. Consequently, attenuation can have greater heat deposition when increase the centre frequency, and will be difficult in propagating deeply. For the B-mode (pulse-echo), attenuation occurs in both directions, while for the passive 'listening' mode, attenuation occurs only on the receiving journey. To compensate for the energy loss, the imaging platform usually has a time gain compensation or depth gain compensation control, allowing amplification modification of the weaker emissions received from deeper within the body. The magnitude of attenuation also depends on the propagation distance and tissue characteristics that the sound propagates through. For example, as the molecules of the bone are densely packed, energy loss due to attenuation will be greater in bone than in fat, which is less densely packed. To approximate the attenuated incident ultrasonic energy in the case of plan wave propagating in the x direction (illustrate as x_b), the modified solution of wave equation considering an exponential decrease in the signal amplitude with distance that can be expressed as:

$$\mathrm{p(x_b, t) = Pe^{-\alpha x_b} cos(wt - kx_b)}. \tag{1.2}$$

α (Np/m) is the frequency-dependent amplitude attenuation coefficient, where Np is the neper (1 Np is approximately 8.686 dB). In soft tissue, α is proportional to f^m, where $1 < m < 2$. For most applications of diagnostic ultrasound, m is approximately 1 Hoskins et al. (2019).

1.2.2 Ultrasound-induced thermal mechanisms

Thermal effects indicate the conversion of acoustic energy to heat due to the mechanisms of heat conduction, convection and perfusion Suslick and Nyborg (1990). The dominant mechanism causing the thermal effect is attenuation, which mainly results from absorption and scattering. Besides the impact from tissue characteristics, the thermal performance also depends on the HIFU exposure parameters (e.g. intensity, duration and duty cycle) Ebbini and Ter Haar (2015). The thermal heating energy deposition per unit volume and time is represented by Q Clarke and Ter Haar (1997); Pierce and Beyer (1990), which can be estimated by the

absorbed sound power density for (and only for) the case of plane wave field:

$$Q = 2I_0\varepsilon(f). \tag{1.3}$$

where I_0 is the acoustic intensity and $\varepsilon(f)$ is the frequency-dependent attenuation coefficient. Equation 1.3 is feasible only when the exposure is a plane wave with constant angular frequency. Due to the absorption plays a main role in attenuation, the frequency-dependent attenuation coefficient $\varepsilon(f)$ can be approximated by absorption coefficients Hill et al. (2004).

Nonlinear propagation, as aforementioned, is an important effect for thermal deposition, due to the high-intensity ultrasound energy can be transferred to higher harmonics; therefore, each of higher harmonic component can more readily contribute to heating and be absorbed at different rates. This process can cause inhomogeneous tissue ablation and increase the possibility of the overlying tissue being over-heated, particular when the focal zone targets on a medium with different properties Bacon and Carstensen (1990); McLaughlan et al. (2010a). When the thermal-induced temperature in the tissue exceeds 43°C, a variety of bio-effects would be encountered. The subsequent tissue damage can be reversible or irreversible, depending on the parameters, including the rate of temperature increase and the ablative duration. Under specific conditions, e.g. when the temperature of the focal zone is greater than 45°C and with 1 s of HIFU duration, coagulative necrosis can occur almost instantly Vaezy et al. (2001). The temperature evolution within the focal zone can be adequately described by Pennes' transient bioheat transfer equation Kolios et al. (1998). The thermal dose parameter Cumulative Equivalent Minutes (CEM) describes the cumulative thermal effects for hyperthermia therapy at equivalent exposure times with reference temperatures 43°C, which is widely used to assess the clinically relevant thermal damage Beik et al. (2016); Sapareto and Dewey (1984),

1.2.3 Cavitation effects and mechanical mechanisms

A variety of mechanical effects are involved in ultrasound therapy, including acoustic streaming, radiation pressure and cavitation Nyborg (2001). Acoustic cavitation as the dominant therapeutic mechanical mechanism that was illustrated in this section.

The term 'acoustic cavitation' refers to activities associated with air or gas bubbles, pockets and cavities under excitations of acoustic waves Thornycroft

and Barnaby (1895). More specifically, acoustic cavitation can be the gas pocket formed through exsolution and rectified diffusion .etc Wu and Nyborg (2008) or the growth and collapse of pre-existing bubbles (such as the contrast agent) Ashokkumar (2011). Acoustic cavitation has been demonstrated to have a strong relationship with many bio-effects, including opening or disrupting the blood–brain barrier Tung et al. (2010), histotripsy or lithotripsy for mechanical tissue fractionation Lingeman et al. (2009); Roberts (2014), thermal necrosis coagulation Yoshizawa et al. (2017) and enhancing therapeutic efficacy Coussios et al. (2007); Coussios and Roy (2008). Each of these applications is developed based on the thermal or mechanical effects of cavitation and stimulated with different exposure parameters with or without cavitation nuclei.

Acoustic cavitation can be categorised as either of two phenomena: non-inertial cavitation and inertial cavitation. Non-inertial (stable) cavitation generally refers to the bubble oscillating around an equilibrium radius. At relatively low ultrasound pressure, the bubble behaves in a symmetrical and linear manner, which illustrates as its expansion and compression is proportional to the exposure pressure Quaia (2005). Stable oscillations can create liquid flows, or 'micro-streaming', surrounding the bubbles VanBavel (2007). When oscillating bubbles are near the cells, they can cause shear stress the cell membrane. The intensity of shear stress (related to the bubble motion) is the ultrasound parameter depend and has been demonstrated in simulations can be ranged from 100 to 1000 Pa Wu (2002). This shear stress generated by stable cavitation can cause temporary pores in the cell membrane, with the potential benefit that molecules (such as drugs and calcium) are able to enter the cell via passive diffusion Guzman et al. (2001); Tran et al. (2007).

When with sufficient large peak negative pressure of the ultrasound field, cavitation can grow to several times of its original size during the negative pressure phase, which can result in non-linear oscillations Ball (1982); Sboros (2008). In this stage, the bubbles are generally unstable and can be rapidly collapsed due to the inertia of in-rushing fluid. This results in the fragmentation of cavitation into numerous smaller bubbles, known as the process of the inertial cavitation. When the bubble with non-linear asymmetric oscillation and collapses phenomenon, a broadband pressure wave can be generated in the fluid and present as a jet. In particular, a collapse occurring close to the surface of the cell membrane can result in the formation of a liquid jet towards the nearby surface. The consequent shock waves and micro-jet can generate high forces that perforate the cell membranes

and permeabilise blood vessels Postema et al. (2004, 2005). Moreover, inertial cavitation collapse has been demonstrated to be associated with transient ultrasonic energy and broadband noise. Broadband noise can generally be achieved by nulling the harmonic emissions at multiples of the central frequency (nf_0, n = 1, 2, 3, 4, ...) and is a tool for monitoring cavitation activity during HIFU therapy Gyongy and Coussios (2009); McLaughlan et al. (2010b). Inertial cavitation can also contribute to certain physical effects, such as sonoluminescence (extreme thermodynamic conditions in cavitation results in light production) Walton and Reynolds (1984) and sonochemistry (chemical reactions) Suslick (1990). For ultrasound therapy, inertial cavitation can play a role in the thermal ablation of tissue Yoshizawa et al. (2017), histotripsy Lingeman et al. (2009); Roberts (2014), etc., as mentioned above.

1.2.4 Clinical uses of high-intensity focused ultrasound

HIFU therapy implemented via clinical-relevant systems has been used in cancerous tissues in the prostate, uterus, breast, liver and pancreas Blana et al. (2004); Chan et al. (2002); Huber et al. (2001); Kennedy et al. (2004a); Kennedy (2005); Szabo (2004a); Ter Haar and Coussios (2007); WU et al. (2003). Clinical HIFU devices have been under development since the 1990s and are now in routine clinical use. The clinical systems can generally be categorised into ultrasound or magnetic resonance image guidance, and either transrectal or extracorporeal types Kim et al. (2008).

Two transrectal devices are popularly used for clinical uses: Ablatherm HIFU system (EDAP, Vaulx-en-Velin, France) and Sonablate 500 system (Focus Surgery, Inc., Indianapolis, IN, USA). Both are monitored and guided by ultrasound methods; the typical application of these two systems is for the prostate pathology therapy. Extracorporeal devices, which are more versatile than transrectal devices, have been applied in benign and malignant pathology of the liver, kidney, etc. Standard extracorporeal HIFU systems include the HAIFU System (Chongqing HIFU Technology Co., Ltd., Chongqing, China), the HIFU Tumor Therapy System (also developed in China) and Exablate 2000 (InSightec, Haifa, Israel). The HIFU system from China assisted by ultrasound modalities which is composed of the diagnostic array coaxial in the middle of a spherically curved HIFU transducer. On the other hand, the therapeutic system developed in Israel is a magnetic resonance-assisted device that uses a 200-element phased-array transducer with

beam-steering capability.

1.3 High-intensity focused ultrasound treatment monitoring

Guidance and monitoring of HIFU treatments can increase the clinical translation of acoustic therapy and improve aspects of treatment, including efficacy and safety. Precision targeting can increase the propagation accuracy of HIFU dose to cancerous tissue without affecting adjacent healthy tissue. An ultrasound guidance procedure always contains three aspects: 1) pre-treatment mapping to confirm the treatment region and the anatomical information relating to the tissue structure, 2) in-treatment monitoring of the therapeutic process on the targeted tissue and 3) post-treatment evaluation and analysis of the therapy performance Vaezy et al. (2001). Clinical and research HIFU guidance methods mainly comprise MRI and ultrasound modalities: passive cavitation detection (PCD), active cavitation detection (ACD), interlaced B-mode, Passive Acoustic Mapping (PAM) and temperature mapping (either the MRI-assisted or ultrasound-assisted).

1.3.1 Magnetic resonance imaging

Magnetic resonance imaging is the gold-standard monitoring technique for HIFU clinical use Bacon and Carstensen (1990); Duc and Keserci (2018). It can be understood as a way to measure the response of atomic particles to high-frequency radio waves in the magnetic field. High intensity focused ultrasound therapy guided by MRI is commonly termed MRI-guided focused ultrasound surgery (MRgFUS). The first combination of ultrasound and MRI was proposed in the early 1990s, with an ultrasound transducer set inside an MRI scanner Jolesz and Jakab (1991). The idea of using MRI to monitor HIFU therapy for tissue necrosis was originally suggested by Hynynen et al. in 1992 Hynynen et al. (1993); Schenck et al. (1993), and the published results illustrated that lesions formed by HIFU exposure in muscle tissue can be visualised by MRI. Thus, the idea of MRI-guided non-invasive HIFU surgery was proved to be feasible.

Since then, MRgFUS has been reported to have viable applications in tumour treatment and guidance, e.g. for uterine leiomyomas Fennessy et al. (2007); Hindley et al. (2004); Stewart et al. (2003, 2006). Several preliminary clinical studies on MRgFUS in the treatment of breast tumours have also been published Merckel et al. (2013, 2016); Peek and Wu (2018). Some pre-clinical use of MRgFUS

for gene therapy Huber et al. (2003); Kim and Han (2018), thermal ablation of liver tumours Kennedy et al. (2004b); Wijlemans et al. (2012) and brain tumours Dervishi et al. (2013); MacDonell et al. (2018) have also been reported.

The main added value of MRgFUS is its capability to provide temperature measurements within the targeted region, with relatively high spatial and temporal resolution (typically with sub-Hz and roughly 1 mm). The commonly used MR thermometry methods are based on the parameter proton resonance frequency, which is largely tissue-independent and linearly dependent on temperature and, thus, gives sufficient signal-to-noise and temperature accuracy. Generally, MRgFUS can be used for treatment planning, e.g. for tumour detection, due to its high sensitivity, its ability to provide fine anatomic details and its quasi-real-time thermal monitoring of HIFU therapy with approximately 1°C accuracy Köhler et al. (2009); Poorter et al. (1995). However, the limitation of MRgFUS systems is that they are large and expensive, additionally MR thermometry cannot be used for non-thermal HIFU treatment, such as the drug delivery for Blood–Brain Barrier (BBB) opening, and it therefore lacks monitoring ability for cavitation, which restricts the clinical application of MR thermometry with a wider area, and raises the concern about the adoption of ultrasound monitoring.

1.3.2 Active acoustic monitoring

When compared with the MRgFUS system, the ultrasound-guided focused ultrasound system (and its ultrasound monitoring methods) has advantages that include being portable and low cost .etc; hence, it has great potential for clinical adoption. Active acoustic monitoring methods mainly include ACD and B-mode ultrasound imaging techniques. The common limitation of all active acoustic monitoring methods is that they cannot be performed in parallel with ultrasound therapy due to the interference of the HIFU beam, and incapable of distinguishing the normal and lesion tissues.

Conventional ACD is performed with a single-element detector Crum et al. (1992). Its working principle is to transmit a pulse at a high-frequency and detect the backscattering from bubble emissions via the pulse-echo mode. In addition to the aforementioned common limitation, ACD cannot provide much spatial information, and the emissions generated from hyperechogenicity show only the backscattering information of the cross-section related to the bubble that occurs post-exposure, not the phenomenon that induced this cross-section. Consequently,

ACD techniques have been developed into the image domain, with the B-mode diagnostic array.

Several techniques have been introduced into interlaced B-mode with HIFU to improve the image quality and detect sensitivity. In terms of beamforming techniques, as well as the conventional beamforming algorithm delay-and-sum (DAS), data-adaptive methods, such as minimum variance distortionless response and its related techniques (e.g. eigensubspace and coherent factors) have been combined with B-mode Asl and Mahloojifar (2009, 2010); Holfort et al. (2009). However, these related adaptive methods always involve high computation costs, which makes them unpopular for clinical use. Coherent beamforming methods, delay-multiply-and-sum (DMAS) and other methods, have been investigated with finer image quality and demonstrate can have the same computation complexity as DAS Matrone et al. (2016, 2014); Mozaffarzadeh et al. (2018).

In addition to the development of beamforming techniques, harmonic imaging is also applied to map the non-linear scattering/emissions of an incident wave from bubbles/contrast agents or to map the non-linear propagation of the incident wave in the medium, with the aim of improving the signal-to-noise ratio for detecting sensitivity Averkiou (2000); Hwang and Simpson (1998). For the monitoring of cavitation activities occurred in HIFU therapy, due to the strong non-linear characteristic of cavitation activities with harmonic components, interlaced B-mode can be beamformed with the received higher harmonic emissions for increased image quality to localise the cavitated bubbles. Also, the multi-pulse imaging technique, such as the pulse inversion, was developed to enhance the sensitivity of nonlinear imaging, specifically, two pulses with inverted amplitude information are transmitted to perform pulse inversion, then their echoes are summed to reject the linearly responding components and to improve the signal-to-noise ratio (the schematic picture shown in Figure 1.2) Burns et al. (2000); Ma et al. (2005); Song et al. (2013). A similar strategy has also been applied to absolute-time-of-flight beamformed PAM for the detection of weak bubble acoustic signals during HIFU therapy Pouliopoulos et al. (2018).

Conventionally, the interlaced B-mode can be achieved by line-by-line transmissions with the dynamic focus regime Szabo (2004b). This mode can provide finer contrast to noise ratio but with low frame rate (typically 30 Hz for interleaving) that incapable of capturing transient bubble behaviours and allow the bubble to be dissolved in the HIFU-off interval without available feedback Khokhlova et al. (2006). Therefore, the plane wave was developed as an ultrafast active ultrasound

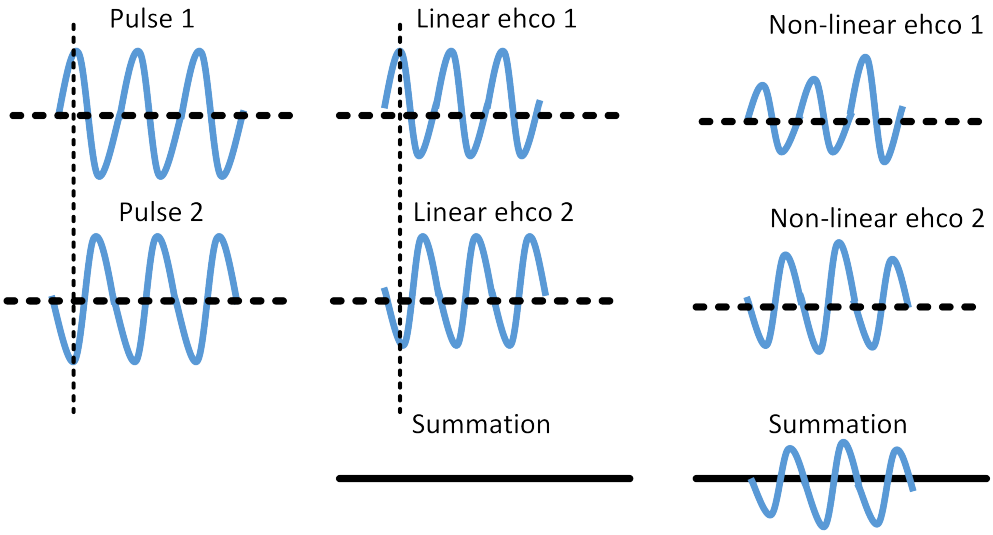

Figure 1.2: The schematic of pulse inversion regime. The summation of echoes is to null the linear components, whereas the residual parts is the non-linear signal.

imaging technique that can be interlaced with HIFU exposure facilitating a significantly increased frame rate for cavitation monitoring Grondin et al. (2015); Tanter and Fink (2014). Since all element transmission with no focusing, that feature can degrade the signal to noise ratio, coherent compounded plane wave imaging was then introduced to mitigate this issue. Multiple steered plane waves are transmitted, and the received back-scattered emissions from all angles are averaged into the final B-mode for finer image contrast and signal-to-noise ratio Austeng et al. (2011); Montaldo et al. (2009). This method can effect the frame rate, but the results demonstrate that the compromised frame rate can reach 463 fps for imaging rapidly moving targets (faster than the typical dissolution time of contrast agents between 1 and 30 ms Uhlendorf et al. (2000)), and therefore could be adopted for the hyperechogenicity monitoring Denarie et al. (2013).

Another suggested B-mode technique related to HIFU monitoring is about the identification of tissue ablation. This functional B-mode method is developed based on the dynamic change in tissue attenuation and stiffness due to the occurrence of lesions Chang et al. (2013); Damianou et al. (1997). An associated research topic is the Acoustic Radiation Force Impulse (ARFI) imaging which has been investigated based on the acoustic radiation force generated within focal zone, and then subsequently use the B-mode image to measure tissue displacements for dynamic stiffness estimation Doherty et al. (2013); Nightingale (2011); Nightingale

et al. (2002). One concern about ARFI techniques which is the tissue displacements caused by motion artefacts can affect the accuracy of final measurements. Consequently, more advanced and robust radiation-force methods have been explored, such as harmonic motion imaging E Konofagou et al. (2012); Hynynen and Konofagou (2006); Konofagou and Hynynen (2003), amplitude-modulated harmonic motion imaging Maleke and Konofagou (2008); Maleke et al. (2006); Vappou et al. (2009) and supersonic shear wave imaging Bercoff et al. (2004); Gennisson et al. (2012). All of these aim to monitor the change in the speed of sound through the focal zone and identify the changes in tissue stiffness by active ultrasound imaging or ultrafast active ultrasound imaging.

1.3.3 Passive acoustic monitoring

Passive acoustic monitoring mainly includes PCD and PAM, which provide the feedback on cavitation activity in one dimension or two dimensions. PCD employs a single detector to passively receive acoustic emissions or scatter during HIFU therapy. The frequency components of the passively received acoustic emissions (beyond the magnitude of floor noise), can be used as an indicator of different bubble behaviours. Harmonic emissions are received at multiples of the centre frequency ($\mathrm{nf_o}, \mathrm{n} = 2, 3, 4, ...$; f_o is the centre frequency), which can originate from non-linear bubble oscillations and non-linear ultrasound propagation Leighton (2012). The subharmonic components ($\mathrm{nf_o/m}, \mathrm{m} = 2, 3, 4, ..., \mathrm{n} = 1$) are generally understood as the indicator of stable cavitation (but can also occur for inertially cavitating bubbles if the bubble keeps oscillating at a period multiple to the centre frequency). Ultraharmonic emissions ($\mathrm{nf_o/m}, \mathrm{m} = 2, 3, 4, ..., \mathrm{n} = 2, 3, 4, ...$) are usually caused by the propagation of subharmonic components through non-linear tissue (but the exact mechanism that causes ultraharmonic emissions has not been fully understood) Ilyichev et al. (1989). Broadband emissions are indicator for the occurrence of the inertial cavitation (When the bubble collapses, it can generate the shock wave and micro-jet in a very short time. The rapid time-domain signal is very broad in the frequency domain which makes the broadband emissions are efficient for the inertial cavitation monitoring) McLaughlan et al. (2017).

Passive acoustic mapping can be briefly described as using a multi-element array to passively record acoustic emissions and then reconstruct the distribution of cavitation sources with spatial information via passive beamforming techniques.

These methods originated from passive sonar, used to map and localise underground seismic features and ocean structures under ambient noise Buckingham et al. (1992); Norton and Won (2000). Then, this concept was introduced into the therapeutic ultrasound field for mapping and quantitative analysis of the resulting cavitation activities (i,e., cavitation localisation and cavited dose calculation) Gyongy et al. (2008); Gyöngy and Coussios (2010).

Based on the duration of the therapeutic ultrasound pulses, PAM beamforming algorithms can be divided into the absolute-time-of-flight beamformers, and relative-time-of-flight beamformers. For very short high-intensity therapeutic pulses, e.g. with pulse duration in micro-second magnitude, that work for BBB disruption, the absolute-time-of-flight beamformer is preferred for therapeutic monitoring and generally, this method has better resolution than the relative-time-of-flight beamformer Davies et al. (2020); Gateau et al. (2011). Conversely, for long high-intensity therapeutic exposures with a high duty cycle, the relative-time-of-flight beamformer is applied to average the intensity bins within the cavitation activity period for the final energy output Gyongy et al. (2008); Gyöngy and Coussios (2010). The relative-time-of-flight beamformer is a sub-optimal beamforming technique due to the unknown of a priori time-of-flight information, and usually suffers from 'X-type' artefacts in the axial direction.

Passive acoustic mapping beamforming techniques have been implemented in both the time and frequency domains. Time-domain PAM is more readily implanted in the hardware platform for commercial use. Frequency-domain PAM can directly select the intensity bin within the interested frequency band without the need for filtering, thus increasing the computation speed (as fewer intensity bins can be averaged into one frame) Haworth et al. (2016); Kim et al. (2020). Another advantage of frequency-domain PAM is that its beamforming process contains the phased components, potentially making phase-aberration correction more straightforward, particularly for transcranial applications Arvanitis et al. (2016). However, frequency-domain PAM cannot provide time-evolution cavitation information. Therefore, the transient angular spectrum approach has been introduced into PAM to maintain time evolution information and optimise computation speed, with the added benefit of accurate cavitation localisation capability Li et al. (2021). Regarding image quality, a variety of beamforming techniques have been developed. The most popular ones are time exposure acoustics (TEA) and the robust Capon beamformer (RCB) Coviello et al. (2015); Norton and Won (2000). Subsequently, more techniques have been integrated into the PAM beam-

former, such as the coherent factor and cross-spectral matrix estimation Boulos et al. (2018); Polichetti et al. (2020). Additionally, to optimise the computation cost of PAM, the paralleled running beamforming technique with sparse matrix, implemented via a Graphics Processing Unit (GPU) and sparse array, has been investigated Kamimura et al. (2020); Sivadon et al. (2020).

Passive acoustic mapping and related methods have been applied in a variety of ways, including for tracking and analysing cavitation activities in phantoms Choi and Coussios (2012); Crake et al. (2015); Gyongy and Coussios (2009); Haworth et al. (2012) and monitoring drug delivery related to the inertial cavitation phenomenon and correlated with drug extravasation Kwan et al. (2015). Passive acoustic mapping has also been used for acoustic monitoring, lesion prediction Haworth et al. (2015); Salgaonkar et al. (2009), and the simulation and correction of the phase-aberration effects for trans-cranial cavitation imaging Arvanitis et al. (2014, 2013); O'Reilly et al. (2014).

1.3.4 Ultrasound temperature monitoring

In addition to the applications of MR thermometry mentioned in Section 1.3.1 with the capability to provide accurate temperature measurements for thermal ultrasound therapy. Ultrasound methods have also been widely investigated for temperature-related phenomena for HIFU therapy.

Passive acoustic mapping (for the measurement of energy absorption from inertial acoustic bubble emissions) combined with a nonlinear bioheat equation (for the measurement of the acoustic absorption of the primary HIFU beam) have been proposed to give an evolving estimation of temperature rise and tissue-ablated cell death for HIFU thermal therapy guidance Jensen et al. (2013). The interlaced B-mode for hyperechogenic imaging has also been investigated in temperature monitoring studies, however, due to the possible absence of boiling bubbles, it may have insufficient hyperechoic features for ultrasound-based thermal therapy monitoring. Moreover, the temperature rises of the HIFU field have not been found to have a strong relationship with tissue echogenicity, except when a significant population of boiling bubble occurs, also the boiling bubbles are always correlated with over-treatment, which all indicate this active monitoring method is not reliable Bailey et al. (2001); Hill and Ter Haar (1995); Jensen et al. (2012); Khokhlova et al. (2006).

Several alternative active ultrasound techniques have also been developed for

dynamic temperature information and lesion identification. One representative algorithm is based on the change in the speed of sound Miller et al. (2004). The speed of sound is assumed to be constant for B-mode imaging and hence, the evolved tissue characteristic in the HIFU targeted zone can cause a dynamic change in the speed of sound, and displayed in the interlaced B-mode with tissue structure displacement. This feature can be estimated by the coherent correlation method for the quantitative analysis of displacement and changes in the temperature field. However, many factors may affect the efficiency of such method, including the varied speed of sound in different tissue layers, the impact of tissue motion and the loss of elastic properties when tissue is denatured with coagulation necrosis. Other techniques for exploring ablated regions based on tissue attenuation and stiffness have also been used for HIFU monitoring, as described in Section 1.3.2. Additionally, active acoustic mapping related to ARFI techniques has been combined with finite element methods to simulate temperature distribution during ultrasound-based therapy and assist in accurate HIFU treatment guidance Fahey et al. (2005); Martínez et al. (2015); Palmeri et al. (2005).

1.4 Thesis objective and outline

The objective of this thesis was to explore the new algorithms into hybrid ultrasound modalities and applied for HIFU therapy monitoring. The outline of this thesis is as follows: In Chapter 2, some key parameters and factors of hybrid pulse sequence and interlaced B-mode are analysed which is to build foundation for the implementation of HIFU experiments and its ultrasound monitoring, including the optimal interlaced B-mode modality via phased array and optimal duty cycle for the implementation of hybrid pulse regimen. Then, the introduction of power spectrum equalised techniques into the interlaced B-mode is proposed. In Chapter 3, based on the foundation (the hybrid pulse implementation) from Chapter 2, various time-domain PAM beamformers are illustrated and compared with the proposed beamforming approach based on DC-component reduction which works as an alternative method of PCD (passive monitoring method presented in Chapter 2), and the experimental results from the gel phantom and *ex vivo* liver studies are analysed. In Chapter 4, the element directivity factor based on a soft-baffle model which was developed as a pixel-wise F-number and shading weight strategy into PAM (and interlaced B-mode) for image quality improvement, the final output is examined by simulation and experiments. In Chapter 5, for a competent

field of view, a polar coordinate PAM is proposed, alongside a dual-mode between the interlaced B-mode and PAM was mutually convoluted for the enhancement of PAM image quality. In Chapter 6, an overall summary of the PhD work and thoughts on future studies are presented.

Chapter References

Arvanitis C.D., Clement G.T. and McDannold N. (2014). Transcranial assessment and visualization of acoustic cavitation: modeling and experimental validation. *IEEE transactions on medical imaging*, **34**(6), pp. 1270–1281.

Arvanitis C.D., Crake C., McDannold N. and Clement G.T. (2016). Passive acoustic mapping with the angular spectrum method. *IEEE transactions on medical imaging*, **36**(4), pp. 983–993.

Arvanitis C.D., Livingstone M.S. and McDannold N. (2013). Combined ultrasound and mr imaging to guide focused ultrasound therapies in the brain. *Physics in Medicine & Biology*, **58**(14), p. 4749.

Ashokkumar M. (2011). The characterization of acoustic cavitation bubbles–an overview. *Ultrasonics sonochemistry*, **18**(4), pp. 864–872.

Asl B.M. and Mahloojifar A. (2009). Minimum variance beamforming combined with adaptive coherence weighting applied to medical ultrasound imaging. *IEEE transactions on ultrasonics, ferroelectrics, and frequency control*, **56**(9), pp. 1923–1931.

Asl B.M. and Mahloojifar A. (2010). Eigenspace-based minimum variance beamforming applied to medical ultrasound imaging. *IEEE transactions on ultrasonics, ferroelectrics, and frequency control*, **57**(11), pp. 2381–2390.

Austeng A., Nilsen C.I.C., Jensen A.C., Näsholm S.P. and Holm S. (2011). Coherent plane-wave compounding and minimum variance beamforming. In: *2011 IEEE International Ultrasonics Symposium*. IEEE, pp. 2448–2451.

Averkiou M.A. (2000). Tissue harmonic imaging. In: *2000 IEEE Ultrasonics Symposium. Proceedings. An International Symposium (Cat. No. 00CH37121)*, vol. 2. IEEE, pp. 1563–1572.

Bacon D.R. and Carstensen E.L. (1990). Increased heating by diagnostic ultrasound due to nonlinear propagation. *The Journal of the Acoustical Society of America*, **88**(1), pp. 26–34.

Bailey M.R., Couret L.N., Sapozhnikov O.A., Khokhlova V.A., ter Haar G., Vaezy S., Shi X., Martin R. and Crum L.A. (2001). Use of overpressure to assess the role

of bubbles in focused ultrasound lesion shape in vitro. *Ultrasound in medicine & biology*, **27**(5), pp. 695–708.

Ball J.M. (1982). Discontinuous equilibrium solutions and cavitation in nonlinear elasticity. *Philosophical Transactions of the Royal Society of London. Series A, Mathematical and Physical Sciences*, **306**(1496), pp. 557–611.

Baseri B., Choi J.J., Tung Y.S. and Konofagou E.E. (2010). Multi-modality safety assessment of blood-brain barrier opening using focused ultrasound and definity microbubbles: a short-term study. *Ultrasound in medicine & biology*, **36**(9), pp. 1445–1459.

Beik J., Abed Z., Ghoreishi F.S., Hosseini-Nami S., Mehrzadi S., Shakeri-Zadeh A. and Kamrava S.K. (2016). Nanotechnology in hyperthermia cancer therapy: From fundamental principles to advanced applications. *Journal of Controlled Release*, **235**, pp. 205–221.

Bercoff J., Tanter M. and Fink M. (2004). Supersonic shear imaging: a new technique for soft tissue elasticity mapping. *IEEE transactions on ultrasonics, ferroelectrics, and frequency control*, **51**(4), pp. 396–409.

Beyer R.T. (1975). *Nonlinear acoustics*. The Command.

Bing K.F., Howles G.P., Qi Y., Palmeri M.L. and Nightingale K.R. (2009). Blood-brain barrier (bbb) disruption using a diagnostic ultrasound scanner and definity® in mice. *Ultrasound in medicine & biology*, **35**(8), pp. 1298–1308.

Blana A., Walter B., Rogenhofer S. and Wieland W.F. (2004). High-intensity focused ultrasound for the treatment of localized prostate cancer: 5-year experience. *Urology*, **63**(2), pp. 297–300.

Boulos P., Varray F., Poizat A., Ramalli A., Gilles B., Bera J.C. and Cachard C. (2018). Weighting the passive acoustic mapping technique with the phase coherence factor for passive ultrasound imaging of ultrasound-induced cavitation. *IEEE transactions on ultrasonics, ferroelectrics, and frequency control*, **65**(12), pp. 2301–2310.

Buckingham M.J., Berknout B.V. and Glegg S.A. (1992). Imaging the ocean with ambient noise. *Nature*, **356**(6367), pp. 327–329.

Burns P.N., Wilson S.R. and Simpson D.H. (2000). Pulse inversion imaging of liver blood flow: improved method for characterizing focal masses with microbubble contrast. *Investigative radiology*, **35**(1), p. 58.

Chan A.H., Fujimoto V.Y., Moore D.E., Martin R.W. and Vaezy S. (2002). An image-guided high intensity focused ultrasound device for uterine fibroids treatment. *Medical physics*, **29**(11), pp. 2611–2620.

Chang J.M., Park I., Lee S.H., Kim W.H., Bae M.S., Koo H.R., Yi A., Kim S.J., Cho N. and Moon W.K. (2013). Stiffness of tumours measured by shear-wave elastography correlated with subtypes of breast cancer. *European radiology*, **23**(9), pp. 2450–2458.

Choi J.J. and Coussios C.C. (2012). Spatiotemporal evolution of cavitation dynamics exhibited by flowing microbubbles during ultrasound exposure. *The Journal of the Acoustical Society of America*, **132**(5), pp. 3538–3549.

Clarke R. and Ter Haar G. (1997). Temperature rise recorded during lesion formation by high-intensity focused ultrasound. *Ultrasound in medicine & biology*, **23**(2), pp. 299–306.

Coussios .C., Farny C., Ter Haar G. and Roy R. (2007). Role of acoustic cavitation in the delivery and monitoring of cancer treatment by high-intensity focused ultrasound (hifu). *International journal of hyperthermia*, **23**(2), pp. 105–120.

Coussios C.C. and Roy R.A. (2008). Applications of acoustics and cavitation to noninvasive therapy and drug delivery. *Annu. Rev. Fluid Mech.*, **40**, pp. 395–420.

Coviello C., Kozick R., Choi J., Gyöngy M., Jensen C., Smith P.P. and Coussios C.C. (2015). Passive acoustic mapping utilizing optimal beamforming in ultrasound therapy monitoring. *The Journal of the Acoustical Society of America*, **137**(5), pp. 2573–2585.

Crake C., de Saint Victor M., Owen J., Coviello C., Collin J., Coussios C.C. and Stride E. (2015). Passive acoustic mapping of magnetic microbubbles for cavitation enhancement and localization. *Physics in Medicine & Biology*, **60**(2), p. 785.

Craster R.V. and Guenneau S. (2012). *Acoustic metamaterials: Negative refraction, imaging, lensing and cloaking*, vol. 166. Springer Science & Business Media.

Crum L., Roy R., Dinno M., Church C., Apfel R., Holland C. and Madanshetty S. (1992). Acoustic cavitation produced by microsecond pulses of ultrasound: a discussion of some selected results. *The Journal of the Acoustical Society of America*, **91**(2), pp. 1113–1119.

Damianou C.A., Sanghvi N.T., Fry F.J. and Maass-Moreno R. (1997). Dependence of ultrasonic attenuation and absorption in dog soft tissues on temperature and thermal dose. *The Journal of the Acoustical Society of America*, **102**(1), pp. 628–634.

Davies H.J., Morse S.V., Copping M.J., Sujarittam K., Bourgin V.D., Tang M.X. and Choi J.J. (2020). Imaging with therapeutic acoustic wavelets–short pulses enable acoustic localization when time of arrival is combined with delay and sum. *IEEE Transactions on Ultrasonics, Ferroelectrics, and Frequency Control*, **68**(1), pp. 178–190.

Denarie B., Tangen T.A., Ekroll I.K., Rolim N., Torp H., Bjåstad T. and Lovstakken L. (2013). Coherent plane wave compounding for very high frame rate ultrasonography of rapidly moving targets. *IEEE transactions on medical imaging*, **32**(7), pp. 1265–1276.

Dervishi E., Larrat B., Pernot M., Adam C., Marie Y., Fink M., Delattre J.Y., Boch A.L., Tanter M. and Aubry J.F. (2013). Transcranial high intensity focused ultrasound therapy guided by 7 tesla mri in a rat brain tumour model: a feasibility study. *International Journal of Hyperthermia*, **29**(6), pp. 598–608.

Dictionary O.E. (1989). Oxford english dictionary. *Simpson, Ja & Weiner, Esc*, p. 3.

Diederich C.J. (2005). Thermal ablation and high-temperature thermal therapy: overview of technology and clinical implementation. *International journal of hyperthermia*, **21**(8), pp. 745–753.

Doherty J.R., Trahey G.E., Nightingale K.R. and Palmeri M.L. (2013). Acoustic radiation force elasticity imaging in diagnostic ultrasound. *IEEE transactions on ultrasonics, ferroelectrics, and frequency control*, **60**(4), pp. 685–701.

Dromi S., Frenkel V., Luk A., Traughber B., Angstadt M., Bur M., Poff J., Xie J., Libutti S.K., Li K.C. et al. (2007). Pulsed-high intensity focused ultrasound and low temperature–sensitive liposomes for enhanced targeted drug delivery and antitumor effect. *Clinical cancer research*, **13**(9), pp. 2722–2727.

Duc N.M. and Keserci B. (2018). Review of influential clinical factors in reducing the risk of unsuccessful mri-guided hifu treatment outcome of uterine fibroids. *Diagnostic and Interventional Radiology*, **24**(5), p. 283.

Duck F.A., Baker A.C. and Starritt H.C. (2020). *Ultrasound in medicine*. CRC Press.

E Konofagou E., Maleke C. and Vappou J. (2012). Harmonic motion imaging (hmi) for tumor imaging and treatment monitoring. *Current Medical Imaging*, **8**(1), pp. 16–26.

Ebbini E.S. and Ter Haar G. (2015). Ultrasound-guided therapeutic focused ultrasound: current status and future directions. *International journal of hyperthermia*, **31**(2), pp. 77–89.

Escudero D.S., Goudot G., Vion M., Tanter M. and Pernot M. (2018). 2d and 3d real-time passive cavitation imaging of pulsed cavitation ultrasound therapy in moving tissues. *Physics in Medicine & Biology*, **63**(23), p. 235028.

Fahey B.J., Nightingale K.R., Nelson R.C., Palmeri M.L. and Trahey G.E. (2005). Acoustic radiation force impulse imaging of the abdomen: demonstration of feasibility and utility. *Ultrasound in medicine & biology*, **31**(9), pp. 1185–1198.

Fennessy F.M., Tempany C.M., McDannold N.J., So M.J., Hesley G., Gostout B., Kim H.S., Holland G.A., Sarti D.A., Hynynen K. et al. (2007). Uterine leiomyomas: Mr imaging–guided focused ultrasound surgery—results of different treatment protocols. *Radiology*, **243**(3), pp. 885–893.

Frenkel V. (2008). Ultrasound mediated delivery of drugs and genes to solid tumors. *Advanced drug delivery reviews*, **60**(10), pp. 1193–1208.

Fry D.L. and Hyatt R.E. (1960). Pulmonary mechanics: a unified analysis of the relationship between pressure, volume and gasflow in the lungs of normal and diseased human subjects. *The American journal of medicine*, **29**(4), pp. 672–689.

Gallego-Juárez J.A. (2017). Basic principles of ultrasound. *Ultrasound in Food Processing. Chichester: Wiley Blackwell*, pp. 1–26.

Gateau J., Aubry J.F., Pernot M., Fink M. and Tanter M. (2011). Combined passive detection and ultrafast active imaging of cavitation events induced by short pulses of high-intensity ultrasound. *IEEE transactions on ultrasonics, ferroelectrics, and frequency control*, **58**(3), pp. 517–532.

Gennisson J.L., Grenier N., Combe C. and Tanter M. (2012). Supersonic shear wave elastography of in vivo pig kidney: influence of blood pressure, urinary pressure and tissue anisotropy. *Ultrasound in medicine & biology*, **38**(9), pp. 1559–1567.

Goldberg B.B. and Lehman J.S. (1969). Some observations on the practical uses of a-mode ultrasound. *American Journal of Roentgenology*, **107**(1), pp. 198–205.

Grondin J., Payen T., Wang S. and Konofagou E.E. (2015). Real-time monitoring of high intensity focused ultrasound (hifu) ablation of in vitro canine livers using harmonic motion imaging for focused ultrasound (hmifu). *JoVE (Journal of Visualized Experiments)*, (105), p. e53050.

Grüll H. and Langereis S. (2012). Hyperthermia-triggered drug delivery from temperature-sensitive liposomes using mri-guided high intensity focused ultrasound. *Journal of Controlled Release*, **161**(2), pp. 317–327.

Guzman H.R., Nguyen D.X., Khan S. and Prausnitz M.R. (2001). Ultrasound-mediated disruption of cell membranes. ii. heterogeneous effects on cells. *The Journal of the Acoustical Society of America*, **110**(1), pp. 597–606.

Gyongy M., Arora M., Noble J.A. and Coussios C.C. (2008). Use of passive arrays for characterization and mapping of cavitation activity during hifu exposure. In: *2008 IEEE Ultrasonics Symposium*. IEEE, pp. 871–874.

Gyongy M. and Coussios C.C. (2009). Passive spatial mapping of inertial cavitation during hifu exposure. *IEEE Transactions on Biomedical Engineering*, **57**(1), pp. 48–56.

Gyöngy M. and Coussios C.C. (2010). Passive cavitation mapping for localization and tracking of bubble dynamics. *The Journal of the Acoustical Society of America*, **128**(4), pp. EL175–EL180.

Haworth K.J., Bader K.B., Rich K.T., Holland C.K. and Mast T.D. (2016). Quantitative frequency-domain passive cavitation imaging. *IEEE transactions on ultrasonics, ferroelectrics, and frequency control*, **64**(1), pp. 177–191.

Haworth K.J., Mast T.D., Radhakrishnan K., Burgess M.T., Kopechek J.A., Huang S.L., McPherson D.D. and Holland C.K. (2012). Passive imaging with pulsed ultrasound insonations. *The Journal of the Acoustical Society of America*, **132**(1), pp. 544–553.

Haworth K.J., Salgaonkar V.A., Corregan N.M., Holland C.K. and Mast T.D. (2015). Using passive cavitation images to classify high-intensity focused ultrasound lesions. *Ultrasound in medicine & biology*, **41**(9), pp. 2420–2434.

Hernandez-Andrade E., Jansson T., Ley D., Bellander M., Persson M., Lingman G. and Maršál K. (2004). Validation of fractional moving blood volume measurement with power doppler ultrasound in an experimental sheep model. *Ultrasound in Obstetrics and Gynecology: The Official Journal of the International Society of Ultrasound in Obstetrics and Gynecology*, **23**(4), pp. 363–368.

Hill C. and Ter Haar G. (1995). High intensity focused ultrasound—potential for cancer treatment. *The British journal of radiology*, **68**(816), pp. 1296–1303.

Hill C.R., Bamber J.C. and ter Haar G.R. (2004). Physical principles of medical ultrasonics.

Hindley J., Gedroyc W.M., Regan L., Stewart E., Tempany C., Hynnen K., Macdanold N., Inbar Y., Itzchak Y., Rabinovici J. et al. (2004). Mri guidance of focused ultrasound therapy of uterine fibroids: early results. *American Journal of Roentgenology*, **183**(6), pp. 1713–1719.

Holfort I.K., Gran F. and Jensen J.A. (2009). Broadband minimum variance beamforming for ultrasound imaging. *IEEE transactions on ultrasonics, ferroelectrics, and frequency control*, **56**(2), pp. 314–325.

Hoskins P.R., Martin K. and Thrush A. (2019). *Diagnostic ultrasound: physics and equipment*. CRC Press.

Huber P., Mann M., Melo L., Ehsan A., Kong D., Zhang L., Rezvani M., Peschke P., Jolesz F., Dzau V. et al. (2003). Focused ultrasound (hifu) induces localized

enhancement of reporter gene expression in rabbit carotid artery. *Gene Therapy*, **10**(18), pp. 1600–1607.

Huber P.E., Jenne J.W., Rastert R., Simiantonakis I., Sinn H.P., Strittmatter H.J., von Fournier D., Wannenmacher M.F. and Debus J. (2001). A new noninvasive approach in breast cancer therapy using magnetic resonance imaging-guided focused ultrasound surgery. *Cancer research*, **61**(23), pp. 8441–8447.

Hwang J.J. and Simpson D.H. (1998). Ultrasonic diagnostic imaging with harmonic contrast agents. US Patent 5,706,819.

Hynynen K., Darkazanli A., Unger E. and Schenck J. (1993). Mri-guided noninvasive ultrasound surgery. *Medical physics*, **20**(1), pp. 107–115.

Hynynen K., McDannold N., Martin H., Jolesz F.A. and Vykhodtseva N. (2003). The threshold for brain damage in rabbits induced by bursts of ultrasound in the presence of an ultrasound contrast agent (optison®). *Ultrasound in medicine & biology*, **29**(3), pp. 473–481.

Hynynen K., McDannold N., Vykhodtseva N. and Jolesz F.A. (2001). Noninvasive mr imaging–guided focal opening of the blood-brain barrier in rabbits. *Radiology*, **220**(3), pp. 640–646.

Hynynen K.H. and Konofagou E. (2006). Harmonic motion imaging. US Patent 6,984,209.

Ilyichev V., Koretz V. and Melnikov N. (1989). Spectral characteristics of acoustic cavitation. *Ultrasonics*, **27**(6), pp. 357–361.

Jensen C., Cleveland R. and Coussios C. (2013). Real-time temperature estimation and monitoring of hifu ablation through a combined modeling and passive acoustic mapping approach. *Physics in Medicine & Biology*, **58**(17), p. 5833.

Jensen C.R., Ritchie R.W., Gyöngy M., Collin J.R., Leslie T. and Coussios C.C. (2012). Spatiotemporal monitoring of high-intensity focused ultrasound therapy with passive acoustic mapping. *Radiology*, **262**(1), pp. 252–261.

Jensen J.A. (1996). *Estimation of blood velocities using ultrasound: a signal processing approach*. Cambridge University Press.

Jolesz F.A. and Jakab P.D. (1991). Acoustic pressure wave generation within an mr imaging system: potential medical applications. *Journal of Magnetic Resonance Imaging*, **1**(5), pp. 609–613.

Kamimura H.A., Wu S.Y., Grondin J., Ji R., Aurup C., Zheng W., Heidmann M., Pouliopoulos A.N. and Konofagou E.E. (2020). Real-time passive acoustic mapping using sparse matrix multiplication. *IEEE Transactions on Ultrasonics, Ferroelectrics, and Frequency Control*, **68**(1), pp. 164–177.

Kashcheeva S., Sapozhnikov O., Khokhlova V., Averkiou M. and Crum L. (2000). Nonlinear distortion and attenuation of intense acoustic waves in lossy media obeying a frequency power law. *Acoustical Physics*, **46**(2), pp. 170–177.

Kennedy J., Wu F., Ter Haar G., Gleeson F., Phillips R., Middleton M. and Cranston D. (2004a). High-intensity focused ultrasound for the treatment of liver tumours. *Ultrasonics*, **42**(1-9), pp. 931–935.

Kennedy J., Wu F., Ter Haar G., Gleeson F., Phillips R., Middleton M. and Cranston D. (2004b). High-intensity focused ultrasound for the treatment of liver tumours. *Ultrasonics*, **42**(1-9), pp. 931–935.

Kennedy J.E. (2005). High-intensity focused ultrasound in the treatment of solid tumours. *Nature reviews cancer*, **5**(4), p. 321.

Khokhlova V., Burov V. and Gavrilov L. (2014). High intensity therapeutic ultrasound research in the former ussr in the 1950s–1970s. *The Journal of the Acoustical Society of America*, **136**(4), pp. 2220–2220.

Khokhlova V.A., Bailey M.R., Reed J.A., Cunitz B.W., Kaczkowski P.J. and Crum L.A. (2006). Effects of nonlinear propagation, cavitation, and boiling in lesion formation by high intensity focused ultrasound in a gel phantom. *The Journal of the Acoustical Society of America*, **119**(3), pp. 1834–1848.

Khokhlova V.A., Fowlkes J.B., Roberts W.W., Schade G.R., Xu Z., Khokhlova T.D., Hall T.L., Maxwell A.D., Wang Y.N. and Cain C.A. (2015). Histotripsy methods in mechanical disintegration of tissue: Towards clinical applications. *International journal of hyperthermia*, **31**(2), pp. 145–162.

Kim A. and Han S.H. (2018). A pilot study of microbubble-delivered gene therapy using high intensity focused ultrasound (hifu). *Journal of Undergraduate Life Sciences • Volume*, **12**(1).

Kim P., Song J.H. and Song T.K. (2020). A new frequency domain passive acoustic mapping method using passive hilbert beamforming to reduce the computational complexity of fast fourier transform. *Ultrasonics*, **102**, p. 106030.

Kim Y.s., Rhim H., Choi M.J., Lim H.K. and Choi D. (2008). High-intensity focused ultrasound therapy: an overview for radiologists. *Korean journal of radiology*, **9**(4), pp. 291–302.

Köhler M.O., Mougenot C., Quesson B., Enholm J., Le Bail B., Laurent C., Moonen C.T. and Ehnholm G.J. (2009). Volumetric hifu ablation under 3d guidance of rapid mri thermometry. *Medical physics*, **36**(8), pp. 3521–3535.

Kolios M.C., Worthington A.E., Sherar M.D. and Hunt J.W. (1998). Experimental evaluation of two simple thermal models using transient temperature analysis. *Physics in Medicine & Biology*, **43**(11), p. 3325.

Konofagou E.E. and Hynynen K. (2003). Localized harmonic motion imaging: theory, simulations and experiments. *Ultrasound in medicine & biology*, **29**(10), pp. 1405–1413.

Kremkau F.W. (1979). Cancer therapy with ultrasound: a historical review. *Journal of clinical ultrasound*, **7**(4), pp. 287–300.

Kwan J.J., Myers R., Coviello C.M., Graham S.M., Shah A.R., Stride E., Carlisle R.C. and Coussios C.C. (2015). Ultrasound-propelled nanocups for drug delivery. *small*, **11**(39), pp. 5305–5314.

Laugier P. and Haïat G. (2011). Introduction to the physics of ultrasound. *Bone quantitative ultrasound*, pp. 29–45.

Leighton T. (2012). *The acoustic bubble*. Academic press.

Leighton T.G. (2007). What is ultrasound? *Progress in biophysics and molecular biology*, **93**(1-3), pp. 3–83.

Li M., Gu J., Vu T., Sankin G., Zhong P., Yao J. and Jing Y. (2021). Time-resolved passive cavitation mapping using the transient angular spectrum approach. *IEEE transactions on ultrasonics, ferroelectrics, and frequency control*, **68**(7), pp. 2361–2369.

Lingeman J.E., McAteer J.A., Gnessin E. and Evan A.P. (2009). Shock wave lithotripsy: advances in technology and technique. *Nature Reviews Urology*, **6**(12), pp. 660–670.

Lynn J.G., Zwemer R.L., Chick A.J. and Miller A.E. (1942). A new method for the generation and use of focused ultrasound in experimental biology. *The Journal of general physiology*, **26**(2), p. 179.

Ma Q., Ma Y., Gong X. and Zhang D. (2005). Improvement of tissue harmonic imaging using the pulse-inversion technique. *Ultrasound in medicine & biology*, **31**(7), pp. 889–894.

MacDonell J., Patel N., Rubino S., Ghoshal G., Fischer G., Burdette E.C., Hwang R. and Pilitsis J.G. (2018). Magnetic resonance–guided interstitial high-intensity focused ultrasound for brain tumor ablation. *Neurosurgical focus*, **44**(2), p. E11.

Maleke C. and Konofagou E.E. (2008). Harmonic motion imaging for focused ultrasound (hmifu): a fully integrated technique for sonication and monitoring of thermal ablation in tissues. *Physics in Medicine & Biology*, **53**(6), p. 1773.

Maleke C., Pernot M. and Konofagou E.E. (2006). Single-element focused ultrasound transducer method for harmonic motion imaging. *Ultrasonic imaging*, **28**(3), pp. 144–158.

Maloney E. and Hwang J.H. (2015). Emerging hifu applications in cancer therapy. *International Journal of Hyperthermia*, **31**(3), pp. 302–309.

Martínez R., Vera A. and Leija L. (2015). Hifu induced heating modelling by using the finite element method. *Physics Procedia*, **63**, pp. 127–133.

Mason T.J., Riera E., Vercet A. and Lopez-Buesa P. (2005). Application of ultrasound. In: *Emerging technologies for food processing*. Elsevier, pp. 323–351.

Matrone G., Ramalli A., Savoia A.S., Tortoli P. and Magenes G. (2016). High frame-rate, high resolution ultrasound imaging with multi-line transmission and

filtered-delay multiply and sum beamforming. *IEEE transactions on medical imaging*, **36**(2), pp. 478–486.

Matrone G., Savoia A.S., Caliano G. and Magenes G. (2014). The delay multiply and sum beamforming algorithm in ultrasound b-mode medical imaging. *IEEE transactions on medical imaging*, **34**(4), pp. 940–949.

Maxwell A.D., Wang T.Y., Cain C.A., Fowlkes J.B., Sapozhnikov O.A., Bailey M.R. and Xu Z. (2011). Cavitation clouds created by shock scattering from bubbles during histotripsy. *The Journal of the Acoustical Society of America*, **130**(4), pp. 1888–1898.

McDannold N., Vykhodtseva N. and Hynynen K. (2008). Blood-brain barrier disruption induced by focused ultrasound and circulating preformed microbubbles appears to be characterized by the mechanical index. *Ultrasound in medicine & biology*, **34**(5), pp. 834–840.

McLaughlan J., Cowell D. and Freear S. (2017). Gold nanoparticle nucleated cavitation for enhanced high intensity focused ultrasound therapy. *Physics in Medicine & Biology*, **63**(1), p. 015004.

McLaughlan J., Rivens I., Leighton T. and Ter Haar G. (2010a). A study of bubble activity generated in ex vivo tissue by high intensity focused ultrasound. *Ultrasound in medicine & biology*, **36**(8), pp. 1327–1344.

McLaughlan J., Rivens I., Leighton T. and ter Haar G. (2010b). A study of bubble activity generated in ex vivo tissue by high intensity focused ultrasound. *Ultrasound in Medicine & Biology*, **36**(8), pp. 1327 – 1344. doi: https://doi.org/10.1016/j.ultrasmedbio.2010.05.011.

McLaughlan J.R. (2008). *An investigation into the use of cavitation for the optimisation of high intensity focused ultrasound (HIFU) treatments*. Ph.D. thesis, Institute of Cancer Research (University Of London).

Merckel L.G., Bartels L.W., Köhler M.O., van den Bongard H., Deckers R., Mali W.P.T.M., Binkert C.A., Moonen C.T., Gilhuijs K.G. and van den Bosch M.A. (2013). Mr-guided high-intensity focused ultrasound ablation of breast cancer with a dedicated breast platform. *Cardiovascular and interventional radiology*, **36**(2), pp. 292–301.

Merckel L.G., Knuttel F.M., Deckers R., van Dalen T., Schubert G., Peters N.H., Weits T., van Diest P.J., Mali W.P.T.M., Vaessen P.H. et al. (2016). First clinical experience with a dedicated mri-guided high-intensity focused ultrasound system for breast cancer ablation. *European radiology*, **26**(11), pp. 4037–4046.

Miller N.R., Bamber J.C. and ter Haar G.R. (2004). Imaging of temperature-induced echo strain: preliminary in vitro study to assess feasibility for guiding focused ultrasound surgery. *Ultrasound in medicine & biology*, **30**(3), pp. 345–356.

Montaldo G., Tanter M., Bercoff J., Benech N. and Fink M. (2009). Coherent plane-wave compounding for very high frame rate ultrasonography and transient elastography. *IEEE transactions on ultrasonics, ferroelectrics, and frequency control*, **56**(3), pp. 489–506.

Mozaffarzadeh M., Sadeghi M., Mahloojifar A. and Orooji M. (2018). Double-stage delay multiply and sum beamforming algorithm applied to ultrasound medical imaging. *Ultrasound in medicine & biology*, **44**(3), pp. 677–686.

Nightingale K. (2011). Acoustic radiation force impulse (arfi) imaging: a review. *Current medical imaging*, **7**(4), pp. 328–339.

Nightingale K., Soo M.S., Nightingale R. and Trahey G. (2002). Acoustic radiation force impulse imaging: in vivo demonstration of clinical feasibility. *Ultrasound in medicine & biology*, **28**(2), pp. 227–235.

Norton S.J. and Won I. (2000). Time exposure acoustics. *IEEE Transactions on Geoscience and Remote Sensing*, **38**(3), pp. 1337–1343.

Nyborg W.L. (2001). Biological effects of ultrasound: development of safety guidelines. part ii: general review. *Ultrasound in medicine & biology*, **27**(3), pp. 301–333.

O'Reilly M.A., Jones R.M. and Hynynen K. (2014). Three-dimensional transcranial ultrasound imaging of microbubble clouds using a sparse hemispherical array. *IEEE Transactions on Biomedical Engineering*, **61**(4), pp. 1285–1294.

O'Reilly M.A., Waspe A.C., Ganguly M. and Hynynen K. (2011). Focused-ultrasound disruption of the blood-brain barrier using closely-timed short pulses:

influence of sonication parameters and injection rate. *Ultrasound in medicine & biology*, **37**(4), pp. 587–594.

Palmeri M.L., Sharma A.C., Bouchard R.R., Nightingale R.W. and Nightingale K.R. (2005). A finite-element method model of soft tissue response to impulsive acoustic radiation force. *IEEE transactions on ultrasonics, ferroelectrics, and frequency control*, **52**(10), pp. 1699–1712.

Pauly H. and Schwan H. (1971). Mechanism of absorption of ultrasound in liver tissue. *The Journal of the Acoustical Society of America*, **50**(2B), pp. 692–699.

Peek M.C. and Wu F. (2018). High-intensity focused ultrasound in the treatment of breast tumours. *Ecancermedicalscience*, **12**.

Pierce A.D. and Beyer R.T. (1990). Acoustics: An introduction to its physical principles and applications. 1989 edition.

Polichetti M., Varray F., Gilles B., Béra J.C. and Nicolas B. (2020). Use of the cross-spectral density matrix for enhanced passive ultrasound imaging of cavitation. *IEEE Transactions on Ultrasonics, Ferroelectrics, and Frequency Control*, **68**(4), pp. 910–925.

Poorter J.D., Wagter C.D., Deene Y.D., Thomsen C., Ståhlberg F. and Achten E. (1995). Noninvasive mri thermometry with the proton resonance frequency (prf) method: in vivo results in human muscle. *Magnetic resonance in medicine*, **33**(1), pp. 74–81.

Postema M., Van Wamel A., Lancée C.T. and De Jong N. (2004). Ultrasound-induced encapsulated microbubble phenomena. *Ultrasound in medicine & biology*, **30**(6), pp. 827–840.

Postema M., van Wamel A., ten Cate F.J. and de Jong N. (2005). High-speed photography during ultrasound illustrates potential therapeutic applications of microbubbles. *Medical physics*, **32**(12), pp. 3707–3711.

Pouliopoulos A.N., Burgess M.T. and Konofagou E.E. (2018). Pulse inversion enhances the passive mapping of microbubble-based ultrasound therapy. *Applied Physics Letters*, **113**(4), p. 044102.

Quaia E. (2005). Physical basis and principles of action of microbubble-based contrast agents. In: *Contrast media in ultrasonography*. Springer, pp. 15–30.

Ramalli A., Dallai A., Guidi F., Bassi L., Boni E., Tong L., Fradella G., D'hooge J. and Tortoli P. (2018). Real-time high-frame-rate cardiac b-mode and tissue doppler imaging based on multiline transmission and multiline acquisition. *IEEE transactions on ultrasonics, ferroelectrics, and frequency control*, **65**(11), pp. 2030–2041.

Ranjan A., Jacobs G.C., Woods D.L., Negussie A.H., Partanen A., Yarmolenko P.S., Gacchina C.E., Sharma K.V., Frenkel V., Wood B.J. et al. (2012). Image-guided drug delivery with magnetic resonance guided high intensity focused ultrasound and temperature sensitive liposomes in a rabbit vx2 tumor model. *Journal of controlled release*, **158**(3), pp. 487–494.

Roberts W.W. (2014). Development and translation of histotripsy: current status and future directions. *Current opinion in urology*, **24**(1), p. 104.

Salgaonkar V.A., Datta S., Holland C.K. and Mast T.D. (2009). Passive cavitation imaging with ultrasound arrays. *The Journal of the Acoustical Society of America*, **126**(6), pp. 3071–3083.

Sapareto S.A. and Dewey W.C. (1984). Thermal dose determination in cancer therapy. *International Journal of Radiation Oncology* Biology* Physics*, **10**(6), pp. 787–800.

Sboros V. (2008). Response of contrast agents to ultrasound. *Advanced drug delivery reviews*, **60**(10), pp. 1117–1136.

Schenck J., Damianou C.A., Unger E., Darkazanli A. and Hynynen K. (1993). The feasibility of using mri to monitor and guide noninvasive ultrasound surgery. *Ultrasound in Medicine and Biology*.

Sehgal C.M. and Greenleaf J.F. (1984). Scattering of ultrasound by tissues. *Ultrasonic imaging*, **6**(1), pp. 60–80.

Sibille A., Prat F., Chapelon J.Y., Abou El Fadil F., Henry L., Theillère Y., Ponchon T. and Cathignol D. (1993). Extracorporeal ablation of liver tissue by high-intensity focused ultrasound. *Oncology*, **50**(5), pp. 375–379.

Sivadon A., Varray F., Nicolas B., Béra J.C. and Gilles B. (2020). Using sparse array for 3d passive cavitation imaging. In: *2020 IEEE International Ultrasonics Symposium (IUS)*. IEEE, pp. 1–4.

Song P., Zhao H., Urban M.W., Manduca A., Pislaru S.V., Kinnick R.R., Pislaru C., Greenleaf J.F. and Chen S. (2013). Improved shear wave motion detection using pulse-inversion harmonic imaging with a phased array transducer. *IEEE transactions on medical imaging*, **32**(12), pp. 2299–2310.

Stewart E.A., Gedroyc W.M., Tempany C.M., Quade B.J., Inbar Y., Ehrenstein T., Shushan A., Hindley J.T., Goldin R.D., David M. et al. (2003). Focused ultrasound treatment of uterine fibroid tumors: safety and feasibility of a noninvasive thermoablative technique. *American journal of obstetrics and gynecology*, **189**(1), pp. 48–54.

Stewart E.A., Rabinovici J., Tempany C.M., Inbar Y., Regan L., Gastout B., Hesley G., Kim H.S., Hengst S. and Gedroye W.M. (2006). Clinical outcomes of focused ultrasound surgery for the treatment of uterine fibroids. *Fertility and sterility*, **85**(1), pp. 22–29.

Sullivan E.D., Peter D.J. and Cranley J.J. (1984). Real-time b-mode venous ultrasound. *Journal of Vascular Surgery*, **1**(3), pp. 465–471.

Suslick K.S. (1990). Sonochemistry. *science*, **247**(4949), pp. 1439–1445.

Suslick K.S. and Nyborg W.L. (1990). Ultrasound: its chemical, physical and biological effects.

Szabo T.L. (2004a). *Diagnostic ultrasound imaging: inside out*. Academic Press.

Szabo T.L. (2004b). *Diagnostic ultrasound imaging: inside out*. Academic press.

Tan S., Teh H., Mancer J.K. and Poh W. (2008). Improving b mode ultrasound evaluation of breast lesions with real-time ultrasound elastography—a clinical approach. *The Breast*, **17**(3), pp. 252–257.

Tanter M. and Fink M. (2014). Ultrafast imaging in biomedical ultrasound. *IEEE transactions on ultrasonics, ferroelectrics, and frequency control*, **61**(1), pp. 102–119.

ter Haar .G. and Coussios C. (2007). High intensity focused ultrasound: physical principles and devices. *International journal of hyperthermia*, **23**(2), pp. 89–104.

Ter Haar G. (2007). Turning up the power: High intensity focused ultrasound (hifu) for the treatment of cancer. *Ultrasound*, **15**(2), pp. 73–77.

Ter Haar G. and Coussios C. (2007). High intensity focused ultrasound: past, present and future. *International journal of Hyperthermia*, **23**(2), pp. 85–87.

Ter Haar G., Zahur S. and Jayadewa C. (2009). High-intensity focused ultrasound (hifu) treatment of liver cancer. *Interventional Radiological Treatment of Liver Tumors*, p. 92.

Ter Haar G.R. (2001). High intensity focused ultrasound for the treatment of tumors. *Echocardiography*, **18**(4), pp. 317–322.

Thornycroft J.I. and Barnaby S.W. (1895). Torpedo-boat destroyers.(including appendix and plate at back of volume). In: *Minutes of the Proceedings of the Institution of Civil Engineers*, vol. 122. Thomas Telford-ICE Virtual Library, pp. 51–69.

Tran T., Roger S., Le Guennec J.Y., Tranquart F. and Bouakaz A. (2007). Effect of ultrasound-activated microbubbles on the cell electrophysiological properties. *Ultrasound in medicine & biology*, **33**(1), pp. 158–163.

Tung Y.S., Vlachos F., Choi J.J., Deffieux T., Selert K. and Konofagou E.E. (2010). In vivo transcranial cavitation threshold detection during ultrasound-induced blood–brain barrier opening in mice. *Physics in Medicine & Biology*, **55**(20), p. 6141.

Uhlendorf V., Scholle F.D. and Reinhardt M. (2000). Acoustic behaviour of current ultrasound contrast agents. *Ultrasonics*, **38**(1-8), pp. 81–86.

Vaezy S., Andrew M., Kaczkowski P. and Crum L. (2001). Image-guided acoustic therapy. *Annual review of biomedical engineering*, **3**(1), pp. 375–390.

VanBavel E. (2007). Effects of shear stress on endothelial cells: possible relevance for ultrasound applications. *Progress in biophysics and molecular biology*, **93**(1-3), pp. 374–383.

Vappou J., Maleke C. and Konofagou E.E. (2009). Quantitative viscoelastic parameters measured by harmonic motion imaging. *Physics in Medicine & Biology*, **54**(11), p. 3579.

Walton A.J. and Reynolds G.T. (1984). Sonoluminescence. *Advances in physics*, **33**(6), pp. 595–660.

Wang T.Y., Xu Z., Hall T.L., Fowlkes J.B., Roberts W.W. and Cain C.A. (2011). Active focal zone sharpening for high-precision treatment using histotripsy. *IEEE transactions on ultrasonics, ferroelectrics, and frequency control*, **58**(2), pp. 305–315.

Whittingham T. (2007). Medical diagnostic applications and sources. *Progress in biophysics and molecular biology*, **93**(1-3), pp. 84–110.

Wijlemans J., Bartels L., Deckers R., Ries M., Mali W.T.M., Moonen C. and Van Den Bosch M. (2012). Magnetic resonance-guided high-intensity focused ultrasound (mr-hifu) ablation of liver tumours. *Cancer Imaging*, **12**(2), p. 387.

WU F., WANG Z.B., CHEN W.Z., BAI J., ZHU H. and QIAO T.Y. (2003). Preliminary experience using high intensity focused ultrasound for the treatment of patients with advanced stage renal malignancy. *The Journal of Urology*, **170**(6, Part 1), pp. 2237 – 2240. doi: https://doi.org/10.1097/01.ju.0000097123.34790.70. Part 1 of 2.

Wu J. (2002). Theoretical study on shear stress generated by microstreaming surrounding contrast agents attached to living cells. *Ultrasound in medicine & biology*, **28**(1), pp. 125–129.

Wu J. and Nyborg W.L. (2008). Ultrasound, cavitation bubbles and their interaction with cells. *Advanced drug delivery reviews*, **60**(10), pp. 1103–1116.

Xu Z., Raghavan M., Hall T.L., Chang C.W., Mycek M.A., Fowlkes J.B. and Cain C.A. (2007). High speed imaging of bubble clouds generated in pulsed ultrasound cavitational therapy-histotripsy. *IEEE transactions on ultrasonics, ferroelectrics, and frequency control*, **54**(10), pp. 2091–2101.

Yoshizawa S., Takagi R. and Umemura S.i. (2017). Enhancement of high-intensity focused ultrasound heating by short-pulse generated cavitation. *Applied Sciences*, **7**(3), p. 288.

Zhao B., Chen Y., Liu J., Zhang L., Wang J., Yang Y., Lv Q. and Xie M. (2018). Blood-brain barrier disruption induced by diagnostic ultrasound combined with microbubbles in mice. *Oncotarget*, **9**(4), p. 4897.

Zhou Y.F. (2011). High intensity focused ultrasound in clinical tumor ablation. *World journal of clinical oncology*, **2**(1), p. 8.

Chapter 2

Optimisations about hybrid pulse regimen and interlaced B-mode for HIFU monitoring

Many parameters and factors related to HIFU treatment can affect the final ablation performance and its ultrasound monitoring efficacy. This chapter mainly investigates the optimal trade-off between HIFU duty cycle and ablation efficiency, to allow for the interlaced B-mode with proposed active beamforming techniques. Final results mainly include three aspects: The coherent divergent wave imaging was tested as the optimal imaging modality, when considering the Field Of View (FOV) and compounding image quality; A duty cycle of 95% was found to be the optimal trade-off between the minimum impact on lesion formation via the tissue-mimicking phantoms, while providing the sufficient time to perform the interlaced B-mode imaging; Finally, the proposed B-mode beamformer with spectrum equalised techniques shows a robust anti-noise capability while maintaining an efficient computation complexity as delay and sum which gives the potential for real-time monitoring.

2.1 Introduction

In this chapter, the diagnostic transducers (linear and phased) were mounted acutely to the HIFU axis, while with a passive detector was co-aligned with HIFU beam for cavitation monitoring.

As the review stated in 1.3.2, the cavitation particularly when a large boil-

ing population occurs, can generate the hyper-echogenic areas and monitored by B-mode images Coussios et al. (2007); Rabkin et al. (2005). However, the necessity of B-mode is to be interlaced with therapeutic exposure to avoid the HIFU interference, and the conventional B-mode such as line-by-line (typically with approximately 30 Hz frame rate Khokhlova et al. (2006)) which can not efficiently image the transient bubble activities, and allow the bubble dissolve in the interval between HIFU-dead period and B-mode imaging. Normally, the contrast agent/-cavitation can be dissolved between 1 and 30 ms, which is shorter than the time to the formation a conventional B-mode image Uhlendorf et al. (2000). Additionally, when the image is acquired by a phased array, the limited physical dimension may not provide a sufficient field of view for imaging. All of these bring up the concern about the chosen of the optimal interlaced B-mode modalities via phased array considering its potential impact (high frame rate with finer image quality and field of view) on treatment monitoring. So that Linear Imaging (LI), coherent Compound Plane Wave Imaging (CPWI), Divergent Wave Imaging (DWI), and Coherent Divergent Wave Imaging (CDWI) performance were compared with identical conditions to select one efficient modality in conjunction with HIFU therapy. Moreover, HIFU duty cycle Hölscher et al. (2013) would compromise the effect of ablation efficacy while providing the HIFU-off opportunity for the data acquisition time of B-mode and time gap setting (to minimise the HIFU interference on B-mode). Therefore, the effect of the varied HIFU duty cycles ($80 - 100\%$) on the lesion size was investigated. Finally, a non-linear beamformer with spectrum equalised techniques in the whitened domain was further considered for the interlaced B-mode to improve the image quality and reduce the interlaced time (i.e., with fewer compound angles as each steered image is improved), and hence, maximise the hybrid pulse efficiency.

The chapter is organised as: section 2.2 test four image qualities via phased array on CIRS standard phantom CRIS2 (2022) in terms of FOV, image quality (contrast-to-noise ratio, lateral and axial resolutions), section 2.3 explore an optimal duty cycle by repeating HIFU exposures with groups of peak negative pressures via polyacrylamide and BSA phantoms and section 2.4 illustrates the proposed whiten-domain beamformer in time and frequency domain and its comparison with other beamforming algorithms in simulation and experimental way.

2.2 Optimising imaging parameters for interlaced B-mode

A 64-element phased-array (IP-105 SN:114, centre frequency 5MHz, bandwidth from 2.28 MHz to 9.10 MHz, pitch width 0.15 mm, Sonic Concepts, USA) transducer was evaluated with four image modalities, (1) linear imaging (LI) with line-by-line focused beam, (2) coherent plane wave imaging (CPWI), (3) divergent wave imaging (DWI) and (4)coherent divergent wave imaging (CDWI). For each of these modalities their FOV, spatial resolution and SNR, were evaluated for a fixed acquisition time. The linear imaging (LI) was transmitted by the focused beam with a specific aperture size (32 in this research) and then beamformed line-by-line Jensen et al. (2006); Rabkin et al. (2005). The coherent plane wave image (CPWI) Gateau et al. (2011) was full-element planar transmission for each time, then compound different angles into one frame for the image quality improvement. Divergent wave imaging (DWI) Papadacci et al. (2014); Zhang et al. (2016) was designed to transmit the focused beam each time with full-element in different steering angles. Finally, every focused beam in different steered angles was beamformed into lines and composed into one image. Coherent divergent wave imaging (CDWI) Escudero et al. (2018) was the full-element planar beam in divergent mode with different steered angles, and each steered divergent mode was beamformed into one frame and average them into one frame.

2.2.1 Method and metrics

The phased array was connected to the house-developed Ultrasound Array Research Platform (UARP) Cowell et al. (2013); Smith et al. (2013, 2012). A multi-purpose, multi-tissue ultrasound phantom (040GSE, CIRS) with attenuation 0.5 dB/[Mhz cm] was used to provide a validated reference target for all imaging modalities. The centre frequency of transmission was 5 MHz with 4 cycle Hanning apodized sine wave. The imaging depth was 75 mm with sampling frequency 40 Mhz. A pulse repetition frequency (PRF) of 2 Khz was chosen to take account of the round trip time of the ultrasound wave (sound speed = 1520 m/s in phantom) to ensure there was no aliasing between each transmission. The focal depth for the focused beam of LI and DWI was 30 mm, respectively. For CPWI, the compounding angles were set from -2° to 2°, with 0.2° as one step. The CDWI was beamformed with span angle 30° and lateral step is 0.5°, and compounded from -10^{0} to 10^{0} with step angle 0.5^{0}.

The total data acquisition time was set as 2700μs (to simulate a data acquisition time of interlaced B-mode within HIFU-dead period), which was kept identical for all imaging modalities, so that the total beamformed lines (i.e. each beamformed line is one transmission) in LI and DWI were the same as the total number of steering angles for CPWI and CDWI (the total line number in LI and DWI was 27 which stays same for compounding angles in CPWI and CDWI.). All radio frequency (RF) data for different modalities was beamformed using delay and sum (DAS) Klemm et al. (2008), with a speed of sound (1480 m/s). The lateral and axial resolutions (LR, AR) for the different imaging modalities were measured by the full width at half maximum (FWHM) (-6 dB). The contrast-to-noise ratio (CNR) Moubark et al. (2016) was defined as:

$$\mathrm{CNR} = 20 * \log_{10}\left(\frac{|\mu_{\mathrm{sig}} - \mu_{\mathrm{noi}}|}{\sqrt{(\delta_{\mathrm{sig}}^2 + \delta_{\mathrm{noi}}^2)}}\right). \tag{2.1}$$

Where μ_{sig} and μ_{noi} are the mean of the total pixel values of the noise and signal region of interest (ROI) at the same depth, the δ_{sig} and δ_{noi} are the standard deviation of pixel amplitude within the noise and signal ROI, respectively, after Hilbert transform but before logarithmic compression.

2.2.2 Results

Figure 2.1 shows four imaging modalities with the same total DAT, and Table 2.1 gives their quantitative evaluation.

	LI	CPWI	DWI	CDWI
FOV	742.5 mm^2	742.5 mm^2	2943.8 mm^2	8831.3 mm^2
DAT	2700 μs	2700 μs	2700 μs	2700 μs
CNR	–	–	10.2 ± 0.1 dB	11.1 ± 0.1 dB
LR	–	–	1.96 ± 0.02 mm	2.31 ± 0.01 mm
AR	–	–	0.4 ± 0.1 mm	0.4 ± 0.1 mm

Table 2.1: Comparisons within four imaging modalities

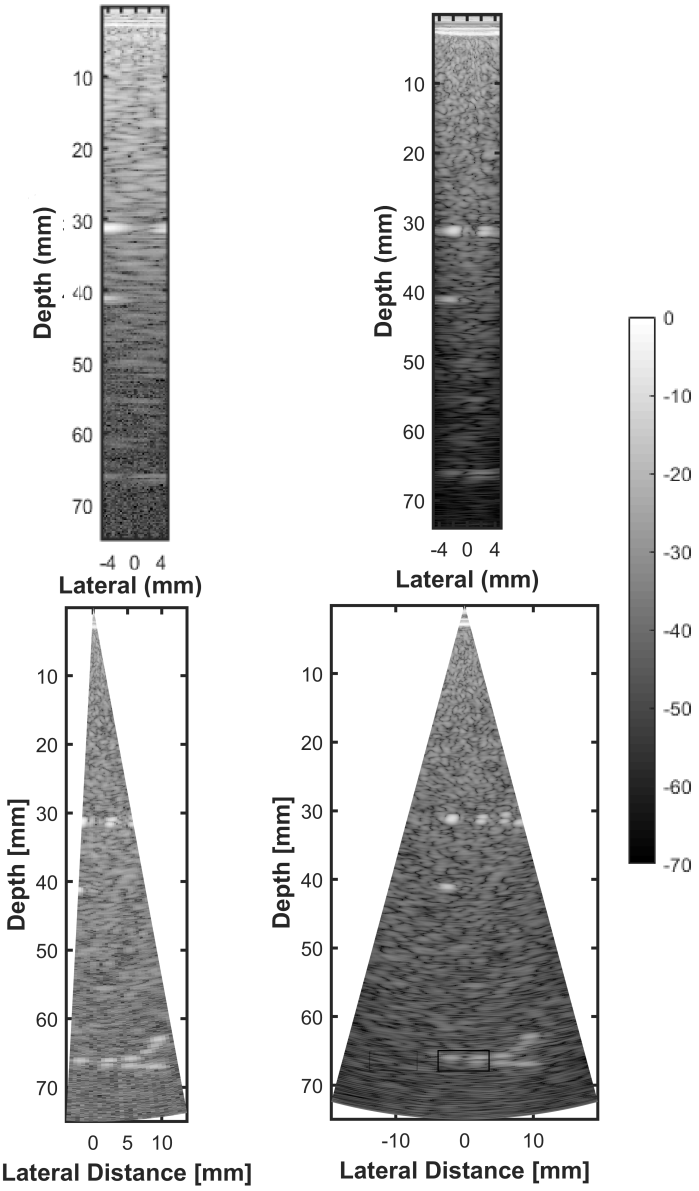

Figure 2.1: Linear wave (top left), coherent plane wave with 27 angles (top right), divergent linear wave with 27 lines (bottom left), coherent divergent plane wave with 27 angles (bottom right) (the rectangular regions indicate for the CNR calculation).

The phased array with 64 elements determines the FOV of LI and CPWI was limited ($742.5mm^2$) (and its maximum physical lateral size was about $12mm$). The hyperechoic region in the interlaced B-mode could commonly reach beyond $10mm$ Rabkin et al. (2005); Silverman et al. (2006) on lateral size, which reveals that neither LI nor CPWI on a phased array was the optimal choice for ultrasound monitoring. Due to the limited FOV of LI and CPWI, the CNR, LR and AR were not displayed in the table. CDWI shows a slight improvement on CNR and approximately three-folds of FOV compared with DWI, for a fixed total DAT. Finally, It was demonstrated that CDWI had the best FOV at approximately $8089mm^2$, and CNR reached 11dB, while keeping resolution at a comparable level as DWI. The next step is to interlace the CDWI into HIFU exposure for the exploration of an optimal duty cycle for the ablation performance.

2.3 Optimisation of HIFU exposure for diagnostic ultrasound guidance

HIFU with continuous wave (CW) excitation could provide the maximised ablation performance. However, the necessity of B-mode to be interlaced with HIFU which required the excitation should be pulsed with a certain duty cycle. Decreasing the duty cycle could maximise the ablation performance while may facilitate insufficient time for B-mode formation. Therefore, identifying the optimal relationship between duty cycle and lesion size (ablation performance) becomes essential. In this section, the relationship between duty cycle and lesion size with different negative peak pressures is discussed. Following the previous section, the CDWI B-mode was interlaced with HIFU exposure, and passive acoustic detection (PCD) was paralleled with sonifications to monitor the inertial cavitation activity. Finally, a hybrid HIFU pulse regimen with a confirmed duty cycle for treatment and monitoring was proved and laid a foundation for the next few chapters' study.

2.3.1 Methods and materials

Experimental setup

For imaging sequence (transmitted by the phased array (IP-105 SN:114, centre frequency 5 MHz, 64-element and pitch width $0.15mm$) and connected to the house-made system Ultrasound Array Research Platform (UARP)), the centre frequency was 5 MHz with a pulse length of 4 cycles and the pulse repetition frequency

(PRF) was $10e^3$, the sampling rate was 40 MHz. The span angle of CDWI was 30° and steering from −10° to 10° by a step angle of 0.5°. The diagnostic array was set up perpendicularly to the axial HIFU beam to co-align them as shown in Figure 2.2, and this allowed a co-axial PCD to be located in the middle of the HIFU transducer.

To synchronise between imaging and therapy parts, an external trigger from the UARP was used to activate a Quantum Composer (QC) system (9250 Digital Delay Pulse Generator, 4 Independent Channel Outputs, MT, USA), and then to generate the Transistor–transistor logic (TTL) triggers for HIFU activation and PCD data acquisition, while each B-mode transmission from the UARP was internally triggered. The QC-controlled function generator was used to excite a $15s$ duration pulsed signal with duty cycles of 80, 85, 90, 95, 100% separately, which was then amplified by the power amplifier (A300, New York, USA). A single element HIFU transducer (focal depth is 63 mm and radius of curvature region, H-102, Sonic Concepts, WA, USA) was driven at its third harmonic (3.3 MHz), which was used to perform HIFU exposure on the polyacrylamide and bovine serum albumin (BSA) tissue-mimicking phantoms.

A broadband-focused detector (Y-102, Sonic Concepts, WA, USA) was co-aligned in the centre of the HIFU transducer to detect the acoustic emissions during HIFU exposure. This detector was connected to a 5MHz high-pass filter (Allen Avionics, NY, USA), and then a 40 dB pre-amplifier (SPA.1411, Spectrum GmbH, Grosshansdorf, Germany). Finally, the PCD data was recorded by a 14-bit data acquisition card (DAQ) (M4i, Spectrum GmbH, Grosshansdorf, Germany), and all PCD data was processed by MATLAB (MATLAB 2017b, The Math Works, Natick, MA, USA) after the exposure. All exposures were performed in a Perspex water tank, and the water for the HIFU experiment was degassed at room temperature ($20 \pm 2°C$). A 1 mm spherical alignment target was used to ensure the HIFU transducer, PCD and diagnostic imaging probe were all aligned, more details about the process can be seen in McLaughlan (2018).

Alignment of ultrasound probe, PCD and HIFU systems

The HIFU transducer was positioned at one side of the transparent water tank hanging in the degassed water via CNC, while the PCD detector was coaxial in the middle of the HIFU transducer. The BSA tissue-mimicking phantom was mounted to the HIFU transducer with the distance of $63mm$ (focal depth). A $1mm$ ball bearing was put in the middle of the phantom right as the indicator to adjust

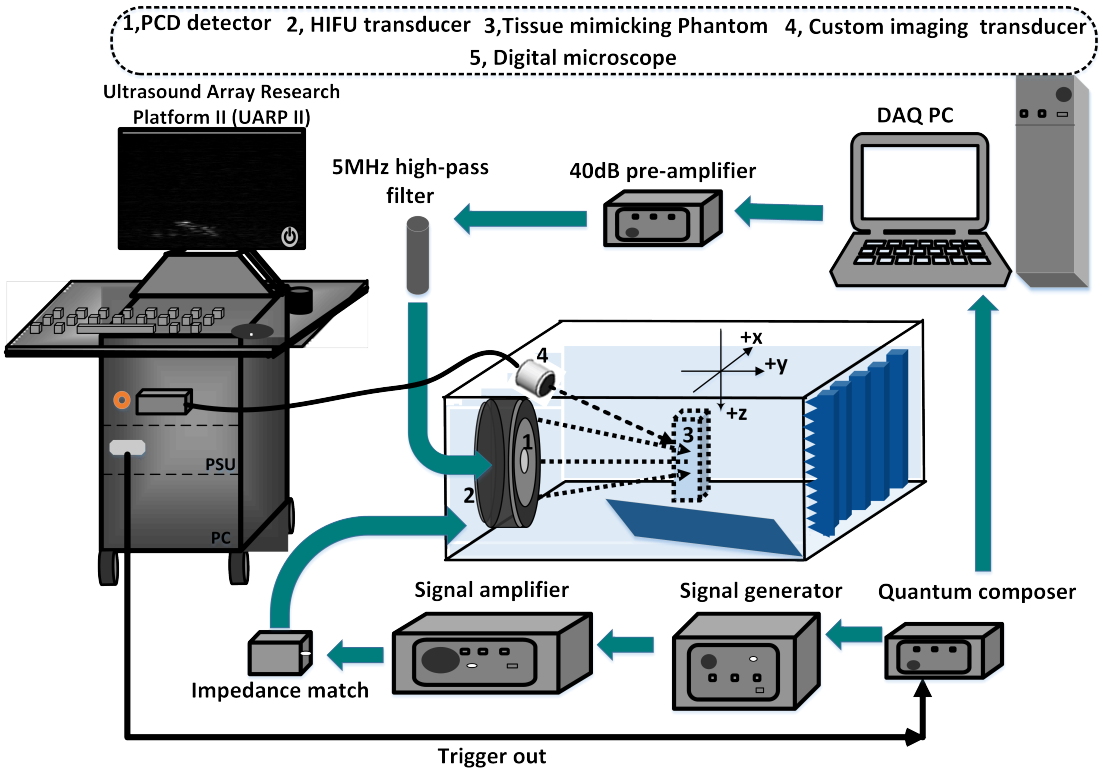

Figure 2.2: Hybrid experimental system schematic (the HIFU transducer with diagnostic array was in an acute mode).

the alignment. After that, the HIFU transducer was connected to the impedance match circuit and power amplifier. The PCD detector was connected with the high-pass filter, pre-amplifier, and DAQ system. After the above connections, the signal generator transmitted a sine wave with 25 Mv, 10 cycles in the driven frequency 3.3 MHz, and the PRF was 100 Hz. Note that the amplitude of excitation signal should not be set beyond the peak-to-peak (PP) limitation of the amplifier (A300, New York, USA) 450 Mv, in case of saturation. The echo from the ball bearing was then passively received by the DAQ software. The HIFU transducer or phantom was adjusted to make the time of flight around 42 μm, and the micrometer stage was shifted in +X, -X, Z directions separately to maximise the echo amplitude. The imaging probe and HIFU transducer were fastened on the same CNC system. B-mode in CDWI was used to monitor the ball bearing to adjust the angle between the HIFU transducer and imaging probe and then co-align them. Moreover, a noise-canceling material was laid under the phantom while setting up a specific angle at the bottom of the water tank to reduce the ultrasound reflection, as shown in Figure 2.2. A microscope (AM4113TL, Dino-lite, New Taipei city, Taiwan) was used to monitor the lesion formation at the beginning of each HIFU-dead period. It was positioned perpendicularly to the phantom at +X or -X side. The ball bearing in the middle of the phantom could also be imaged by the microscope as an indicator to adjust the alignment. Finally, once all these procedures above were confirmed, the signal generator was connected to the QC and kept the phantom position while replacing it with the BSA phantom without the ball bearing for the HIFU experiment. All phantoms were manufactured according to the previous method McLaughlan et al. (2017).

Pulse regimens for interlaced diagnostic and therapeutic ultrasound

The schematic of the hybrid sequence as shown in Figure 2.3 shows the timing between PCD acquisition, CDWI, and pulsed HIFU exposure with a varying duty cycle. CDWI was compounded with 27 steered angles (followed the previous section) during the HIFU-off time to monitor for any increase in hyperechogenicity Anand and Kaczkowski (2004).

The HIFU exposure had five duty cycles (100%, 95%, 90%, 85%, 80%, the duty cycle was varied by applying different HIFU-off time with the fixed HIFU-on time for each repetition) and all at five different peak negative pressures (PNP) (1.43, 1.69, 1.92, 2.13, 2.34MPa) (equivalent approximate free-field averaged spatial peak intensity of 900 $\mathrm{W\,cm^{-2}}$ to 1950 $\mathrm{W\,cm^{-2}}$ $\pm$ 6 %), respectively. Each duty cycle with

different PNP were repeated for three times. The HIFU exposure duration was 15s and divided with 250 times, so that a single therapy/imaging sequence lasting 600 ms, as depicted in Figure 2.3.

Two delays/time-gaps were set up by QC for each HIFU period/repetition. The first one was set 0.1 ms after B-mode acquisition before the onset of HIFU to spare enough temporal time for the last steering of B-mode. The second delay was 0.2 ms between the end of HIFU and before the B-mode transmissions. The aim of both delays was to prevent interference from the HIFU exposure on the final CDWI image (the delays could be adjusted flexibly based on the varied parameters of HIFU exposure and medium characters to better reject the sonification interference for B-mode).

The PCD sequence was recorded 50μs before and after HIFU. A comb filter was used to filter the super- and ultraharmonics and preserve the broadband noise Chen et al. (2003); McLaughlan et al. (2010) for the inertial cavitation monitoring. The frequency analysis of the broadband noise was performed by subdividing the available bandwidth into 100 μs as one segment. The filter spectral bandwidth ranged from 5 MHz to 20 MHz in the frequency domain. Finally, the components were integrated over the whole HIFU exposure duration and named as the Inertial Cavitation Dose (ICD) McLaughlan et al. (2010).

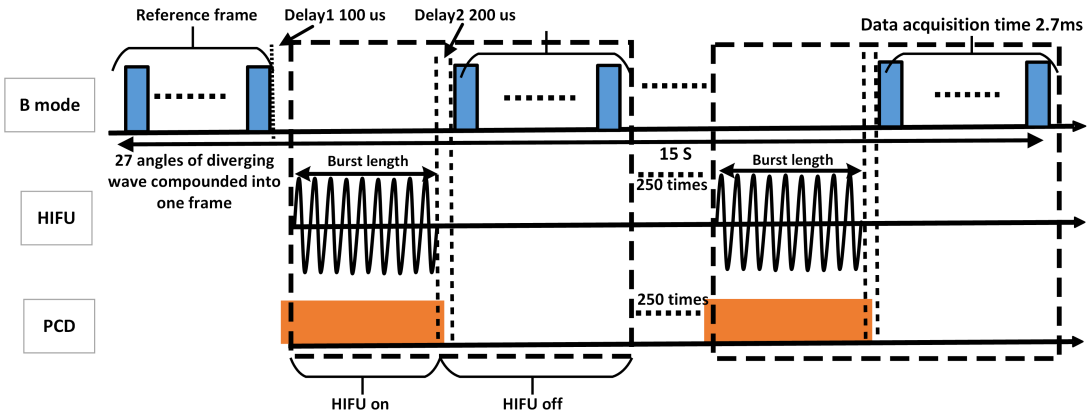

Figure 2.3: Hybrid HIFU pulse regimens (duty cycles: 100%, 95%, 90%, 85%, 80% with PNPs: 1.43, 1.69, 1.92, 2.13, 2.34 MPa).

2.3.2 Results and Discussion

Figure 2.4 shows the picture of the ablation sites on the polyacrylamide phantom and the evolution plots of the hyperechoic region by CDWI (one group among the test results with a duty cycle of 85% and PNP of 2.13 MPa). The original ultrasound image is shown in Figure 2.4 ($0s$), with the HIFU focus at the onset of exposure and before the hyperechoic region could be visualised within the white circle area. The hyperechoic regions indicated by the white arrows represent the exposure with duty cycles of 95% and 90%. The hyperechoic region occurred at about $1s$ and then grew towards the face of the HIFU transducer throughout the remainder ($5s, 10s, 15s$) of the exposure. Furthermore, an artefact appeared in the middle of B-mode and gradually became stronger with the exposure working on the phantom. Reasons for this might be explained by the reflection of the phantom holder (1.75mm 3d Printer Filament Blue, 600g Abs, Cel-Robox, Rbx-Abs-bl824) and the interference from HIFU. Figure 2.5 shows the example of broadband information from a $15s$ exposure at a PNP of 2.13 MPa with a duty cycle of 85%. Inertial cavitation information appeared approximately at $2s$, which is later than the occurrence of the hyperechoic region in the B-mode. One likely cause for this delay might be the difference of the propagation path between the emissions generated from HIFU focus to the PCD detector and diagnostic probe. Then, the inertial cavitation information increased sharply after $3s$ while the size of the hyperechoic region grew significantly. This matches the results from Hynynen (1991) and Coleman et al. (1996), in which the rapid growth of a hyperechoic region was correlated to the amount of scattering from the gas, vapour and/or boiling bubbles generated at the HIFU foci during cavitation in HIFU or lithotripsy treatments. The upper insets in Figure 2.5 are the interlaced B-mode images at different times within the focal area to show the evolution of the hyperechogenicity.

Figure 2.6 shows the lesion area as a function of duty cycle for equivalent acoustic pressures. For all duty cycles, lesion size had an increasing trend with the increase in PNP (equivalent free-field averaged spatial peak intensity shown aforementioned). Duty cycles of 100% and 95% had a more outstanding ablated performance on the whole period. After the PNP had reached to 1.92MPa, the superiority of ablated performance of 100% and 95% duty cycles was more significant. This data suggest that when the duty cycle is below 95%, heating efficacy could be dropped by folds. Meanwhile, the data also indicate that a 95% duty cycle is an optimal choice for the interlaced B-mode, as this duty cycle gives enough

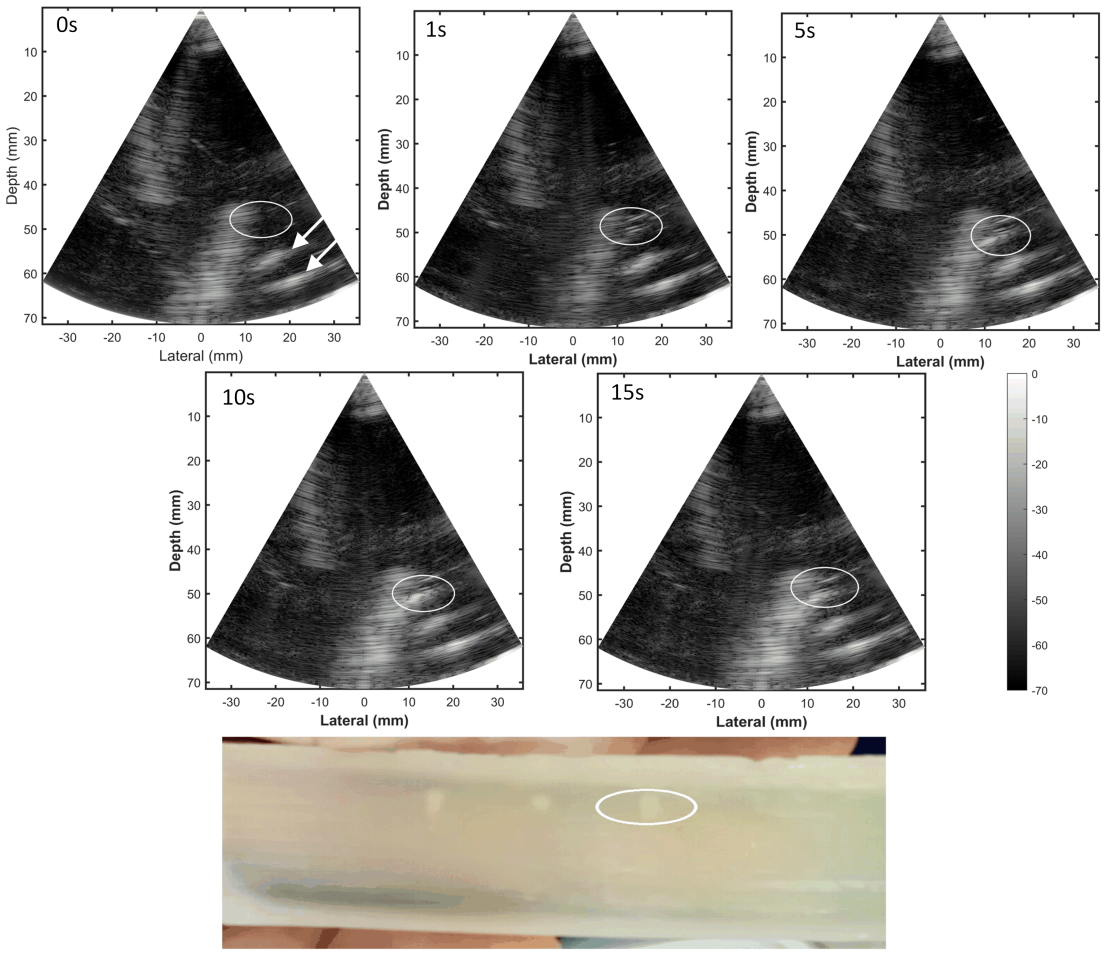

Figure 2.4: The evolution of hyperechoic region displayed by the interlaced B-modes and its final lesion picture.

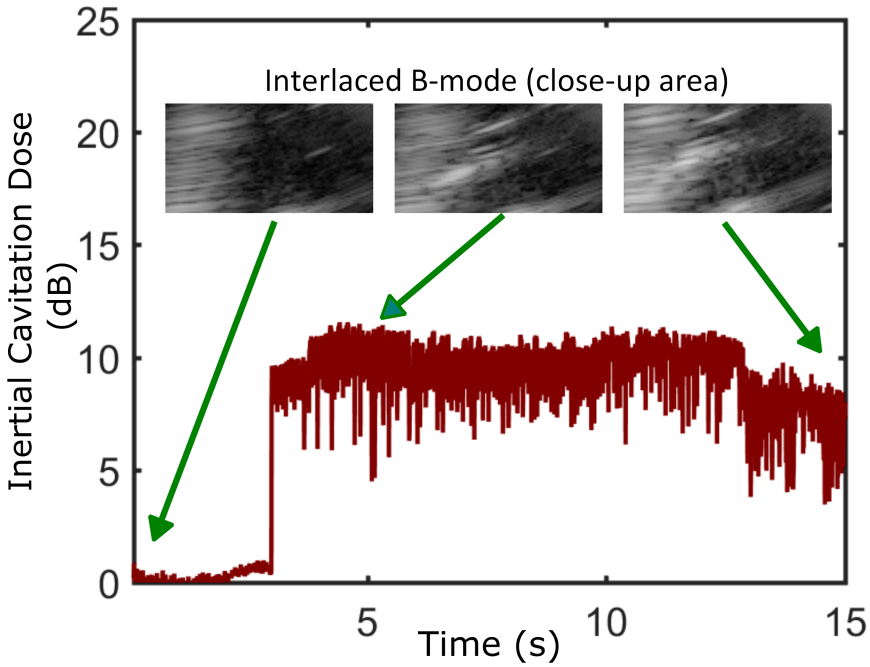

Figure 2.5: Inertial cavitation dose for a 15s exposure, the upper insets showing the interlaced B-mode at 0s, 5s and 15s.

time for the B-mode data acquisition while not sacrificing the therapy performance significantly. The upper-right inset in Figure 2.6 which is recorded by microscope immediately after HIFU exposure, shows the thermal lesion at the focal point. The microscope was positioned at -X side about 4cm from the water tank perpendicular to the HIFU axial (Y-axis), as shown in Figure 2.2.

The detection of the inertial cavitation during HIFU is necessary, as once it occurs, the temperature of the focal zone and lesion could be unpredictable, with the majority ablation moving towards the HIFU source Malcolm and Ter Haar (1996); Meaney et al. (2000); Watkin et al. (1996). In this section, the investigation was done to determine the relationship between the HIFU duty cycle and lesion size that involving with the performance from cavitation (i.e., for inertial cavitation). The complementary work could be emphasised on a clinically relevant threshold for the detection of cavitation. This is important to provide the quantitative parameters for avoiding high-intensity cavitation activities during HIFU thermal therapy, or for the exhibition of cavitation without tissue over-ablation when locating the true HIFU foci before treatment. Moreover, a PCD only provides the information along the HIFU beam axis but weakly locates the cavitation on the HIFU beam lateral, confining it more sensitive in situations such as for subcutaneous

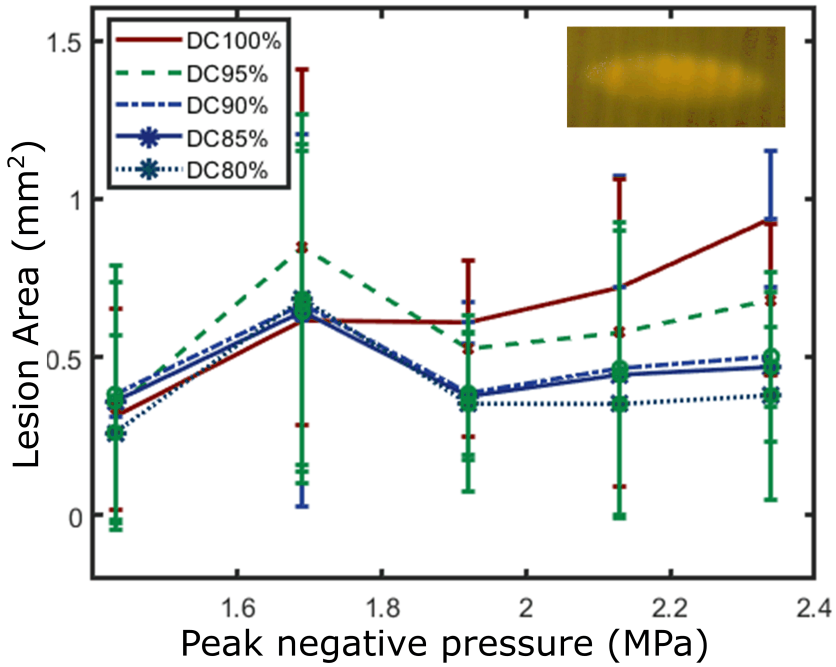

Figure 2.6: The relationship between lesion size and groups of PNP, and tested with different sets of duty cycle and each was repeated with three times. The data was acquired from the system displayed in Figure 2.2. The inset shows the thermal lesion.

tumour treatment monitoring Hu et al. (2007), which was the co-location of the therapeutic ultrasound focus. However, considering both the safety and the dose painting Ter Haar (2016), where the clinician needs to be able to monitor in the regions away from the targeted focus, the ultrasound field, particularly *in vivo*, might be heavily attenuated and lose their focal structure. Due to that, the monitoring methods should ideally always be to 'see' the full treatment path or the conical section generated by the therapeutic ultrasound array. All these inspire the research which is termed as passive acoustic mapping (PAM) Salgaonkar et al. (2009) for HIFU monitoring in the next chapters.

2.4 Spectrum equalised beamforming for the interlaced B-mode suffering HIFU interference

B-mode has been interlaced with HIFU exposures to monitor the hyperechogenicity occurrence McLaughlan et al. (2010); Rabkin et al. (2005). The compounding divergent wave with the conventional beamforming method was demonstrated in

the previous section as an efficient technique for interlaced monitoring. However, the interlaced compounded image may still suffer a heavy interference from HIFU (as shown in section 2.7), even when a time gap is set after the HIFU exposure and before the onset of the B-mode acquisition. Extending the time gap or adding more compounded steering angles into B-mode can improve the image quality while resulting in a lower HIFU duty cycle, which diminishes the ablation performance. A singular value decomposition (SVD) filter was combined into interlace/paralleled B-mode with HIFU exposure, to suppress the ambient interference for hyperechogenicity monitoring Ebbini et al. (2007); Ikeda et al. (2018, 2019). However, due to the stochastic nature of boiling bubbles, the SVD threshold to distinguish the hyperechogenicity and HIFU interference could be varied between frames, which raises the uncertainty (i.e., threshold parameter selection for different frames). Therefore, a robust beamforming method for noise-canceling with computation-efficient speed is critical to maximise monitoring efficiency.

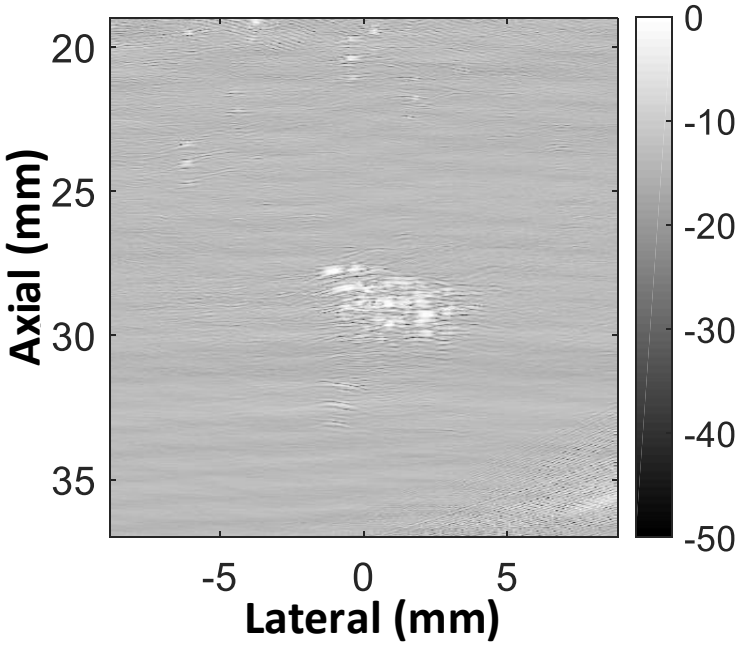

Figure 2.7: A CPWI (via linear array) suffering HIFU interference with five steering angles compounding that interlaced at 4.5 s HIFU exposure. A time gap 1 ms was set after the HIFU exposure and before the B-mode data acquisition.

The delay-and-sum (DAS) algorithm is used to coherently sum the time-delayed RF data in order to amplify the same phased pattern information and suppress the clutter in off-axis. Its simplicity makes it a popular choice for commercial

ultrasound platforms. However, several undesired drawbacks come along with it, such as the clutter from the grating lobe in the near-field and its coherent feature always causing significant noise, particularly if the pulse length is greater than double the pitch size of the transducer Shen and Hsieh (2019). Adaptive weighting techniques Synnevag et al. (2009) were introduced into DAS to improve the image quality while significantly increasing the calculating time, which makes it unsuitable for interlaced B-mode for HIFU monitoring.

Coherent beamforming techniques, such as Delay-Multiply-And-Sum (DMAS) Matrone et al. (2014), have been introduced into B-mode without the need of time-consuming weighting vectors. However, the reconstructed images using DMAS still suffer from the level of side lobes and low noise suppression Mozaffarzadeh et al. (2018). Whitening-related techniques (in time and frequency domains) can be understood as one of the spectral equalisation techniques that has been used in the seismic Helmore (2009) and radar fields Xie et al. (1998) for super-resolution and noise-suppression trials. In this section, whitening techniques were introduced into efficient-calculating DMAS related beamformers. Also, the Cepstrum-based deconvolution Taxt (1997) combined into DMAS was explored due to the deconvolution is one of the classic spectral equalisation techniques that has been widely applied in B-mode Yu et al. (2012). Here, it was used for a full comparison with whitening-related techniques. Finally, the proposed beamforming method was implemented with interlaced B-mode imaging, aiming for efficient HIFU hyperechogenicity monitoring.

2.4.1 Algorithm

In this section the following spectrum equalisation techniques are analysed; 1) three kinds of time-domain whitening transformations (TWDMAS), including the zero-phase component analysis whitening based DMAS (ZCADMAS), the Cholesky whitening based DMAS (ChoDMAS) and the variances whitening based DMAS (VarDMAS); 2) one frequency-domain whitening transformation (FWDMAS) combined with DMAS, as proposed beamformers were presented; and 3) the deconvolution DMAS (DCDMAS) based on the conventional Cepstrum method. Finally, the simulation and experiment data settings are given.

2.4.1.A Related work: DAS

In conventional ultrasound (US) imaging, the B-mode beamformer as one of absolute time of flight (ToF) beamforming techniques, two general assumptions initially were made: the ultrasound speed is constant C_o during propagation (1540 m/s in the tissue or 1480 m/s in the water), and the medium is formed by scattering points with spherical spreading. To form an image in x, z dimension [x is the lateral axial and z is the transverse (/depth) axial], the output $\mathrm{I_{DAS}}(x, z)$ represents each line beamformed with RF data $\mathrm{y}_i(\mathrm{t})$ recording by the diagnostics probe with $N = 128$ elements [i is the array index (i=1, 2, 3, ..., 128)]. The ToF information between point (x, z) and the element located at $(x_i, 0)$ is expressed as:

$$t_i(x,z) = \frac{z * \cos(\alpha) + x * \sin(\alpha) + \frac{L}{2}\sin(|\alpha|) + \sqrt{(x - x_i)^2 + z^2}}{C_o}, \tag{2.2}$$

The L represents the aperture size and α is the inclination angle for coherent compounding. The time-delayed information $t_i(x, z)$ helps rephase the RF data. Finally, the coherent summation of the rephased data for the final output can be expressed as:

$$I_{\mathrm{DAS}}(x,z) = \frac{1}{N}\sum_{i=1}^{N} w_i \check{y}_i(t_i(x,z)). \tag{2.3}$$

The w_i is the weighting patterns which are used to better reject the side lobes, and in DAS, which are assumed to be [1, 1....., 1]. The $\check{y}_i(x, z)$ was the rephased RF data $y_i(t_i(x, z))$ being compensated for the loss of source signal strength from spherical spreading of the wave-fronts originating from source r located at (x,z) (e.g. based on the aforementioned assumption illustrated). Here, the $\check{y}_i(t_i(x, z))$ was expressed as:

$$\check{y}_i(t_i(x,z)) = \alpha_i(\hat{d}) * y_i(t_i(x,z)), \tag{2.4}$$

$*$ means convolution, the $\alpha_i(\hat{d}) = \beta((x - x_i)^2 + z^2)$ is a general gain function as to compensate for the signal attenuation on the 'receiving' road (e.g. energy mostly lost by attenuation due to the spherical or geometric spreading). Here, we adopt $\alpha_i(\hat{d}) = \sqrt{(x - x_i)^2 + z^2}$ as a simple version to be implemented in the beamformer.

2.4.1.B Related work: delay-multiply-and-sum (DMAS)

The principle of DMAS is to coherently backpropagate the pixelwise-filtered RF data with time domain migration information into image space. This is assuming a two-dimensional array with N elements recording data $y_i(t)$ (as explained in section 2.4.1.A). Then it coherently back-propagates data $\check{y}_i(t_i(x,z))$ from the scattering source r located at (x,z), which can be expressed as:

$$I_{\mathrm{DMAS}}(x,z) = \frac{2}{N^2-N}\sum_{i=1}^{N-1}\sum_{j=i+1}^{N} sign(\check{y}_i(t_i(x,z))\check{y}_j(t_j(x,z)))\sqrt{|\check{y}_i(t_i(x,z))\check{y}_j(t_j(x,z))|}. \tag{2.5}$$

Equation 2.5 can be decomposed by applying a square root to re-scale $\check{y}_i(t_i(x,z))$, then carry out the cross-correlation:

$$\bar{y}_i(t_i(x,z)) = sign(\check{y}_i(t_i(x,z)))\sqrt{|\check{y}_i(t_i(x,z))|}, \tag{2.6}$$

$$I_{\mathrm{DMAS}}(x,z) = \frac{2}{N^2-N}\sum_{i=1}^{N-1}\sum_{j=i+1}^{N} \bar{y}_i(t_i(x,z))\bar{y}_j(t_j(x,z)). \tag{2.7}$$

Equation 2.7 can be re-formulated with more computation-efficient version by reducing the computation complexity from $O(N^2)$ to $O(N)$,

$$I_{\mathrm{DMAS}}(x,z) = \frac{1}{2N}\left(\left|\sum_{i=1}^{N}\bar{y}_i(t_i(x,z))\right|^2 - \sum_{i=1}^{N}|\bar{y}_i(t_i(x,z))|^2\right). \tag{2.8}$$

Generally, a bandpass (BP) filter could be utilised to retain the second harmonic component into image space, which was not adopted in this research that is aimed at highlighting the only contribution of spectrum equalisation.

2.4.1.C The spectrum Equalised DMAS

The whitening transformation is often applied for ambient vibration data before stacking waveforms for cross-correlation Krzywosz (2015). The general reason for this application is the spectral response after being equalised or flattened over the available bandwidth, which in the spatial domain, transforms into a small point spread function (PSF) response. Therefore, the cross-correlation output of the equalised spectral response could be approached as quasi-Dirac shape with narrow PSF size. The aforementioned was proposed by the whitened DMAS techniques.

Assuming the RF data matrix $\mathbf{Y}$ is composed of K dimensions and i observations, so that the matrix $\mathbf{Y}$ has size $[k * i]$. Generally, the standardisation and whitening transformations are accompanied by mean-centring each row data Eldar and Oppenheim (2003). Therefore, the corresponding mean value has been detrended from each observation. The detrended RF data $y_{(de)i}(t)$ is then being compensated by equation 2.4 and re-aligned following the procedure in section 2.4.1.A. The re-aligned vector $\check{y}_{(de)i}(t_i(x,z))$ will project into whitening domain for beamforming,

$$\check{y}_{(\mathrm{whi})\mathrm{i}}(t_i(x,z)) = \mathbf{W} * \check{y}_{(de)i}(t_i(x,z)), \tag{2.9}$$

The ideal statistical whitening matrix $\mathbf{W}$ is a linear transformation that transforms a vector of random variables into a set of new variables whose covariance is the identity matrix. The transformation mainly contains decorrelated and sphering features (an example shown in Figure 2.8), which is called 'whitening' because it changes the input 'coloured' vector into a white noise vector.

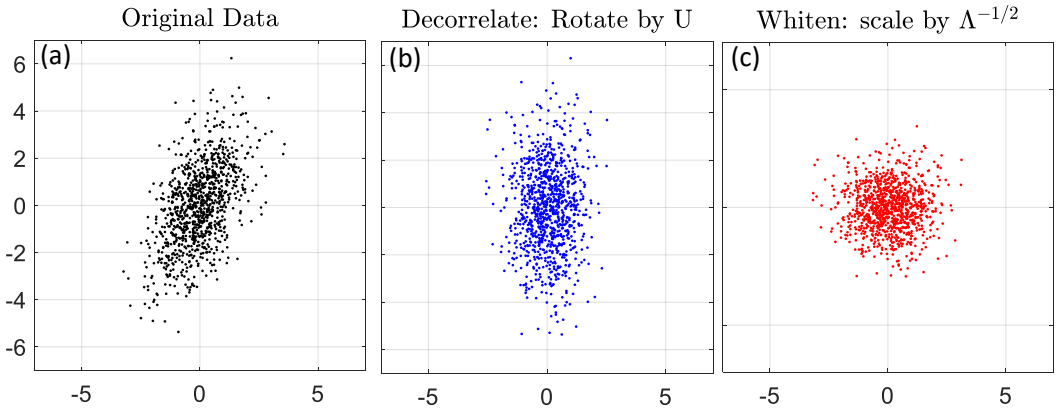

Figure 2.8: (a) Randomly distributed point data. (b) Data decorrelated by its eigenvectors U of covariance matrix. (c) decorrelated data whitened by the square rooted diagonal matrix $\Lambda^{-1/2}$.

In this research, three kinds of whitening matrix transformations were given Kessy et al. (2018). The first one belongs to the zero-phase component analysis (ZCA) whitening, which can be expressed as:

$$\mathbf{W}_{\mathrm{ZCA}} = \mathbf{U}\left(\Lambda + \Delta * tr(\mathbf{R}) * \mathbf{I}\right)^{-1/2}\mathbf{U}^{T}, \tag{2.10}$$

Where $\mathbf{R}$ is the covariance matrix of $\bar{y}_{(de)i}(t_i(x,z))$, the $tr\{.\}$ is the trace operator and Δ is a constant number. The aim of component $\Delta * tr(\mathbf{R}) * \mathbf{I}$ is to keep $\mathbf{W}_{\text{ZCA}}$ positive for its robustness. The $\mathbf{U}$ is the eigenvectors of $\mathbf{R}$ and Λ is the eigenvalues. T represents the transpose.

The second whitening matrix transformation is the Cholesky whitening. The robustness of covariance matrix $\mathbf{R}$ still compensates by $\Delta * tr(\mathbf{R}) * \mathbf{I}$. The data $\check{y}_{(de)i}(t_i(x,z))$ is then whitened by $\sqrt{\mathbf{R}}$. The calculation of $\sqrt{\mathbf{R}}$ by using Cholesky decomposition where:

$$\mathbf{R} = \mathbf{L} * \mathbf{L}^T, \tag{2.11}$$

The whitened transformation matrix is given by:

$$\mathbf{W}_{\text{chole}} = \mathbf{L}^{-1}, \tag{2.12}$$

The $\mathbf{L}$ is the lower triangular which can efficiently be solved out without forming the inverse.

The above two involved with the calculation and decomposition of covariance matrix $\mathbf{R}$ which could increase the expense of computation. The third one was designed with less complexity that can be illustrated as:

$$\mathbf{W}_{\text{var}} = {\mathbf{V}_{\text{var}}}^{-1/2}, \tag{2.13}$$

Where $\mathbf{V}_{\text{var}} = diag(\delta_1^2, ..., \delta_i^2)$ is composed of the variances $\text{var}(\check{y}_{(de)i}(t_i(x,z))) = \delta_i^2$. This results in $\text{var}(\check{y}_{(\text{whi})\text{i}}(t_i(x,z))) = 1$. The covariance matrix $\mathbf{R}$ calculation in the $\mathbf{W}_{\text{var}}$ was not needed which which makes the process can be computation-efficiency, while the corresponding drawback of $\mathbf{V}_{\text{var}}$ is performed without data decorrelation.

The frequency domain whitening transformation $\mathbf{W}_{\text{fre}}$ was developed either for the full range of frequency bandwidth or for an interested frequency band. The frequency whitening operation can be understood as first applying the Hanning window to the input vector $\check{y}_{(de)i}(t_i(x,z)$, then 128 points Fourier transforming the apodized signal, scaling the magnitude in the interested bandwidth to 1, and finally inverse Fourier transforming it into time domain Dr. Erol Kalkan (2022).

After projecting the data $\check{y}_{(de)i}(t_i(x,z)$ into whitening time domain, the re-aligned waveform will be stacked for the cross-correlation, which can be expressed

as:

$$\bar{y}_{(\mathrm{whi})\mathrm{i}}(t_i(x,z)) = sign(\check{y}_{(\mathrm{whi})\mathrm{i}}(t_i(x,z)))\sqrt{|\check{y}_{(\mathrm{whi})\mathrm{i}}(t_i(x,z)))|}, \tag{2.14}$$

$$I_{\mathrm{WDMAS}}(x,z) = \frac{1}{2N}\left(\left|\sum_{i=1}^{N}\bar{y}_{(\mathrm{whi})\mathrm{i}}(t_i(x,z))\right|^2 - \sum_{i=1}^{N}\left|\bar{y}_{(\mathrm{whi})\mathrm{i}}(t_i(x,z))\right|^2\right). \tag{2.15}$$

For the deconvoluted DMAS, according to the assumptions in deconvolution Jensen and Leeman (1994); Taxt (1997), the power spectrum equalisation principle was applied between the real tissue reflective function $g(x,z)$ and the degraded image $I_{\mathrm{DMAS}}(x,z)$ to reduce the impact from both $h(x,z)$ and $n(x,z)$. The relationship between $g(x,z)$ and $I_{\mathrm{DMAS}}(x,z)$ can be expressed as:

$$I_{\mathrm{DMAS}}(x,z) = h(x,z) * g(x,z) + n(x,z). \tag{2.16}$$

Where the $h(x,z)$ denotes the radial response which contains the response from propagation, transducer, etc. The $n(x,z)$ is the additive noise. $*$ denotes the convolution operation. One typical cepstral-based deconvolution technique belongs to the homomorphic transformation that was performed by the regularised Wiener reverse filtering Taxt (1997), which can be expressed by:

$$G(e^{jw}) = \frac{H(e^{jw})}{|H(e^{jw})|^2 + q}. \tag{2.17}$$

Where the $G(e^{jw})$ and $H(e^{jw})$ is the Fourier transform of $g(x,z)$ and $h(x,z)$; q is the noise to signal ratio which is a regularisation component that determines the stability of the deconvolution solutions and can be generally expressed by: $q = \alpha\frac{S_n(e^{jw})}{S_s(e^{jw})}$. The $S_n(e^{jw})$ and $S_s(e^{jw})$ is the power spectral density of the noise and signal; $\alpha = 0.5$, in this research, as a regularisation parameter.

Finally, The image performance of different algorithms was assessed by the contrast-to-noise ratio (CNR), contrast ratio (CR), and full width at half maximum (FWHM) (at -6 dB for resolution). CNR and CR are given by:

$$\mathrm{CNR} = \frac{|\mu_{\mathrm{i}} - \mu_{\mathrm{o}}|}{\sqrt{(\sigma_{\mathrm{i}}^2 + \sigma_{\mathrm{o}}^2)/2}}, \tag{2.18}$$

$$\mathrm{CR} = \frac{\mu_{\mathrm{i}}}{\mu_{\mathrm{o}}}. \tag{2.19}$$

Where μ_i and μ_i denote the mean pixel amplitude of the two rectangular regions [regions of interest (ROI)], respectively; and σ_i and σ_o represent the standard deviation of pixel amplitude within two ROIs, respectively. These four factors can be illustrated as:

$$\mu_i = \mathrm{E}\left\{\mathrm{p_i}\right\}, \tag{2.20}$$

$$\mu_o = \mathrm{E}\left\{\mathrm{p_o}\right\}, \tag{2.21}$$

$$\sigma_i^2 = \mathrm{E}\left\{(\mathrm{p_i} - \mu_\mathrm{i})^2\right\}, \tag{2.22}$$

$$\sigma_o^2 = \mathrm{E}\left\{(\mathrm{p_o} - \mu_\mathrm{o})^2\right\}. \tag{2.23}$$

Where $E\{.\}$ represents the expectation, and p_i and p_o are the pixel amplitude within two selected ROIs separately. The image amplitude value is after the Hilbert transformation and absolute algebra, before log compression.

Implementation procedures of power spectrum equalised DMAS

(1) The RF data $y_i(t)$ was detrended by the corresponding mean value ($y_{(de)i}(t)$).

(2) The RF data $y_{(de)i}(t)$ was being realigned with time-delay information and compensated by the gain function $\alpha_i(\hat{d})$ (the $\check{y}_i(t_i(x,z))$ in equation 2.4).

(3) For time-domain power spectrum equalisation, the realigned data $\check{y}_i(t_i(x,z))$ convoluted with designed whitening-transforming weighting vector. For frequency-domain power spectrum equalisation, the realigned data $\check{y}_i(t_i(x,z))$ was transformed into frequency-domain, then stabilise the frequency spectrum, finally adopted into time-domain.

(4) Finally, the whitened data performed the cross-correlation calculation (equation 2.15).

2.4.2 Simulation and Experimental Results

In this section, numerical and experimental results are illustrated, firstly, to assess the performance of the proposed method: TWDMAS and FWDMAS. Then the selected ones are compared with DAS, DMAS and DCDMAS.

2.4.2.A Simulation results

Field II simulation was used to simulate the plane wave transmitted by a linear array with 128 elements and a central frequency of 7.5 MHz with a sampling frequency of 40 MHz. The excitation was two-cycle sine-waveform and the impulse response was a two-cycle Hanning-apodized sine-waveform. The attenuation was set at 0.5 dB/[MHz cm] with speed of sound of 1480 m/s.

Time and frequency domain whitened DMAS

Figure 2.9 shows a comparison between ZCADMAS, ChoDMAS, VarDMAS and FWDMAS. All results were simulated via a wire target at the depth of 15.5mm, and imaged by a single plane wave. Gaussian noise was added to the simulations, for a SNR of -20 dB, aiming to simulate a noisy environment analogy to HIFU interference as shown in Figure 2.7. In Figure 2.9, the whitened point scatterer show a different level of background noise, and the tail artefacts occurrence which may come from the generation of DC and higher frequency components by lateral convolution, can be suppressed by applying a twice folds centre frequency bandpass filter (e.g. see section 2.6). Figure 2.9(c, d) displays relatively better lateral resolution than Figure 2.9(a, b), while (c) may suffer a bit of deformation with an energy shift to the right side. To characterise the image quality, Figure 2.10 shows the quantitative measurements that lateral side lobe level of FWDMAS was reduced by approximately 10 dB on average compared with TWDMAS, while the lateral resolution of FWDMAS was slightly higher (i.e. approximately 9%) than VarDMAS and ZCADMAS. The ChoDMAS shows the best lateral resolution with approximately 20% improvement compared with FWDMAS, however, with the strong side-lobe generation as shown in Figure 2.10(b), which matches the possible point scatterer deformation in Figure 2.9(c). Based on the metrics performance of FWDMAS, it was selected for further comparison with different imaging techniques (e.g. DAS, DMAS and DCDMAS).

Different imaging techniques with simulated point scatterer phantom

Figure 2.11 shows the simulated point scatterer images beamformed with different imaging techniques. The FWDMAS provides a finer lateral resolution compared with DMAS, which can be seen in Figure 2.12, that improved by about 8.4%. Whilst, the lateral resolution of DCDMAS shows approximately 16.7% worse than DMAS. This could be caused by the inaccurate estimation of the PSF pulse response function, as shown in Figure 2.13. Figure 2.13(a) is the PSF pulse response

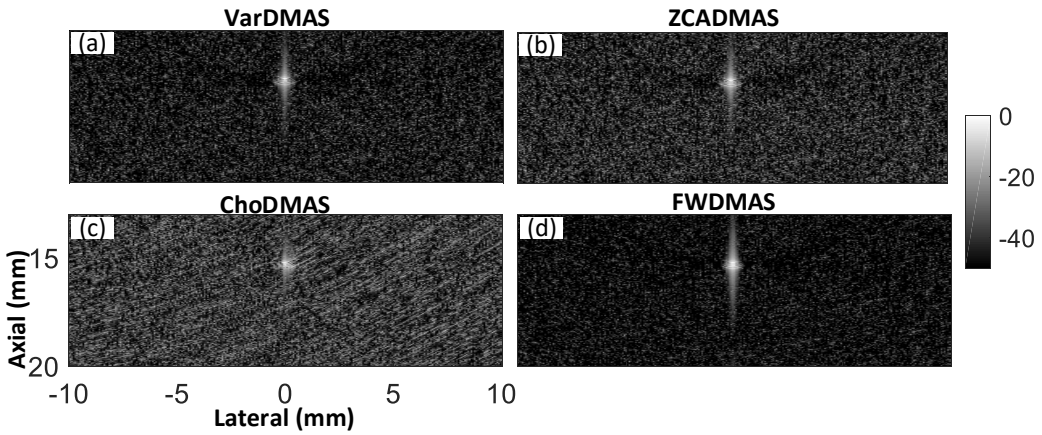

Figure 2.9: A point scattering phantom 'whitened' (a) by $\mathbf{V}_{\text{var}}$, (b) ZCA $\mathbf{W}_{\text{ZCA}}$, (c) Cholesky $\mathbf{L}^{-1}$ and (d) in frequency domain. Noise was added to the RF data, resulting in a signal-to-noise ratio of -20 dB.

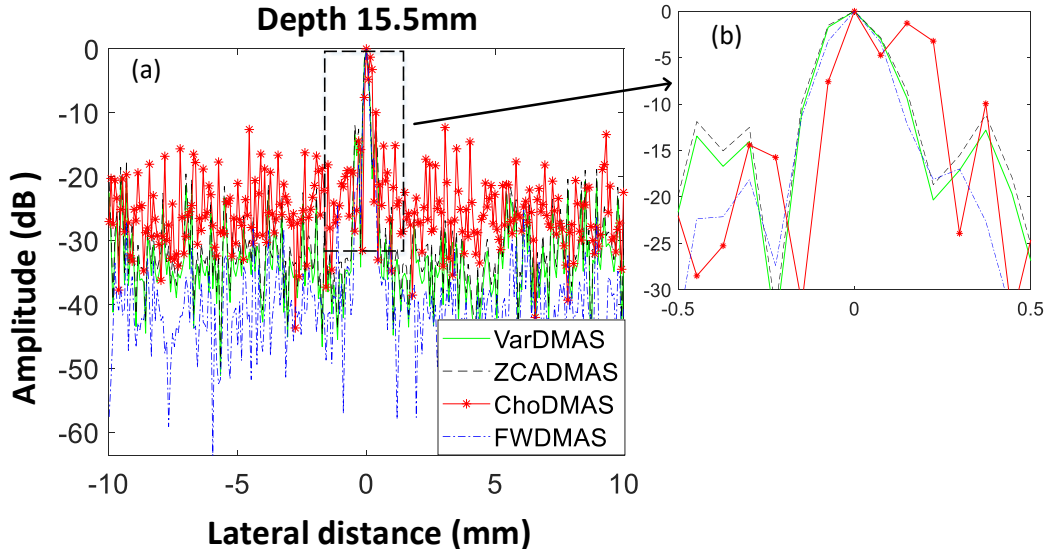

Figure 2.10: Lateral resolution of simulated point scatterer at depth of 15.5 mm by different whitened transformation methods (a). The upper-right corner figure is the enlarged version of the black rectangular region (b).

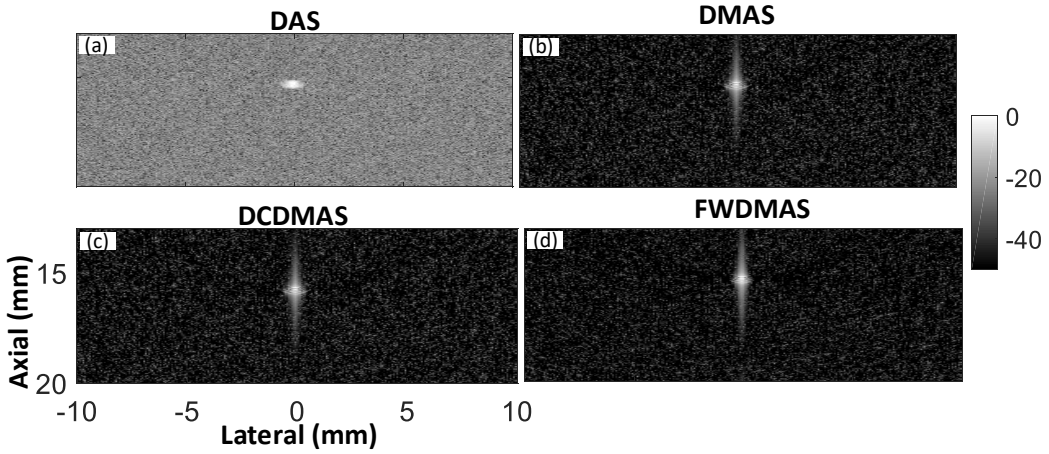

Figure 2.11: Simulated point scatterer phantom beamformed by (a) DAS, (b) DMAS, (c) DCDMAS, (d) FWDMAS. Noise was added to the RF data, resulting in a signal-to-noise ratio of -20 dB.

calculated by 50 axial lines as one window in DMAS and then shifting this window with one axial line as sliding step to get all estimated PSF pulse responses. Finally, they all are averaged into one to get the final PSF pulse response function for deconvolution, as shown in Figure 2.13(b). For the performance of background noise suppression, the DMAS related methods in Figure 2.11(b, c, d) display a better noise-cancelling capability. This can be reflected by image contrast, which is governed by the peak side lobe (PSL). The PSL is defined as the peak value of the first side-lobe Holfort et al. (2009). This is indicated by Figure 2.11(b), where there is approximately 8 dB and 6 dB improvement (i.e. the black bidirectional arrowhead place) by FWDMAS and DCDMAS as compared with DMAS, respectively.

Different imaging techniques with simulated cyst phantom

Figure 2.14 illustrates five groups of cyst phantoms beamformed by aforementioned imaging techniques (DAS, DMAS, FWDMAS and DCDMAS) with different levels of additive noises to simulate the HIFU interference, aiming to test their noise suppression capability. In Figure 2.14, DAS gives the worst performance among all SNR scenarios. For DMAS, FWDMAS and DCDMAS, besides the highest noise situation (SNR = -20dB) that nearly nothing can be visualised, the anechoic area can be more clearly displayed in the image of FWDMAS and DCDMAS than DMAS. This can be demonstrated by the quantitative measurements using

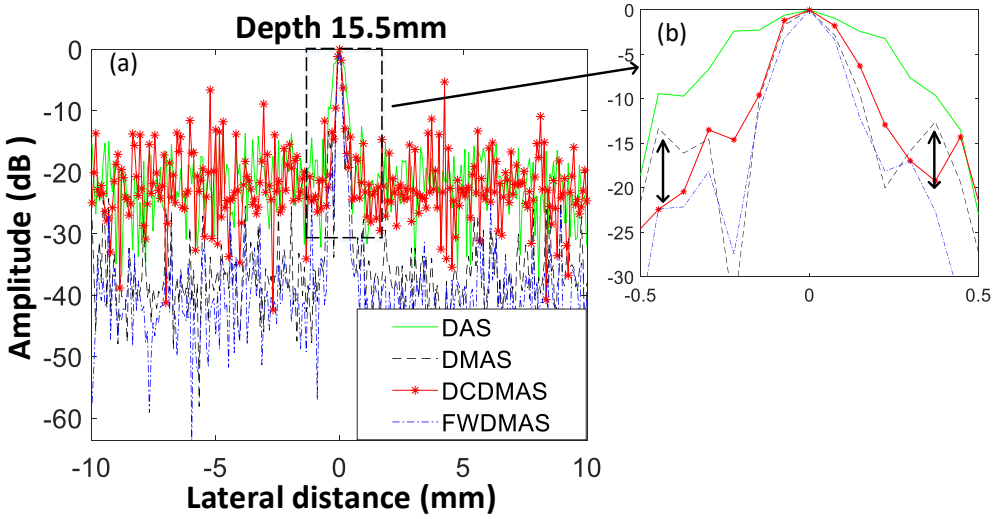

Figure 2.12: Lateral resolution of point scatterer at depth of 15.5 mm by different imaging methods (a). The upper-right corner figure is the enlarged version of the black rectangular region (b).

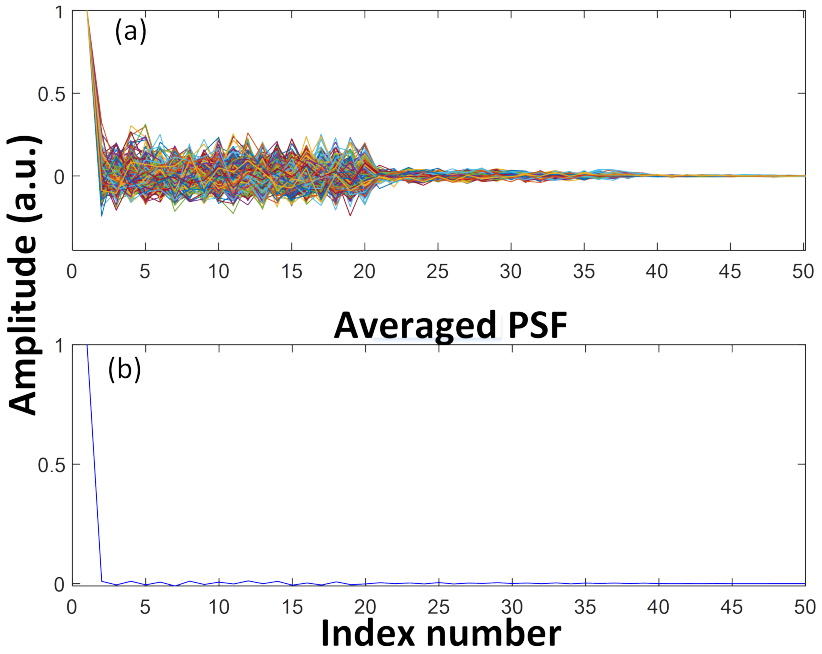

Figure 2.13: PSF pulse response function estimated from DMAS. (a) PSF estimated by each sliding window. (b) Final averaged PSF function for deconvolution.

CNR and CR, as shown in Figure 2.15. Note, due to the worst performance of DAS, its quantitative analysis is not displayed in Figure 2.15. The CNR and CR were measured by equations 2.18 and 2.19. The CNR and CR of DCDMAS under a relatively low noise situation (when without additive noise and with SNR = -10dB additive noise) gives approximately 28.8% and 67.2% averaged improvement compared with DMAS, respectively. Whilst, for a high noise environment (SNR = -10dB and -20dB), the CNR and CR keeps approximately the same level as DMAS [i.e. details also shown in Figure 2.15(a1, b1)]. This unsteady performance can be explained by the results of the blind deconvoluted method strongly relying on the accuracy of the PSF pulse response estimation (the accuracy of blind PSF estimation techniques are beyond the scope of this research, and, therefore, no additional details are discussed herein). Figure 2.14 shows that the PSF pulse response of Cepstrum-based DCDMAS cannot be robustly estimated in the environment with uniform image feature. The inaccurate estimation would result in the PSF pulse response values approaching null, and this trend can also be seen in Figure 2.13. Meanwhile, the CNR and CR of FWDMAS, compared with DMAS, gives a robust enhancement under different noisy scenarios with approximately 14% and 7%, separately.

2.4.2.B Experimental results for the interlaced B-mode

Further testing was performed by the RF data acquired by *in vivo* HIFU experiments. The phantom was the degassed *ex vivo* liver. The B-mode was interlaced with 3.3 MHz centre frequency HIFU exposure and its PNP was 7 MPa. The time gap between HIFU-off and the onset of B-mode data acquisition was set as 1 ms. A similar pulse regimen is shown in Figure 2.3. The linear imaging transducer was 128 elements that was consistent with the simulation setting. The B-mode was transmitted by plane wave with five steering angles from -8^o to 8^o. The centre frequency of the plane wave was 7.5 MHz and its sampling frequency was 40 MHz.

Figure 2.16 shows the results of the interlaced B-mode for HIFU works on *ex vivo* liver phantom that acquired at 5s. In Figure 2.16(b), beamformed by DAS shows significant noise that deteriorates the image contrast even after five steering compounding (a) [i.e. coherent Compounding Plane Wave Imaging (CPWI)]. In Figure 2.16(c, d), the random scatters in the phantoms can be visualised; however, the noise that occurs in the format of the horizontal stripes still exists in the B-mode [i.e. Figure 2.17 is the PSF pulse response function measured from DMAS

of Figure 2.16(c)]. In Figure 2.16(e), FWDMAS provides clear ambient noise suppression in the entire image. To quantify the clutter level of Figure 2.16, the ROI regions are indicated in Figure 2.16(b) for comparison. In Figure 2.18(a, b), the DMAS did not show the improvement on CR and CNR compared with DAS, which might cause by the image intensity loss and increased speckle variance Matrone et al. (2014). Meanwhile, the FWDMAS demonstrated about 69% and 125% increase in CNR and CR over DMAS, respectively. The DCDMAS shows about 37% improvement in CNR and CR as compared with DMAS.

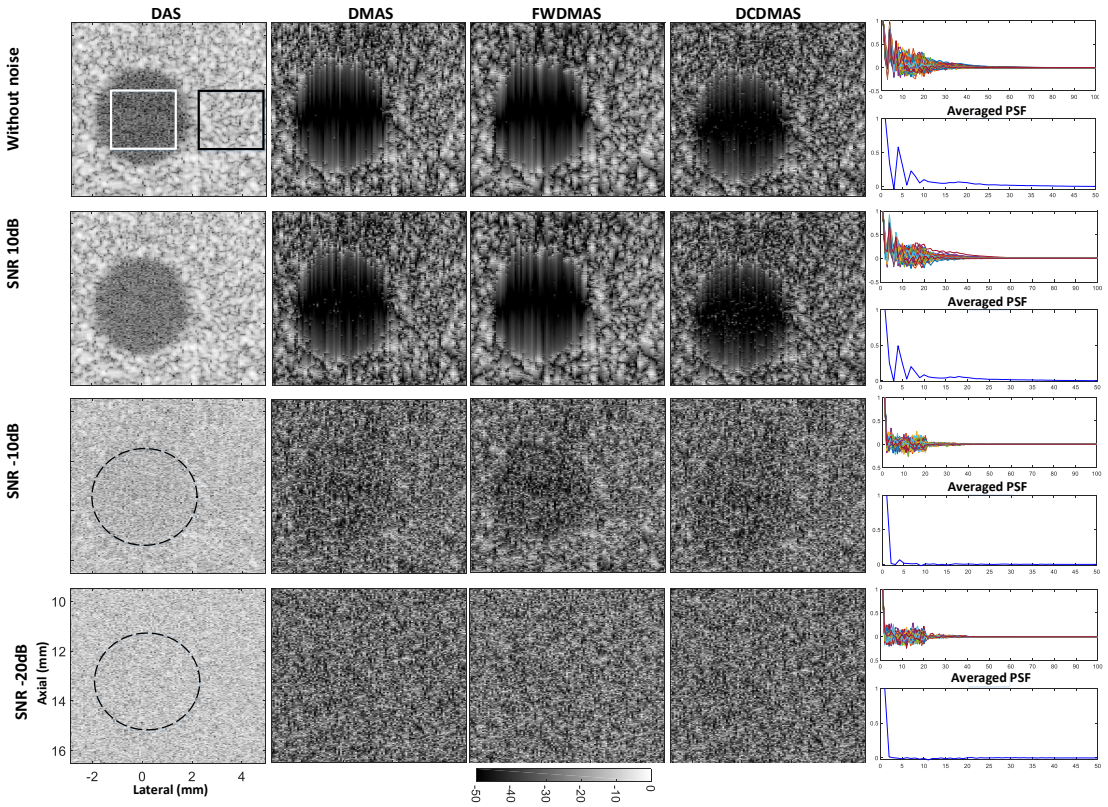

Figure 2.14: Five groups of simulated anechoic cysts imaged using DAS, DMAS, FWDMAS and DCDMAS (with estimated PSF pulse responses) by a single plane wave. The images are displayed without and with random noise for the signal-to-noise ratio of 10, -10, -20 dB, respectively. The white and black rectangles in DAS without noise denote the ROIs used for measuring the CNR and CR. The white rectangle encloses the region inside the cyst, while the black rectangle encloses the region outside the cyst.

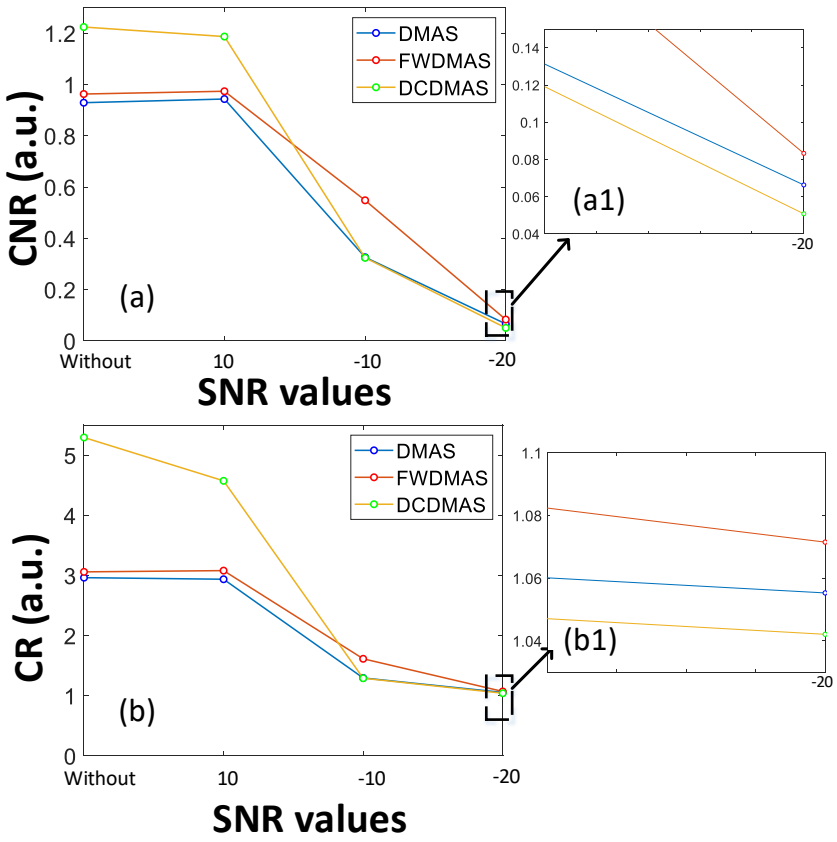

Figure 2.15: The (a) CNR and (b) CR measurements of the simulated cyst with different levels of noise. (a1) and (b1) are the enlarged areas of CNR and CR at rectangular place when SNR is -20dB.

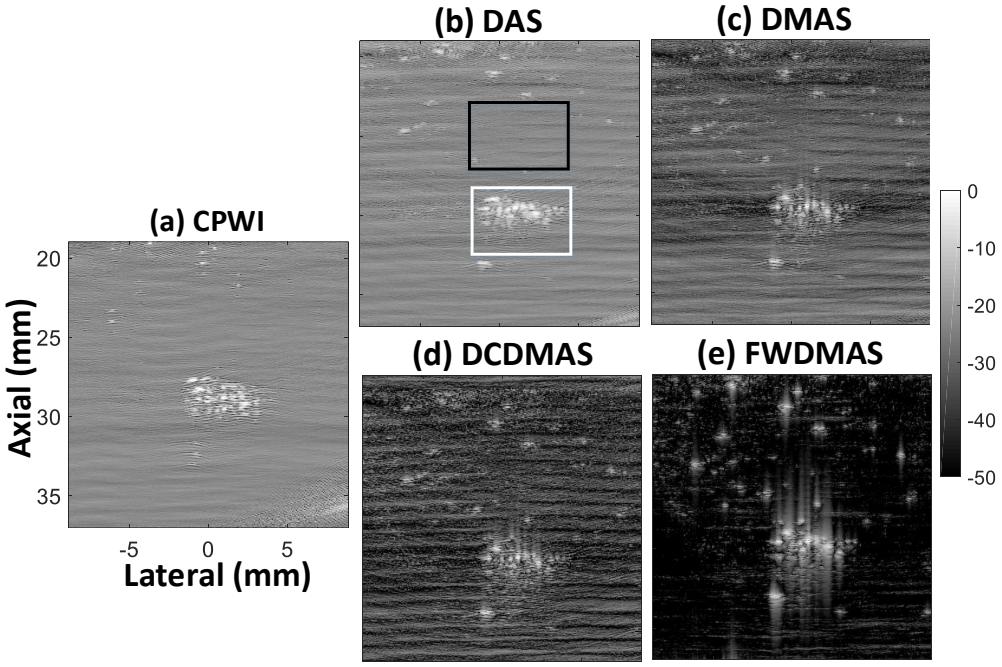

Figure 2.16: The interlaced B-mode images acquired after 5s of HIFU insonification. (a) CPWI by DAS with five steering angles. (b), (c), (d) and (e) are with single plane wave beamformed by DAS, DMAS, DCDMAS and FWDMAS, respectively. The white and black rectangles are for signal and noise ROI separately.

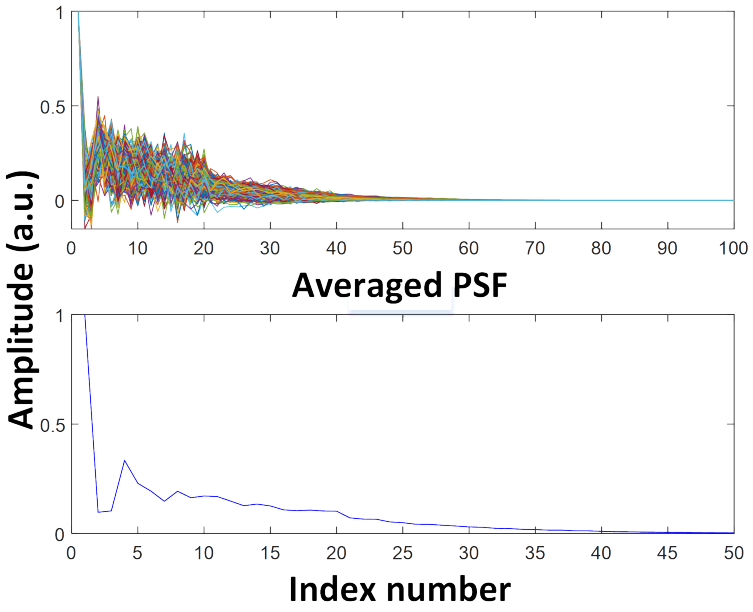

Figure 2.17: PSF pulse response function estimated from the interlaced B-mode beamformed by DMAS.

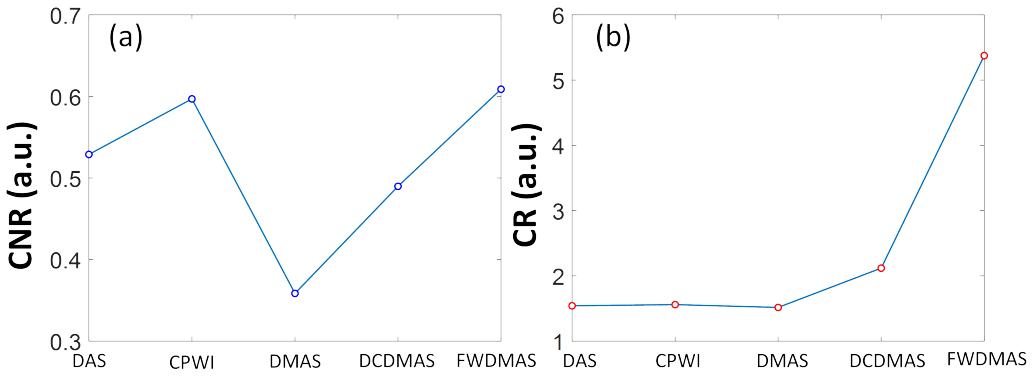

Figure 2.18: The (a) CNR and (b) CR curve of the interlaced B-mode beamformed by different imaging techniques.

2.4.3 Discussion

As shown in Figures 2.13 and 2.15, the image quality of DCDMAS heavily relies on the estimation of PSF pulse response function, which cannot provide a stable performance, as the Cepstrum-based PSF estimation only works well when the image character is non-uniform with high CNR and CR. Therefore, this part mainly concentrates on the explanations between DMAS and the proposed method, FWD-MAS.

Image contrast

As stated in section 2.4.2.A, the peak side lobe is the main factor to determine the image contrast. The amplitude apodization technique Fenster and Lacefield (2015) is an important tool for the side lobe suppression. The intrinsic amplitude apodization function arises in each beamforming algorithm that highlights their ability for image contrast improvement Cohen and Eldar (2018). To illustrate the definition of intrinsic amplitude apodization, the assumption was made that a linear array R with N observations and each observation in one snapshot is uniform (i.e. 1) if $N_{th} \subseteq R$ otherwise is zero. For data $\bar{y}_i(t_i(x,z)$ in equation 2.6 could be re-expressed as:

$$\bar{y}_i(t_i(x,z)) = |\bar{y}_i(t_i(x,z))| * exp\{j\underline{/\bar{y}_i(t_i(x,z))}\}, \tag{2.24}$$

Where the $|\bar{y}_i(t_i(x,z))|$ and $\underline{/\bar{y}_i(t_i(x,z))}$ indicate the amplitude modulus and phase information of $\bar{y}_i(t_i(x,z)$, respectively.

Transforming the equation 2.24 into frequency domain:

$$\bar{y}_i(w) = |\bar{y}_i(w)| * exp\{-jwt_i(w)\}, \tag{2.25}$$

Then the equation 2.7 in time domain can be re-expressed in frequency domain as (i.e. the convolution relationship in time domain is identical to multiply relationship in frequency domain):

$$I(w) = \frac{2}{N^2 - N} \sum_{i=1}^{N-1} \sum_{j=i+1}^{N} |\bar{y}_i(w)||\bar{y}_j(w)| exp\{-jwt_i(w)\} exp\{-jwt_j(w)\}. \tag{2.26}$$

The equation 2.26 can be illustrated in a simpler version:

$$I(w) = \frac{2}{N^2 - N} \sum_{i=1}^{(N^2-N)/2} A_i * exp\{-jw\tau_i\}. \tag{2.27}$$

Where $A_i = |\bar{y}_i(w)||\bar{y}_j(w)|$ is an integer vector with length of $2N-1$, which is termed as the intrinsic amplitude apodization function, and τ_i is identical to $t_i(w)+t_j(w)$. Note that the DMAS related beamformers in this research were computed with the format in equations 2.8 and 2.15 due to their computation efficiency. The equation 2.7 was adopted here only for the explanation of the definition of the intrinsic amplitude apodization function. The definition of the intrinsic amplitude apodization function can also be applied to the DAS beamformer as a uniformed constant number over the aperture data. Figure 2.19 illustrates that the intrinsic amplitude apodization function of DAS gives a uniformed constant number over the aperture channels. For DMAS, its intrinsic amplitude apodization function shows with the triangle shape to reduce the unwanted side lobes, while the intrinsic amplitude apodization function of FWDMAS displays in a quasi-Hanning shape. This explains the phenomenon for image contrast improvement in which FWDMAS is better than DMAS, as shown in Figures 2.11, 2.14 and 2.16.

Spatial resolution

The spatial resolution of B-mode is governed by the centre frequency and available aperture size Ng and Swanevelder (2011). As the centre frequency of transmission for all beamforming is the same, the available aperture size becomes the sole main factor to determine the resolution. In Figure 2.11, the DMAS based methods can be considered as to beamform the RF data from an artificial array with $2N-1$ aperture sizes, as compared with DAS with N aperture sizes, while the intrinsic amplitude apodization function of DMAS keeps the same degree of freedom (nonzero amplitude values shown in Figure 2.19) as FWDMAS, which indicates, theoretically, the resolution of DMAS and FWDMAS would be the same and nearly two times of DAS. However, in Figure 2.12, the FWDMAS displays a slightly lateral resolution improvement compared with DMAS, which could benefit from the contribution of spectrum equalisation technique. Figure 2.20 is the schematic process to equalise the input spectrum (a). The aim of spectral equalisation is a process to boost the balance of spectral components, as shown by the dashed line in (b), and ultimately to achieve finer resolution. Whilst this spectral could in theory be attained, in practise it tends to amplify the energy locating at low and high frequency components, which could be noisy and therefore increase the ambient noise [i.e. this noisy phenomenon can be observed in Figure 2.9(a, b, c)]. This problem raises some inherent fuzziness related to the bandwidth of the signal, so that it would be more ideal to equalise the data within the interested

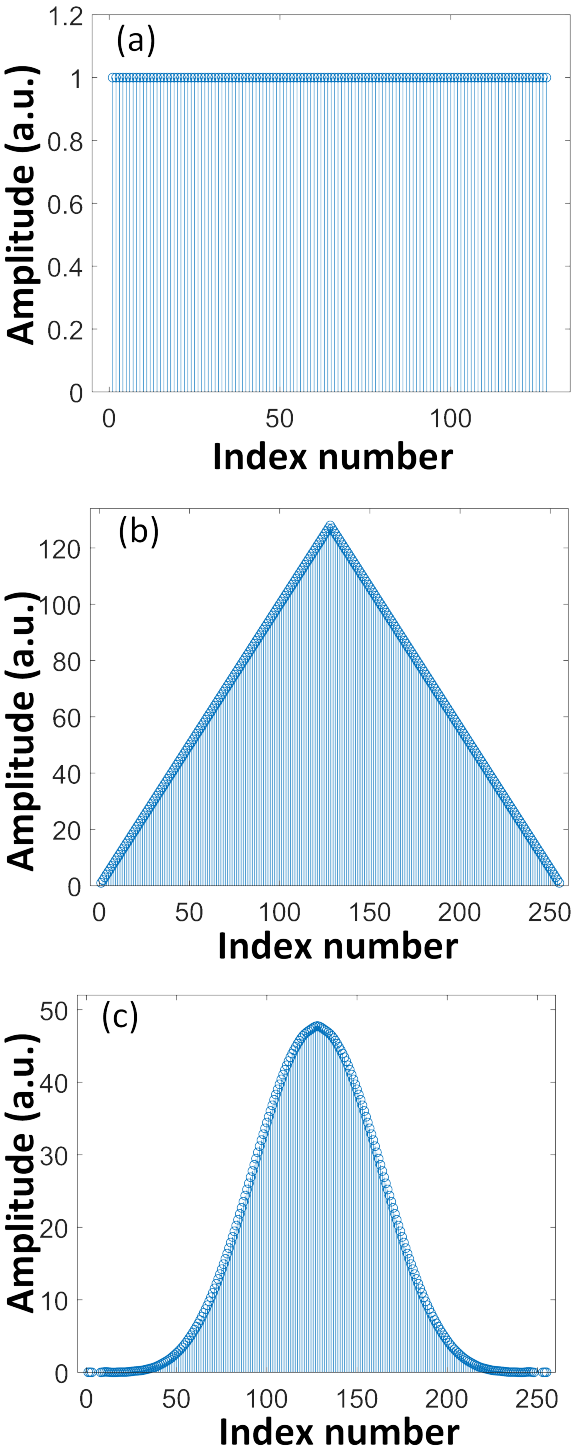

Figure 2.19: The amplitude apodization functions arise from (a) DAS, (b) DMAS and (c) FWDMAS.

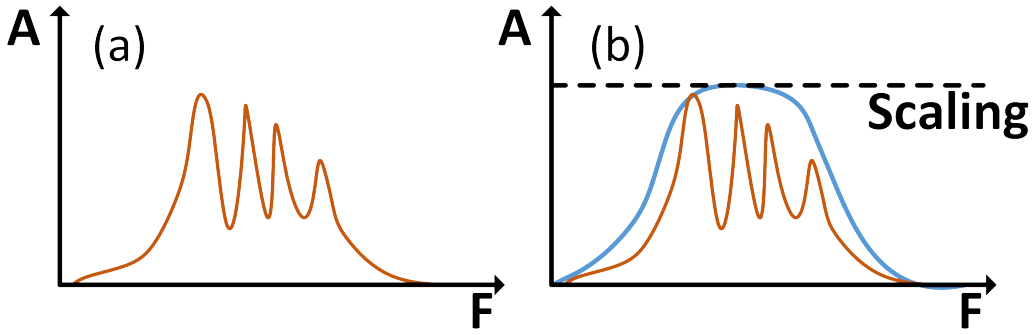

Figure 2.20: The schematic process for spectral equalisation of the re-aligned RF data: (a) the input frequency spectrum (frequency transformation of the spatial realigned RF data for each beamformed pixel), (b) the frequency spectrum being equalised. The dashed line represents the spectrum being equalised by TWDMAS. The blue curve represents the spectrum being equalised by FWDMAS.

bandwidth without overly boosting unwanted energy components by whitening in frequency domain, as shown schematically by the blue curve (b) [i.e. Figure 2.9(d) relative to Figure 2.9(a, b, c) with better ambient noise mitigation, conceding the above explanation].

Energy preservation

The subsequent concern raised in the spectral equalisation technique is energy preservation. Mathematically, based on Parseval's theorem, the output energy in time and frequency domain could be illustrated as:

$$E(t) = \int_{t_1}^{t_2} |\bar{y}(t)|^2 dt. \tag{2.28}$$

$$E(w) = \int_{w_1}^{w_2} |\bar{y}(w)|^2 dw. \tag{2.29}$$

To stabilise the frequency spectrum, a scaling level (shown in Figure 2.20) will generally be set [i.e. in current research is $\bar{y}(w) = scaling = 1$ Dr. Erol Kalkan (2022)]. However, this may result in energy misinterpretation of beamforming output during the frequency whitening transformation process (i.e. equation 2.28 $\neq$ equation 2.29). An accurate energy preservation deserves further consideration, as to build a good quantitative relationship between the hypergenicity in the B-mode and the intensity of significant boiling bubbles, which is important to reveal

the cavitation-related meanings for HIFU treatment monitoring. The adaptive scaling functions McWhorter et al. (1996) that could be applied to prevent energy loss are beyond the scope of this research and are, therefore, not emphasised here.

Computation complexity

Another concern for different beamformers is the computation cost Ikramov and Savel'Eva (2000); Van Loan and Golub (1996). According to equation 2.8, the computation complexity of DMAS has been reduced from $O(N^2)$ to $O(N)$, which is identical to DAS. For DCDMAS, the estimation of PSF and deconvolution by Wiener filter is performed after beamforming, so that its magnitude of computation complexity keeps the same level as DMAS ($O(N)$). Due to the calculation and decomposition of the covariance matrix, the computation complexity for ZCADMAS could approximately reach $O(N^3)$. The computation complexity of ChoDMAS is varied based on the input data-matrix. When performing the inversion of triangular covariance matrix $\mathbf{L}^{-1}$ in equation 2.12 with ones on the diagonal, its computation complexity could be $O(N^3 - N^2)$; otherwise (i.e., without ones on the diagonal), it should be $O(N^3 + N)$, almost same magnitude of ZCADMAS with $O(N^3)$. The VarDMAS is as efficient as DAS ($O(N)$), as no need for the calculation of covariance matrix $\mathbf{R}$. The FWDMAS is flattening the frequency components of realigned data in the interested bandwidth without a time-consuming computation process that determines its complexity is $O(N)$. As the next step, further considerations using parallel computing platforms (i.e. high performance GPU servers) could significantly improve the computation speed.

2.5 Conclusions

The contributions made in this chapter are many including the CDWI was selected as an optimal interlaced modality via phased array to consider its frame rate, image quality, and field of view. For HIFU treatment, the relationship between duty cycles and lesion size with different PNPs was investigated using gel phantoms, and the results show that a 95% duty cycle could be an optimal choice to compromise B-mode data acquisition time and thermal ablation performance. Finally, a cross-correlated beamformer in the whitened domain was investigated and applied to the interlaced B-mode. In both simulations and experiments, the superiority of FWDMAS over DMAS could be summarised in two aspects. Firstly, the robustness of anti-noise is demonstrated by the image contrast improvement, which provides the possibility to minimise the time gap (i.e. setting to prevent the HIFU interference). Secondly, the resolution improvement could reduce the steered number used for compounding and therefore result in a shorter B-mode data acquisition time. Either of the above superiority could cut down the HIFU-dead time and maximise the duty cycle, ultimately magnifying the HIFU treatment performance. Also, the proposed beamforming technique can be potentially developed into varied modalities (linear or divergent mode) to fit into different imaging transducers. All these give the potential to inspire an efficient ultrasound HIFU monitoring regimen for clinical use.

2.6 Appendix

Figure 2.21 illustrates the mitigation of the axial artefacts by filtered-delay-multiply-and-sum (FDMAS) Matrone et al. (2016); Prieur et al. (2018). The bandpass filter was not adopted in this research aiming to emphasise the contribution only from whitening techniques (i.e. spectral equalisation) on the cross-correlated beamforming algorithms.

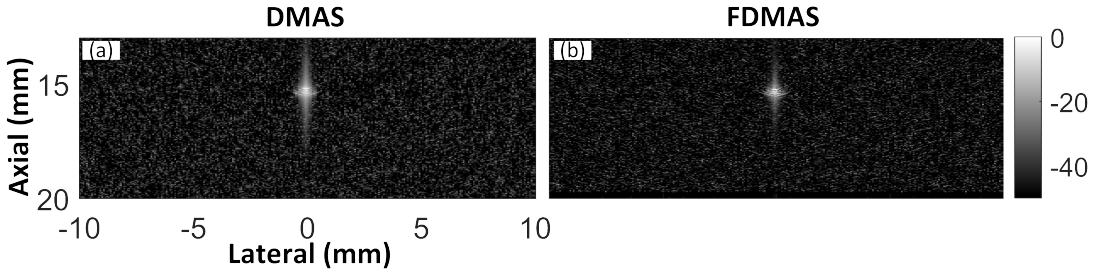

Figure 2.21: The simulated PSF by (a) DMAS and (b) filtered DMAS (FDMAS). Noise was added to the RF data, resulting in a signal-to-noise ratio of -20 dB.

Chapter References

Anand A. and Kaczkowski P.J. (2004). Monitoring formation of high intensity focused ultrasound (hifu) induced lesions using backscattered ultrasound. *Acoustics Research Letters Online*, **5**(3), pp. 88–94.

Chen W.S., Brayman A.A., Matula T.J. and Crum L.A. (2003). Inertial cavitation dose and hemolysis produced in vitro with or without optison®. *Ultrasound in medicine & biology*, **29**(5), pp. 725–737.

Cohen R. and Eldar Y.C. (2018). Sparse convolutional beamforming for ultrasound imaging. *IEEE transactions on ultrasonics, ferroelectrics, and frequency control*, **65**(12), pp. 2390–2406.

Coleman A., Choi M. and Saunders J. (1996). Detection of acoustic emission from cavitation in tissue during clinical extracorporeal lithotripsy. *Ultrasound in medicine & biology*, **22**(8), pp. 1079–1087.

Coussios .C., Farny C., Ter Haar G. and Roy R. (2007). Role of acoustic cavitation in the delivery and monitoring of cancer treatment by high-intensity focused ultrasound (hifu). *International journal of hyperthermia*, **23**(2), pp. 105–120.

Cowell D.M., Smith P.R. and Freear S. (2013). Phase-inversion-based selective harmonic elimination (pi-she) in multi-level switched-mode tone-and frequency-modulated excitation. *IEEE transactions on ultrasonics, ferroelectrics, and frequency control*, **60**(6), pp. 1084–1097.

CRIS2 (2022). Cirs1. https://www.cirsinc.com/products/ultrasound/zerdine-hydrogel/multi-purpose-multi-tisse-ultrasound-phantom/.

Dr. Erol Kalkan P. (2022). Spectral whitening. https://www.mathworks.com/matlabcentral/fileexchange/65345-spectral-whitening.

Ebbini E.S., Bischof J.C., Visaria R.K. and Shrestha A. (2007). Quadratic b-mode and pulse inversion imaging of thermally-induced lesions in vivo. In: *2007 4th IEEE International Symposium on Biomedical Imaging: From Nano to Macro*. IEEE, pp. 1120–1123.

Eldar Y.C. and Oppenheim A.V. (2003). Mmse whitening and subspace whitening. *IEEE Transactions on Information Theory*, **49**(7), pp. 1846–1851.

Escudero D.S., Goudot G., Vion M., Tanter M. and Pernot M. (2018). 2d and 3d real-time passive cavitation imaging of pulsed cavitation ultrasound therapy in moving tissues. *Physics in Medicine & Biology*, **63**(23), p. 235028.

Fenster A. and Lacefield J.C. (2015). *Ultrasound imaging and therapy*. Taylor & Francis.

Gateau J., Aubry J.F., Pernot M., Fink M. and Tanter M. (2011). Combined passive detection and ultrafast active imaging of cavitation events induced by short pulses of high-intensity ultrasound. *IEEE transactions on ultrasonics, ferroelectrics, and frequency control*, **58**(3), pp. 517–532.

Helmore S. (2009). Dealing with the noise-improving seismic whitening and seismic inversion workflows using frequency split structurally oriented filters. In: *2009 SEG Annual Meeting*. OnePetro.

Holfort I.K., Gran F. and Jensen J.A. (2009). Broadband minimum variance beamforming for ultrasound imaging. *IEEE transactions on ultrasonics, ferroelectrics, and frequency control*, **56**(2), pp. 314–325.

Hölscher T., Raman R., Fisher D.J., Ahadi G., Zadicario E. and Voie A. (2013). Effects of varying duty cycle and pulse width on high-intensity focused ultrasound (hifu)-induced transcranial thrombolysis. *Journal of Therapeutic Ultrasound*, **1**(1), pp. 1–5.

Hu Z., Yang X.Y., Liu Y., Sankin G.N., Pua E.C., Morse M.A., Lyerly H.K., Clay T.M. and Zhong P. (2007). Investigation of hifu-induced anti-tumor immunity in a murine tumor model. *Journal of translational medicine*, **5**(1), pp. 1–11.

Hynynen K. (1991). The threshold for thermally significant cavitation in dog's thigh muscle in vivo. *Ultrasound in medicine & biology*, **17**(2), pp. 157–169.

Ikeda H., Nagaoka R., Lafond M., Yoshizawa S., Iwasaki R., Maeda M., Umemura S.i. and Saijo Y. (2018). Singular value decomposition of received ultrasound signal to separate tissue, blood flow, and cavitation signals. *Japanese Journal of Applied Physics*, **57**(7S1), p. 07LF04.

Ikeda H., Yoshizawa S., Maeda M., Umemura S.i. and Saijo Y. (2019). Blood flow imaging using singular value decomposition filter during high-intensity focused ultrasound exposure. *Japanese Journal of Applied Physics*, **58**(SG), p. SGGE15.

Ikramov K.D. and Savel'Eva N. (2000). Conditionally definite matrices. *Journal of Mathematical Sciences*, **98**(1), pp. 1–50.

Jensen J.A. and Leeman S. (1994). Nonparametric estimation of ultrasound pulses. *IEEE Transactions on biomedical engineering*, **41**(10), pp. 929–936.

Jensen J.A., Nikolov S.I., Gammelmark K.L. and Pedersen M.H. (2006). Synthetic aperture ultrasound imaging. *Ultrasonics*, **44**, pp. e5–e15.

Kessy A., Lewin A. and Strimmer K. (2018). Optimal whitening and decorrelation. *The American Statistician*, **72**(4), pp. 309–314.

Khokhlova V.A., Bailey M.R., Reed J.A., Cunitz B.W., Kaczkowski P.J. and Crum L.A. (2006). Effects of nonlinear propagation, cavitation, and boiling in lesion formation by high intensity focused ultrasound in a gel phantom. *The Journal of the Acoustical Society of America*, **119**(3), pp. 1834–1848.

Klemm M., Craddock I., Leendertz J., Preece A. and Benjamin R. (2008). Improved delay-and-sum beamforming algorithm for breast cancer detection. *International Journal of Antennas and Propagation*, **2008**.

Krzywosz N. (2015). *Investigation of ambient seismic noise using seismic interferometry in western Montana*. Ph.D. thesis, Montana Tech of The University of Montana.

Malcolm A. and Ter Haar G. (1996). Ablation of tissue volumes using high intensity focused ultrasound. *Ultrasound in medicine & biology*, **22**(5), pp. 659–669.

Matrone G., Ramalli A., Savoia A.S., Tortoli P. and Magenes G. (2016). High frame-rate, high resolution ultrasound imaging with multi-line transmission and filtered-delay multiply and sum beamforming. *IEEE transactions on medical imaging*, **36**(2), pp. 478–486.

Matrone G., Savoia A.S., Caliano G. and Magenes G. (2014). The delay multiply and sum beamforming algorithm in ultrasound b-mode medical imaging. *IEEE transactions on medical imaging*, **34**(4), pp. 940–949.

McLaughlan J., Cowell D. and Freear S. (2017). Gold nanoparticle nucleated cavitation for enhanced high intensity focused ultrasound therapy. *Physics in Medicine & Biology*, **63**(1), p. 015004.

McLaughlan J., Rivens I., Leighton T. and Ter Haar G. (2010). A study of bubble activity generated in ex vivo tissue by high intensity focused ultrasound. *Ultrasound in medicine & biology*, **36**(8), pp. 1327–1344.

McLaughlan J.R. (2018). Controllable nucleation of cavitation from plasmonic gold nanoparticles for enhancing high intensity focused ultrasound applications. *JoVE (Journal of Visualized Experiments)*, (140), p. e58045.

McWhorter L., Scharf L. and Griffiths L. (1996). Adaptive coherence estimation for radar signal processing. In: *Conference Record of The Thirtieth Asilomar Conference on Signals, Systems and Computers*, vol. 1. IEEE, pp. 536–540.

Meaney P.M., Cahill M.D. and ter Haar G.R. (2000). The intensity dependence of lesion position shift during focused ultrasound surgery. *Ultrasound in medicine & biology*, **26**(3), pp. 441–450.

Moubark A.M., Alomari Z., Harput S., Cowell D.M. and Freear S. (2016). Enhancement of contrast and resolution of b-mode plane wave imaging (pwi) with non-linear filtered delay multiply and sum (fdmas) beamforming. In: *2016 IEEE International Ultrasonics Symposium (IUS)*. IEEE, pp. 1–4.

Mozaffarzadeh M., Sadeghi M., Mahloojifar A. and Orooji M. (2018). Double-stage delay multiply and sum beamforming algorithm applied to ultrasound medical imaging. *Ultrasound in medicine & biology*, **44**(3), pp. 677–686.

Ng A. and Swanevelder J. (2011). Resolution in ultrasound imaging. *Continuing Education in Anaesthesia Critical Care & Pain*, **11**(5), pp. 186–192.

Papadacci C., Pernot M., Couade M., Fink M. and Tanter M. (2014). High-contrast ultrafast imaging of the heart. *IEEE transactions on ultrasonics, ferroelectrics, and frequency control*, **61**(2), pp. 288–301.

Prieur F., Rindal O.M.H. and Austeng A. (2018). Signal coherence and image amplitude with the filtered delay multiply and sum beamformer. *IEEE transactions on ultrasonics, ferroelectrics, and frequency control*, **65**(7), pp. 1133–1140.

Rabkin B.A., Zderic V. and Vaezy S. (2005). Hyperecho in ultrasound images of hifu therapy: involvement of cavitation. *Ultrasound in medicine & biology*, **31**(7), pp. 947–956.

Salgaonkar V.A., Datta S., Holland C.K. and Mast T.D. (2009). Passive cavitation imaging with ultrasound arrays. *The Journal of the Acoustical Society of America*, **126**(6), pp. 3071–3083.

Shen C.C. and Hsieh P.Y. (2019). Ultrasound baseband delay-multiply-and-sum (bb-dmas) nonlinear beamforming. *Ultrasonics*, **96**, pp. 165–174.

Silverman R.H., Muratore R., Ketterling J.A., Mamou J., Coleman D.J. and Feleppa E.J. (2006). Improved visualization of high-intensity focused ultrasound lesions. *Ultrasound in medicine & biology*, **32**(11), pp. 1743–1751.

Smith P.R., Cowell D.M. and Freear S. (2013). Width-modulated square-wave pulses for ultrasound applications. *IEEE transactions on ultrasonics, ferroelectrics, and frequency control*, **60**(11), pp. 2244–2256.

Smith P.R., Cowell D.M., Raiton B., Ky C.V. and Freear S. (2012). Ultrasound array transmitter architecture with high timing resolution using embedded phase-locked loops. *IEEE transactions on ultrasonics, ferroelectrics, and frequency control*, **59**(1), pp. 40–49.

Synnevag J.F., Austeng A. and Holm S. (2009). Benefits of minimum-variance beamforming in medical ultrasound imaging. *IEEE transactions on ultrasonics, ferroelectrics, and frequency control*, **56**(9), pp. 1868–1879.

Taxt T. (1997). Comparison of cepstrum-based methods for radial blind deconvolution of ultrasound images. *IEEE transactions on ultrasonics, ferroelectrics, and frequency control*, **44**(3), pp. 666–674.

Ter Haar G. (2016). Hifu tissue ablation: concept and devices. *Therapeutic Ultrasound*, pp. 3–20.

Uhlendorf V., Scholle F.D. and Reinhardt M. (2000). Acoustic behaviour of current ultrasound contrast agents. *Ultrasonics*, **38**(1-8), pp. 81–86.

Van Loan C.F. and Golub G. (1996). Matrix computations (johns hopkins studies in mathematical sciences).

Watkin N., Ter Haar G. and Rivens I. (1996). The intensity dependence of the site of maximal energy deposition in focused ultrasound surgery. *Ultrasound in medicine & biology*, **22**(4), pp. 483–491.

Xie J., Yuan Y. and Liu Y. (1998). Super-resolution processing for hf surface wave radar based on pre-whitened music. *IEEE journal of oceanic engineering*, **23**(4), pp. 313–321.

Yu C., Zhang C. and Xie L. (2012). A blind deconvolution approach to ultrasound imaging. *IEEE transactions on ultrasonics, ferroelectrics, and frequency control*, **59**(2), pp. 271–280.

Zhang M., Varray F., Besson A., Carrillo R.E., Viallon M., Garcia D., Thiran J.P., Friboulet D., Liebgott H. and Bernard O. (2016). Extension of fourier-based techniques for ultrafast imaging in ultrasound with diverging waves. *IEEE transactions on ultrasonics, ferroelectrics, and frequency control*, **63**(12), pp. 2125–2137.

Chapter 3

Evaluation of PAM beamformers for high-duty-cycle HIFU applications

High-duty-cycle high-intensity focused ultrasound (HIFU) exposures have been employed for clinical thermal ultrasound therapy. Passive acoustic mapping (PAM), with its unique receiving characteristics, has been paralleled with the therapeutic HIFU process to monitor possible cavitation activities. In this research, the relative-time-delay PAM beamformers was explored for long exposure HIFU monitoring (e.g., a quasi-Continuous Wave (qCW) with 95 % duty cycle, 5 s duration was utilized), and the reduction of the DC components generated during such beamforming process which was incorporated with a Robust Capon Beamformer (RCB) to give Robust Capon beamformer with DC reduction (RCB-DC) for the rejection of residual cavitation energy spread. The time exposure acoustics (TEA), RCB, Eigensubspace RCB (E-RCB), and Wiener E-RCB (WE-RCB), were analysed with RCB-DC in both tissue-mimicking gel phantoms and *ex vivo* bovine liver tissue via the aforementioned qCW exposure. The final results demonstrate 86 % to 94 % noise-area suppression when RCB-DC is compared with TEA, while the computation time of RCB, E-RCB, and WE-RCB is maintained at the same magnitude.

3.1 Introduction

High-intensity focused ultrasound is a non/minimally-invasive technique that is used in the treatment of soft tissue diseases, such as those in the prostate, breast and liver Blana et al. (2004); Chan et al. (2002); Kennedy et al. (2004); Wu et al. (2003). During HIFU exposures, both the thermal and mechanical mechanisms result in ultrasound therapy Bailey et al. (2003). The generation of thermal damage, or 'thermal lesions', causes coagulation necrosis, which is the primary mechanism of tissue damage in the clinical application of HIFU Nyborg and Ziskin (1985); Ter Haar (1995). Consequently, cavitation activity from acoustically and/or thermally nucleated bubbles can play an important role in mechanical mechanisms dominant HIFU treatments, but as this activity can be either beneficial or detrimental Shaw et al. (2016). Cavitation monitoring becomes important for the safety, efficiency and development of HIFU therapy techniques.

Magnetic resonance imaging (MRI) and/or ultrasound imaging are generally used to guide and monitor the clinical use of HIFU Ebbini and Ter Haar (2015). The current gold-standard is MRI, as it can be used to estimate the *in situ* temperature change during exposures Köhler et al. (2009). However, this approach limits the use of HIFU to dedicated facilities and increases the cost and complexity of such treatment Al-Bataineh et al. (2012). When compared with MRI, diagnostic ultrasound guidance is more accessible but provides poor differentiation between normal and ablated tissue. The ultrasound-guided approach mainly relies on the presence of hyperechogenicity from bubbles, most likely formed due to tissue boiling McLaughlan et al. (2010); however, their presence represents over-treatment of the region. Additionally, the presence of boiling bubbles can disrupt the HIFU field, reducing treatment efficacy Shaw et al. (2016). Strong acoustic interference from the HIFU field is scattered by tissue, which indicates that B-mode imaging generally has to be interleaved with the HIFU insonation, and hence, preventing active monitoring of bubble activity throughout the HIFU exposure Rabkin et al. (2005).

Passive cavitation detection (PCD) is used to detect characteristic acoustic emissions from bubble activity during HIFU exposures Coussios et al. (2007); Johansen et al. (2018); McLaughlan et al. (2010). A range of methods exist for performing PCD, using both single-element and array detectors that are co-aligned or that intersect with a portion of the HIFU focal region. Single-element PCD systems have been employed to non-invasively ensure a safe level of HIFU expo-

sure Arvanitis and McDannold (2013); Bull et al. (2013); Coussios et al. (2007); Li et al. (2014); however, in this scenario, such data gives no much more indication of the spatial distribution of suspected cavitation events, even its data processing is straightforward and can be done in real time. When performing PCD with a multi-element array Farny et al. (2009), it is possible to implement a dedicated beamformer to map the source location. This technique is commonly referred to as passive acoustic mapping (PAM) or passive cavitation imaging Gyöngy and Coussios (2009); Salgaonkar et al. (2009). This approach can yield spatial information about cavitation activity and has been applied in conventional and customised ultrasound systems Haworth et al. (2016b); Jensen et al. (2012); Salgaonkar et al. (2009). Gyöngy *et al.* demonstrated the feasibility of using PAM for cavitation monitoring during HIFU ablation Gyongy et al. (2008); Gyöngy and Coussios (2009). Currently, PAM is widely used in monitoring HIFU therapy Arvanitis et al. (2013); Haworth et al. (2016a,b, 2015); Jensen et al. (2012); O'Reilly et al. (2014), exploring cavitation dynamics Choi and Coussios (2012); Crake et al. (2015); Haworth et al. (2012, 2014); Lyka et al. (2016) and studying ultrasound-mediated bio-effects for drug delivery Choi et al. (2014); Kwan et al. (2015).

To identify the spatial location of cavitation activity, a range of different passive beamforming techniques have been developed in both the frequency and time domains Abadi et al. (2018); Coviello et al. (2015); Gyöngy and Coussios (2009); Haworth et al. (2016a, 2014). These techniques can be categorised into two groups based on the time-delay pattern used. First, some techniques use absolute time delay, such as the work on monitoring a cavitation-induced blood–brain barrier opening using short (microsecond) pulses Burgess et al. (2018). In this method, the beamforming algorithm is kind like the pulse–echo beamformer, as the cavitation dynamics between individual events are temporally distant enough that averaging would lead to monitoring degradation. Other techniques use relative time delay, developing from TEA Gyongy et al. (2008); Gyöngy and Coussios (2009), and can be employed for continuous-wave (CW) ultrasound therapy monitoring. Experimental results have demonstrated that the resolution of relative-time-delay PAM is determined by the diffraction pattern of the imaging array and is independent of the cavitation emission duration Abadi et al. (2018). In this study, a relative-time-delay PAM beamformer implementing on an uncalibrated imaging array was analysed to establish its efficiency for qCW HIFU monitoring.

A study on underground acoustic source imaging Norton et al. (2006); Norton and Won (2000) demonstrated that constant background noise (termed 'DC

component') contributes to each intensity-based image/bin. After averaging every intensity-based image into a single frame in a pixel-wise fashion, the DC component was shown to form a significant part of the uncorrelated energy accumulation. This demonstrates a need to reduce the DC component for CW exposures, as averaging is a required process in relative-time-delay beamformer algorithms. Adaptive techniques based on Capon beamforming (CB) and RCB Coviello et al. (2015); Li et al. (2003); Stoica et al. (2002) have been developed, and RCB-based beamformers, in particular, have been shown with excellent anti-noise capability. This improvement has been achieved mainly by accounting for array mismatch in receiver locations due to an uncalibrated array and inhomogeneity of tissue. However, none of the these time domain techniques have considered the impact of DC components, which in CW or qCW monitoring conditions will degrade the beamforming performance.

Other computation techniques that do not explicitly take into account DC components have been combined with RCB-based PAM, such as eigen-decomposition Lu et al. (2018); Polichetti et al. (2020), E-RCB, to improve the lateral and axial full width at half maximum (FWHM) by approximately 40 % and 30 % when compared with TEA, but the extra decomposition of the covariance matrix increases the computation time. The coherence factor (CF) is defined as the ratio of the coherent sum to the incoherent sum across the elements of the array Nilsen and Holm (2010). Methods based on the CF, such as the phase coherence factor, have also been used in PAM beamformers to suppress side lobes Boulos et al. (2018). However, with the signal-to-noise ratio (SNR) decreases due to depth-dependent attenuation, the CF-based method may also eliminate signals of interest, reducing the accuracy of the representation of the cavitation region Nilsen and Holm (2010). In this study, a specific type of CF post-filter, the Wiener post-filter, was incorporated with E-RCB-based PAM (in WE-RCB) to attempt further noise suppression. The Wiener post-filter method has already been applied to the eigensubspace capon beamformer (E-CB) in B-mode imaging to demonstrate its efficiency Nilsen and Holm (2010); Zeng et al. (2012) showed that when compared with the E-CB B-mode beamformer, the Wiener post-filter improved the contrast ratio by 32.9 % in a cyst phantom.

For the proposed method (RCB-DC), we concentrate on three aspects, as follows: a time-efficiency spatial cross-correlation operation was involved in the passive beamforming process, reducing the coherent computation complexity per intensity-based bin from N^2 to N (N is the element number of the imaging array),

and the RCB apodisation file was incorporated into the proposed beamformer, due to its capability to suppress energy spread and adaptively compensate for imperfections (such as steering mismatch) of the uncalibrated imaging array; as under CW or qCW monitoring conditions, the DC components could be accumulated into significance, mitigation was attempted. All ultrasound monitoring experiments (interleaved coherent plane-wave imaging [CPWI] and PAM) and the triggering of HIFU ablation were performed using the Ultrasound Array Research Platform (UARP) Cowell et al. (2016); Harput et al. (2013).

The aim of this study is to illustrate the performance of PAM beamformers (TEA, CB, RCB, E-RCB, WE-RCB and RCB-DC) in high-duty-cycle HIFU exposures (rather than to definitively rank the models) via an uncalibrated imaging array and then analyse the DC problem under such experimental conditions. The algorithms were tested on data acquired from qCW HIFU exposures (peak negative pressures of 3 MPa to 7 MPa ± 14 %, equivalent free-field averaged spatial peak intensity of 2100 W cm^{-2} to 3800 W cm^{-2} ± 6 %) in both *in vitro* gel phantoms and *ex vivo* bovine liver tissue. The relative performance of these algorithms was illustrated using relevant imaging metrics, including computation time, spatial resolution, lateral and axial contrast ratios, and the size of the point spread function (PSF) A_{50} Abadi et al. (2018). The combined effect of DC reduction and robust weighting vectors on tail artefact mitigation was also investigated.

3.2 Methods

3.2.1 Passive acoustic mapping algorithms

To form an image, the output acoustic power of PAM, $I_{PAM}(x, z)$, from a point (x, z) is calculated, where x is the lateral axis and z is the depth axis of a diagnostic probe with $N = 128$ elements (Figure 3.1). The relative time of flight between the pixel (x_0, z_0) and the element located at $(x_n, 0)$ is expressed as:

$$d(x_0, z_0, t_p) = t_p + \frac{\sqrt{(x_0 - x_n)^2 + z_0^2}}{c}, \tag{3.1}$$

where $\sqrt{(x_0 - x_n)^2 + z_0^2}$ is the distance from pixel (x_0, z_0) to the element located at $(x_n, 0)$, t_p is the integration time variable, which is a function of the sampling frequency (i.e. discretised by the sampling frequency), and c is the speed of sound.

Acronyms	-	Justification
qCW	-	Quasi-continuous wave
CB	-	Capon beamformer
E-CB	-	Eigenspace Capon beamformer
RCB	-	Robust Capon beamformer
E-RCB	-	Eigenspace robust Capon beamformer
WE-RCB	-	Wiener eigenspace robust Capon beamformer
RCB-DC	-	Robust Capon beamformer with DC reduction

Table 3.1: Selected Beamformer Acronyms

Symbol	Value	Justification
f_s	40 MHz	The sampling rate
t_p	$1/f_s$	t_p is one instance (i.e. discretised by the sampling rate) to beamform each intensity-based image
T	40 μs	The integration time for each PAM frame
Image dimension	16*68	Axial pixels per beamformed line 16, lateral beamformed lines 68
Field of view (mm^2)	16*20.4	Axial step 1 mm, lateral step 0.3 mm (i.e. pitch size), pixel area 0.3 mm^2

Table 3.2: Selected Beamformer Parameter/Symbols

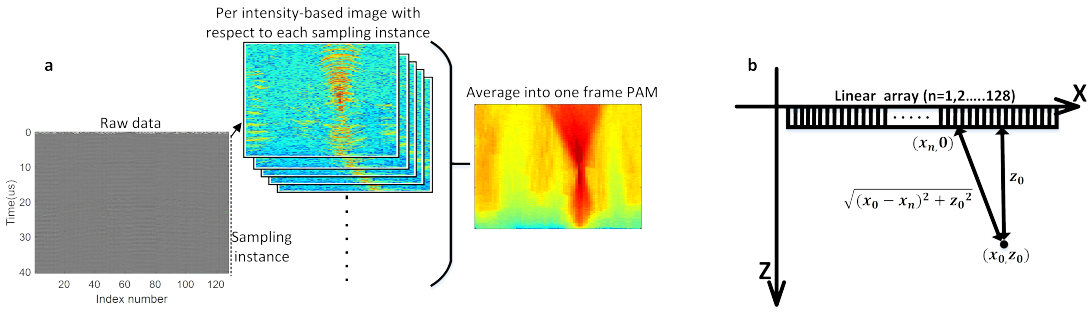

Figure 3.1: Schematic of a) per intensity-based image (or bin) being averaged into PAM process and b) imaging array and corresponding imaging plane for each intensity-based image beamforming.

The delayed signals $s_n(x_0, z_0, t_p)$ are expressed as:

$$s_n(x_0, z_0, t_p) = \\ 4\pi\sqrt{(x_0 - x_n)^2 + z_0^2} * p_n(d(x_0, z_0, t_p)), \tag{3.2}$$

The signal p_n is the time-delayed back-propagating raw data ($n = 1, 2, \ldots, 128$), and $4\pi\sqrt{(x_0 - x_n)^2 + z_0^2}$ is the receiving spatial compensation term for the spherical spreading of the scattered/emitted acoustic waves from the focal region. Source energy is calculated by integrating the square of source strength over the integration time interval T and apodising channel data by applying the weighting vector $\mathbf{w}$ for noise suppression, where the t_0 and T are reconstruction parameters based on the time interval of acoustic activity and the mapping spatial area. ρ is the density of the medium.

$$I_{\mathrm{PAM}}(x_0, z_0) = \\ \frac{1}{4\pi\,\rho\,c\,T\,N}\int_{t_0}^{t_0+T}\left[\sum_{n=1}^{N}\mathbf{w}\,s_n(x_0, z_0, t_p)\right]^2 dt_p\,. \tag{3.3}$$

Thus, the estimation of the PAM source is dependent on the calculation of $\mathbf{w}$. The non-adaptive PAM beamformer TEA uniformly weights the entire receiving signal, which can be expressed as Gyöngy and Coussios (2009); Lyka et al. (2018):

$$\mathbf{w}_{\mathrm{TEA}} = (1/N)\mathbf{1}, \tag{3.4}$$

Adaptive PAM beamformers, such as CB, calculate the weighting vectors by finding the optimal value from the linearly constrained quadratic optimisation problem but retain the disadvantage of steering vector uniformity. In contrast to

CB, RCB provides a simple way of eliminating the scaling ambiguity (the optimisation of the steering vectors) to account for tissue inhomogeneity and array non-calibration Coviello et al. (2015); Li et al. (2003); Stoica et al. (2002). The CB and RCB weight vectors can be written as:

$$\mathbf{w}_{\mathrm{CB}} = \frac{\boldsymbol{R}^{-1}\bar{\boldsymbol{\alpha}}}{\bar{\boldsymbol{\alpha}}^{*}\boldsymbol{R}^{-1}\bar{\boldsymbol{\alpha}}}, \tag{3.5}$$

$$\mathbf{w}_{\mathrm{RCB}} = \frac{\boldsymbol{R}^{-1}\check{\boldsymbol{\alpha}}}{\check{\boldsymbol{\alpha}}^{*}\boldsymbol{R}^{-1}\check{\boldsymbol{\alpha}}}, \tag{3.6}$$

where the covariance matrix $\boldsymbol{R}$ is defined as:

$$\boldsymbol{R}(x,z) = \int_{t_0}^{t_0+T} \mathbf{s}(x,z,t)\,\mathbf{s}(x,z,t)^{H}\,dt_p\,. \tag{3.7}$$

and $\mathbf{s}(x,z,t) = [s_1(x,z,t), s_2(x,z,t), \ldots, s_N(x,z,t)]$. $[.]^H$ is the conjugate transpose. In CB, $\bar{\boldsymbol{\alpha}} = [1,1,\ldots,1]$. For RCB, $\check{\boldsymbol{\alpha}} = \bar{\boldsymbol{\alpha}} - (I + \lambda\boldsymbol{R})^{-1}\bar{\boldsymbol{\alpha}}$ represents the actual steering vector, which is normalised as $\check{\boldsymbol{\alpha}} = (\check{\boldsymbol{\alpha}}N)/\|\check{\boldsymbol{\alpha}}\|$. The Lagrange multiplier λ can be calculated by Newton's methodology, which depends on $\epsilon = \|(I + \lambda\boldsymbol{R})^{-1}\bar{\boldsymbol{\alpha}}\|^2$, where ϵ decides the freedom of the steering vector to be varied within acoustic source region Coviello et al. (2015).

Eigenspace can be introduced into RCB-based PAM (in E-RCB) to further improve the image quality, but when compared with RCB, the inversion and decomposition of the covariance matrix increase the computation time Lu et al. (2018). The E-RCB weighting vector is calculated by projecting the RCB weighting vector into the signal subspace constructed by the eigenvectors related to $\alpha \in [0.1, 0.5]$-times larger eigenvalues of the covariance matrix Asl and Mahloojifar (2010). The E-RCB weighting vectors can be written as:

$$\mathbf{w}_{\mathrm{E-RCB}} = \boldsymbol{U}_s\,\boldsymbol{U}_s^{H}\,\mathbf{w}_{\mathrm{RCB}}, \tag{3.8}$$

The covariance matrix is decomposed into a signal subspace $\boldsymbol{R}_s$ and a noise subspace $\boldsymbol{R}_n$:

$$\begin{aligned} \boldsymbol{R}(x,z) &= \boldsymbol{U}\Lambda\boldsymbol{U}^{H} \\ &= \boldsymbol{U}_s\Lambda\boldsymbol{U}_s^{H} + \boldsymbol{U}_n\Lambda\boldsymbol{U}_n^{H} \\ &= \boldsymbol{R}_s + \boldsymbol{R}_n, \end{aligned} \tag{3.9}$$

where $\boldsymbol{U}_s = [\boldsymbol{V}_1, \boldsymbol{V}_2, ..., \boldsymbol{V}_{\mathrm{sig}}]$ and $\boldsymbol{U}_n = [\boldsymbol{V}_{\mathrm{sig}+1}, \boldsymbol{V}_{\mathrm{sig}+2}, ..., \boldsymbol{V}_L]$ represent the largest and the remaining smaller eigenvectors, respectively. All of these eigen-

vectors form the basis for $\boldsymbol{U}$. and $\boldsymbol{\Lambda} = \text{diag}[\lambda_1, \lambda_2, ..., \lambda_\text{L}]$ are the eigenvalues corresponding to $\boldsymbol{V}_i$ in descending order.

The Wiener beamformer can be considered an adaptive beamformer that is multiplied by a Wiener post-filter, which allows further optimisation of the weighting vectors. For the distortionless beamformers, the Wiener post-filter is determined by finding the minimum value of mean square error between the output and the true signal power Nilsen and Holm (2010); Zeng et al. (2012). The optimised Wiener filter can scale the output power such that it is closer to the true signal power than in E-CB Nilsen and Holm (2010). Here, the Wiener technique is introduced for the first time into PAM in combination with E-RCB and compared with the proposed RCB-DC method. The Wiener weighting vector (WE-RCB) can be expressed as Zeng et al. (2012):

$$\mathbf{w}_{\text{WE}-\text{RCB}} = \frac{\mathbf{w}_{\text{E}-\text{RCB}}{}^{H}\, \boldsymbol{R}_s\, \mathbf{w}_{\text{E}-\text{RCB}}}{\mathbf{w}_{\text{E}-\text{RCB}}{}^{H}\, \boldsymbol{R}\, \mathbf{w}_{\text{E}-\text{RCB}}} \mathbf{w}_{\text{E}-\text{RCB}}, \tag{3.10}$$

For this study, each PAM frame was the average of 781 successive intensity-based images over the acoustic activity integration period $T = 40\,\mu\text{s}$. The intensity-based image represents each individual 'square of amplitude' image beamformed with respect to each sampling instance t_p. An unbiased PAM image can be obtained by subtracting these DC components and apodising by the RCB weighting vector (RCB-DC):

$$\begin{aligned} I_{\text{RCB}-\text{DC}}(x_0, z_0) = \frac{1}{4\pi\, \rho\, c\, T\, N} \int_{t_0}^{t_0+T} \\ \left(\left[\sum_{n=1}^{N} \mathbf{w}_{\text{RCB}}\, s_n(x_0, z_0, t_p) \right]^2 \right. \\ \left. - \sum_{n=1}^{N} \left[\mathbf{w}_{\text{RCB}}\, s_n(x_0, z_0, t_p) \right]^2 \right) dt_p \,. \end{aligned} \tag{3.11}$$

In the proposed method, after considering DC reduction on every intensity-based image, the calculation of (3.11) is identical to a version of the lateral cross-correlation computation, with the incorporation of robust weighting vectors calculated by RCB to improve noise suppression. Within the integration calculation (3.11), the first term represents the passive image, and the second term aims to reduce DC components Norton et al. (2006).

3.2.2 Gel phantoms and *ex vivo* bovine liver tissue

Polyacrylamide tissue-mimicking gel phantoms containing bovine serum albumin (BSA) were used as temperature-sensitive phantoms for all relevant HIFU exposures in this study McLaughlan et al. (2017). These phantoms were fabricated by mixing filtered, degassed water (60 % v/v), acrylamide/bis-acrylamide solution (30 % v/v; A9926, Sigma Aldrich UK, Dorset, UK), 1 mol l^{-1} TRIS buffer (pH 8, 10 % v/v; T2694, Sigma Aldrich UK, Dorset, UK) and 10 % ammonium persulfate (APS; 0.86 % v/v). After BSA (7 % w/v; A7906, Sigma Aldrich UK, Dorset, UK) was added to the solution, it was placed in a vacuum chamber, degassed and mixed for approximately 60 min, with a vacuum of 80 mbar. Finally, the polymerisation catalyst TEMED (0.05 % v/v; T9281, Sigma Aldrich UK, Dorset, UK) was added, and the solution was immediately poured into moulds of size $95 \times 40 \times 32$ mm, then left at room temperature for 20 min to set McLaughlan (2018). For *ex vivo* bovine liver experiments, specimens were acquired and processed 2 h after slaughter. The tissue was processed into samples with an approximate size of $93 \times 38 \times 30$ mm, then degassed for 20 min with a vacuum of 80 mbar and stored in fridge for 8 h prior to use.

3.2.3 High-intensity focused ultrasound therapy and ultrasound imaging system

A schematic diagram of the HIFU therapy and ultrasound imaging system is shown in Figure 3.2. A single-element HIFU transducer (H-102, Sonic Concepts, Inc., WA, USA) was connected to a 55 dB power amplifier (A300, Electronics & Innovation, Ltd., NY, USA) via an impedance-matching network and driven at its third harmonic of 3.3 MHz McLaughlan et al. (2017), with comparatively high peak negative pressures (PNPs) to promote the onset of cavitation activity detectable by the PAM beamformers. A function generator (33250A, Keysight Technologies Uk Ltd., Berkshire, UK) was connected to the power amplifier, providing a 94 040-cycle tone burst, which was externally triggered by the UARP. An oscilloscope was used to monitor the output of the signal generator and power amplifier. A range of the free-field PNPs were used to test the focal region and cavitation activity of each HIFU. These values were measured by a UK National Physical Laboratory (NPL) calibrated differential membrane hydrophone (Precision Acoustics Ltd., Dorchester, UK) with an uncertainty of 14 % at each PNP. All PNP values (3 MPa, 4 MPa, 5 MPa, 6 MPa and 7 MPa) corresponded to the measured averaged spatial

peak intensity (I_{sp} = 2100 W cm^{-2}, 2400 W cm^{-2}, 2900 W cm^{-2}, 3300 W cm^{-2} and 3800 W cm^{-2}), with an uncertainty of 6 % at each I_{sp}. The acoustic power at these electrical drive levels was measured using an NPL-calibrated acoustic radiation force balance system (Precision Acoustics Ltd., Dorchester, UK). All experimental procedures were conducted in a water tank made of optically transparent polycarbonate, with degassed, deionised water at (20 ± 1) °C. Acoustic absorbing material was placed on the inner walls of the tank to minimise reflections.

A 128-element linear transducer (L11-4, Verasonics, Inc., WA, USA) was mounted so that the imaging plane was perpendicular to the face of the HIFU transducer, as shown in Figure 3.2(b) (XZ plane). This imaging transducer was connected to the UARP, which was programmed to synchronise the regimes for CPWI Montaldo et al. (2009), PAM and HIFU exposures. A schematic of this synchronisation is shown in Figure 3.3. For each trigger period, a 28 ms HIFU burst was transmitted while the linear array passively recorded 100 frames of PAM data. Interleaving with HIFU exposures, five-angle CPWI (data acquisition time 500 µs) was averaged into a single B-mode frame so that for each period the duty cycle was 95 %. Time delays of 500 µs and 1 ms were added before and after HIFU exposures to prevent interference in B-mode. The whole sequence was repeated 167 times so that the total time was 5 s. The sampling frequency for B-mode and PAM data was 40 MHz. The radio frequency (RF) data from both PAM and B-mode datasets was stored in UARP memory during exposure and then downloaded for post-processing in MATLAB (MathWorks, California, USA). For PAM on gel phantom and *ex vivo* tissue, the integration period was 40 µs and 781 intensity-based images were averaged into one frame. The PAM dimension was 16 × 68 and field of view was 16 × 20.4 mm^2. The computation time was recorded using MATLAB profiling tools (system CPU: Intel(R) Xeon(R) E-2124G @ 3.40 GHz and memory: 32 GB).

3.2.4 Filtering for inertial cavitation mapping

The broadband emission occurs predominantly with inertial collapse Neppiras (1969), which was isolated in this research by a cascade filter (3.12) for PAM to detect inertial cavitation activity.

$$H(z) = \frac{1 - 2cos(\frac{2\pi f_a}{f_s})z^{-1} + z^{-2}}{1 - 2rcos(\frac{2\pi f_a}{f_s})z^{-1} + r^2 z^{-2}}. \tag{3.12}$$

H(z) is the system function of this filter. f_a is the narrow-band component that

needs to be filtered ($n * f_o$, f_o is the centre frequency, n = 1/2, 1, 3/2 and 2, 5/2, 3). r is a constant number responsible for the filter bandwidth of each component (in this research, 0.8 when n = 1/2, 1, 3/2 and 0.85 when n = 2, 5/2, 3).

3.2.5 Assessment of passive acoustic mapping algorithms

To evaluate different PAM algorithms in this study, the FWHM (−6 dB) was used to measure the lateral and axial resolution (LR and AR) of the acoustic source. A_{50} was used to calculate the PSF size of the cavitation area where the pixel amplitudes were greater than −6 dB attenuation of the maximum amplitude (i.e. half of the maximum amplitude); the maximum occurs at the focal pressure location Abadi et al. (2018). Accordingly, the left area in the image was considered as the noise area.

The image contrast was quantified by axial contrast ratio (ACR) and lateral contrast ratio (LCR). The ACR is the ratio between the maximum pixel energy in the focal region and average maximum pixel energy from the axial proximal and distal focal area. The LCR is the ratio between the maximum pixel energy in the focal region and average maximum pixel energy from the lateral left and right regions of interest (ROI), shown in Figure 3.6(j). The ACR and LCR aim to give a relevant comparison between different kinds of beamformers with no physical implications.

$$\mathrm{ACR} = 10\ \log_{10} \frac{\max\left(\mathrm{I}_{\mathrm{focus}}\right)}{\mathrm{avg}\left(\mathrm{I}_{\mathrm{max(proximal+distal)}}\right)}, \tag{3.13}$$

$$\mathrm{LCR} = 10\ \log_{10} \frac{\max\left(\mathrm{I}_{\mathrm{focus}}\right)}{\mathrm{avg}\left(\mathrm{I}_{\mathrm{max(left+right)}}\right)}. \tag{3.14}$$

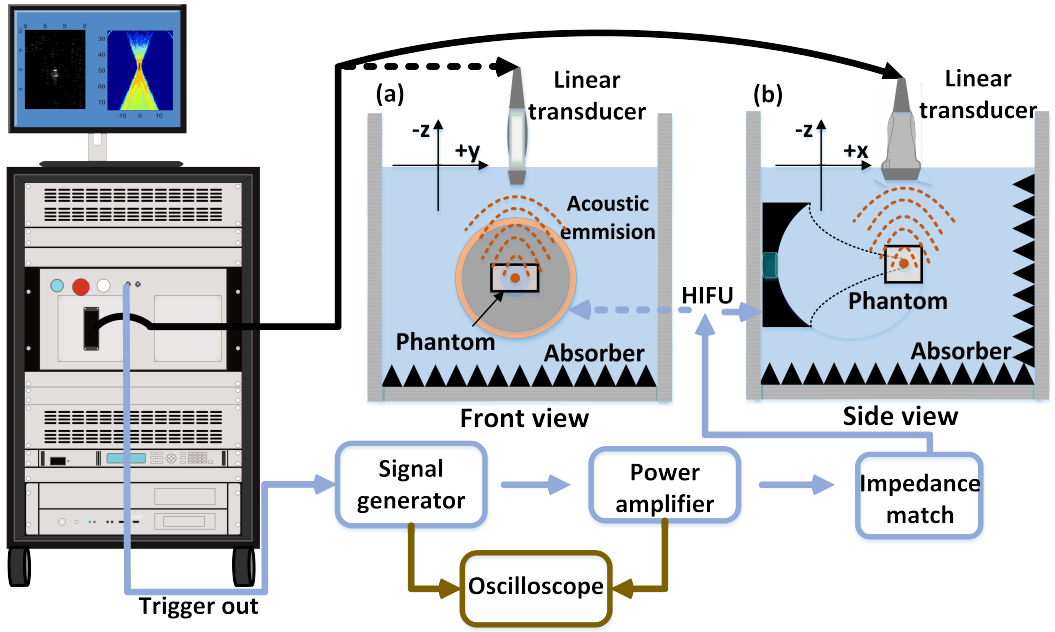

Figure 3.2: A schematic representation of the experimental setup used for gel phantoms and *ex vivo* tissue studies.

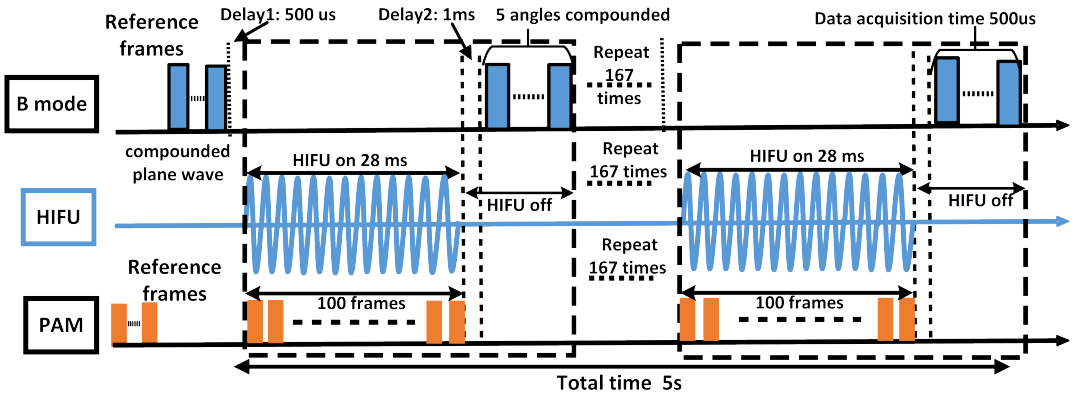

Figure 3.3: A representation of the synchronisation between pulse regimes for HIFU exposures, B-mode and PAM imaging.

3.3 Results

We first validated the raw RF (as shown in Figure 3.4) in the case of system saturation. The suppression of the axial tail noise by beamformers was subsequently analysed, as the axial width can be commonly ten times larger than the lateral width in PAM Haworth et al. (2016a). Finally, the experimental data for the suspected inertial cavitation localisation by different beamformers was described. It should be noted that the quantitative analysis of PAM image quality was compared under identical conditions only to reflect the noise suppression capability of the beamformers, whereas metrics, such as the results of LCR and ACR, are machine-adjustable due to the impact of the precision setting of the artificial negative pixels generated in coherent computation. Further analysis of this is shown in Section 3.4.2 of Discussion.

3.3.1 Radio frequency passive acoustic mapping data validation

The RF data passively acquired from a BSA gel phantom with PNP 7 MPa/I_{sp} (3800 W cm^{-2}, the highest exposure level among the settings) was manually inspected to ensure it had not saturated the ultrasound imaging system's receive circuitry, as signal saturation would cause amplitude clipping, which could result in artefact-causing broadband frequency components, ultimately resulting in misinterpretation of inertial cavitation activity.

One representative frame was analysed in this research at 142.45 ms (frame 480), as the rectified diffusion and thermal effects after hundreds of sonication cycles may enable the initial nuclei to grow to a specific size viable for collapse under inertial cavitation Gyöngy and Coussios (2009). The selected frame in Figure 3.4(a) was displayed before being realigned, and the RF data was recorded in arbitrary units in the 74th channel during cavitation activity, as shown in Figure 3.4(b), demonstrating signal integrity. Figure 3.4(c) displays the spectral cavitation information from the 74th channel in the representative PAM frame (black line) and the spectral information from the same channel at the onset of HIFU (i.e. the first PAM frame: red line). In Section 3.2.4, as the bandwidths of the narrow-band components from passively receiving data vary, the central frequency f_0 and sub-harmonic components $n/2\,f_0$ ($n = 1, 3$) are treated as dominant narrow-band components (blue rectangles) that have the same isolation parameter, 0.8. The filtering bandwidth was (0.66 ± 0.20) MHz, with isolation parameter 0.85

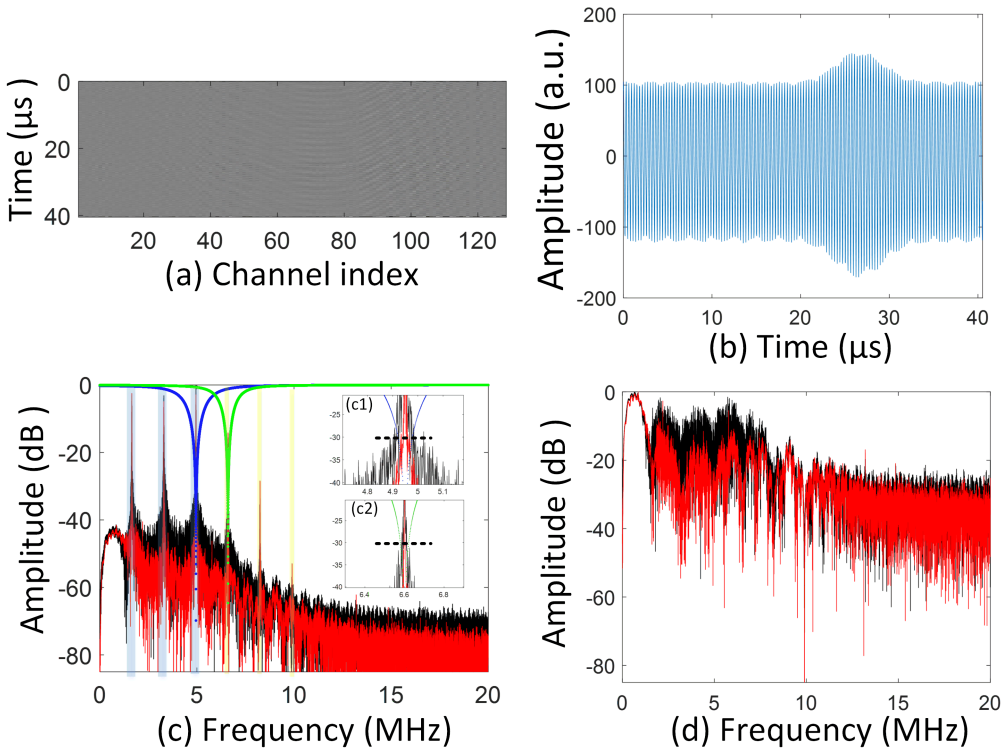

Figure 3.4: (a) Example frame (142.45 ms) of passively recorded RF data at 7 MPa, (b) the time-domain RF signal from the 74th channel of the array in this frame, (c) a frequency spectral image of the 74th channel in a representative frame (black line) and the reference floor of the first frame (red line) and (d) a frequency spectral image of the 74th channel with the broadband signal in the representative frame (black line) and first (reference) PAM frame (red line)

at -6 dB. One part of the cascade filter for $3/2\,f_0$ filtering is displayed in blue dots. Figure 3.4(c1) shows its enlarged version, from -20 dB to -40 dB. The remaining narrow components (green rectangles), including $n\,f_0$ ($n = 2, 3$) and $n/2\,f_0$ ($n = 5$), were filtered at -6 dB with the bandwidth (0.33 ± 0.20) MHz. One part of the $2f_0$ filtering is illustrated with green dots. Figure 3.4(c2) gives an enlarged view. This choice of filtering settings for the narrow-band filter were intended to isolate the components below -30 dB, as shown in Figure 3.4(c1) and (c2), to ensure only broadband information remained. Figure 3.4(d) shows the spectral image of the filtered signal with broadband information (black line). When compared with the red spectral information (which was treated as a reference noise floor), it shows a (5.0 ± 0.9) dB increase, demonstrating the presence of broadband emissions.

3.3.2 High-intensity focused ultrasound pressure field measurements

Gel phantoms and *ex vivo* bovine liver tissue were exposed to HIFU under peak negative pressure levels ranging from 3 MPa to 7 MPa (I_{sp} 2100 W cm^{-2} to 3800 W cm^{-2}). Free-field HIFU pressure measurements and corresponding PAM monitoring were used for two reasons: first, to give a general outline of the HIFU focal region as an indicator of where cavitation activity primarily occurred, as seen in the white ellipse in Figure 3.6(e) and (j), and second, to test which pressure level (or averaged spatial peak intensity) caused prominent cavitation activity in both types of phantom to enable convenient analyzation of the performance of different PAM algorithms. Figure 3.5(a) and (b) show an example of the HIFU pressure field. Figure 3.6 shows a representative PAM frame at $T = 142.45$ ms to illustrate the inertial cavitation activity in both the gel phantom and *ex vivo* liver tissue under different exposure levels. The TEA subtracting the DC components (TEA-DC) PAM algorithm was used to beamform (Figure 3.6, as derived in 3.11), with $\mathbf{w}_{\mathrm{RCB}}$ set as uniform. Figure 3.6(e) and (j) demonstrate that PNP 7 MPa is the optimal exposure level, with significant cavitation activity for the following algorithm comparisons.

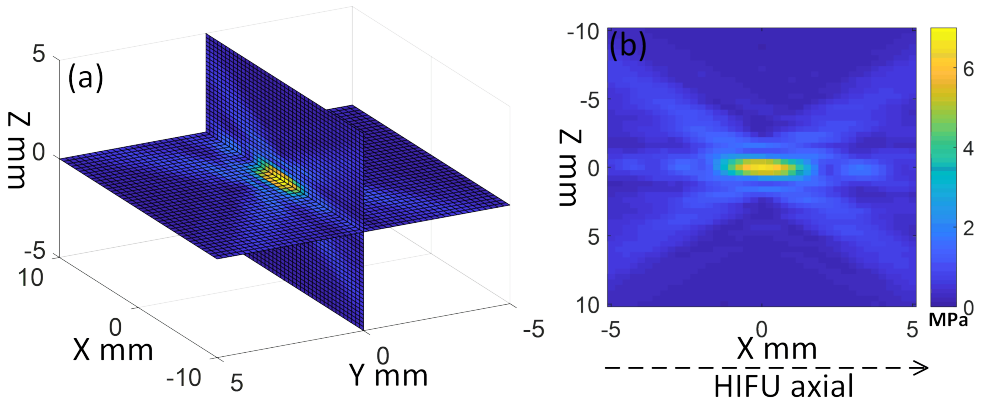

Figure 3.5: Examples of (a) three-dimensional and (b) two-dimensional (XZ plane) HIFU pressure field measurements to outline the focal region.

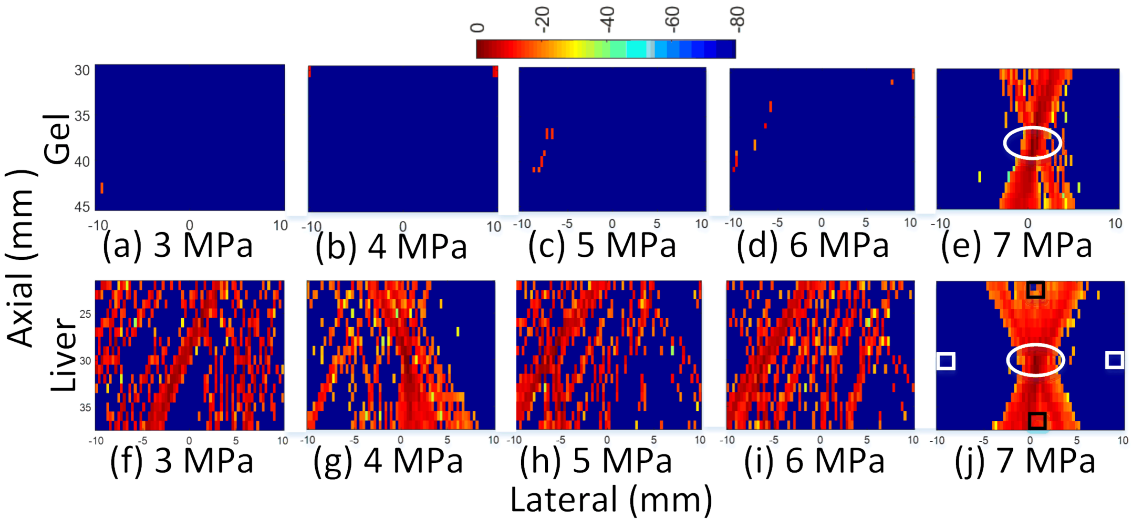

Figure 3.6: PAM frames at 142.45 ms: (a)–(e) from gel phantoms and (f)–(j) from *ex vivo* tissue. The white ellipse represents the HIFU focus, and the white and black rectangles show the lateral and axial ROI for LCR and ACR, respectively (equivalent I_{sp} values are stated in the Methods section).

3.3.3 Axial tail artefact suppression

Previous studies have demonstrated that the reverberations between multiple cavitation events and the diffraction pattern of the imaging array may contribute to the appearance of axial tail artefacts Coviello et al. (2015); Haworth et al. (2012). Adaptive beamforming algorithms, such as CB and RCB, have demonstrated tail artefact suppression capability, particularly the RCB approach, as it accounts for array imperfections, etc. To select a value for ϵ, we followed similar procedures to those of Coviello et al. (2015); Li et al. (2003); Lu et al. (2018). In the present study, the values of ϵ for all RCB based methods (i.e. RCB, E-RCB, WE-RCB and RCB-DC) were chosen through PAM experiments on gel phantoms and *ex vivo* tissue as 0.5 and 8, respectively.

Figure 3.7(a) and (e), (b) and (f), and (c) and (g) were beamformed by TEA, TEA-DC and RCB, respectively. The tail artefacts are significant; they are presented as an elongated region of acoustic energy beyond the focal region in the axial direction in Figure 3.7(a) and (e), and (b) and (f). Figure 3.7(c) and (g) show the ability of RCB to mitigate this type of artefact. However, in these measurements with the presented dynamic ranges, residual DC components are observable. Thus, the joint effects of DC reduction and robust weighting vectors to suppress the tail artefacts were analysed. The comparison between TEA and TEA-DC is intended to consider the effect of DC component reduction. The ACR of Figure 3.7(b) and (f) increased from (18 ± 6) dB and (19 ± 7) dB (Figure 3.7[a] and [e]) to (33 ± 7) dB and (27 ± 6) dB, respectively, as shown in Figure 3.7(i). Analysing the differences between TEA and RCB with regard to the effect of optimal weighting vectors, the ACR of Figure 3.7(c) and (g) increased from (18 ± 6) dB and (19 ± 7) dB (Figure 3.7[a] and [e]) to (20 ± 5) dB and (20 ± 4) dB, respectively, a less significant suppression when compared with the DC component reduction. When taking into account the DC component reduction and optimal weighting vectors in RCB-DC, as shown in Figure 3.7(d) and (f), the ACR of RCB-DC is (157.0 ± 0.5) dB, demonstrating increases of 139 dB (TEA), 124 dB (TEA-DC) and 137 dB (RCB) on gel phantoms and 138 dB (TEA), 130 dB (TEA-DC) and 137 dB (RCB) in *ex vivo* tissue. Between 86 % and 94 % more noise area was consistently removed in RCB-DC than in TEA. The LCR of RCB-DC is (157.0 ± 0.5) dB, which shows that background noise has also been efficiently suppressed (Figure 3.7[j]).

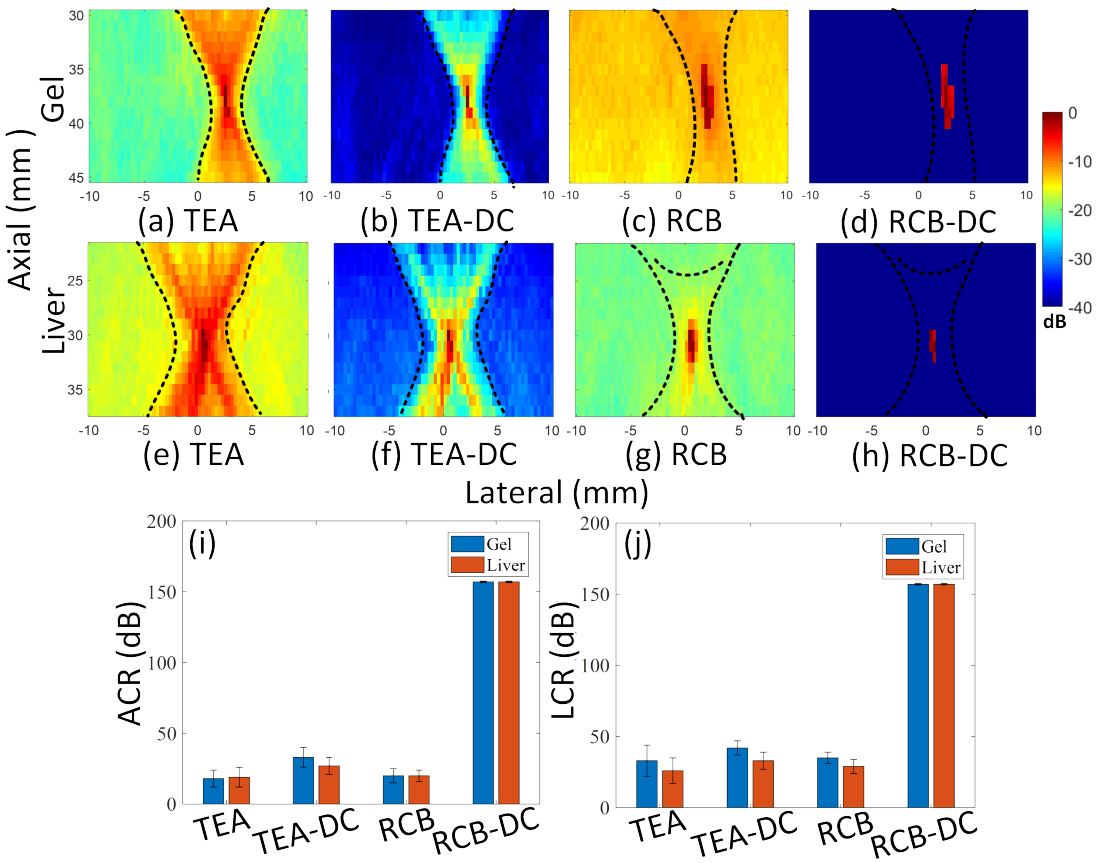

Figure 3.7: PAM results from gel phantoms (a)–(d) and *ex vivo* tissue (e)–(h), beamformed by (from left to right) TEA, TEA-DC, RCB and RCB-DC at PNP 7 MPa. The broken lines indicate the scope of axial tail artefacts. (i) and (j) show corresponding ACR and LCR values.

3.3.4 Experiment: gel phantom

It was expected that cavitation activity would primarily occur within the white elliptical focal area shown in Figure 3.6(e) and (j). However, much of the inertial cavitation region beamformed by TEA shown in Figure 3.8(a) takes place axially outside of that region, i.e. in contrast to experimental expectations. The CB shown in Figure 3.8(b) has worse performance than TEA, as illustrated by Table 3.3. This could be caused by several factors, such as the degraded quality of the imaging array with poor element sensitivity, speed of sound variations in the propagating-path and media attenuation Lyka et al. (2018). These factors may be mitigated by the diagonal loading technique, which aims to increase CB robustness. To compensate for CB performance, RCB ($\epsilon = 0.5$) can be considered as a version of the adaptive diagonal loading technique; the parameter ϵ allows for a given ellipsoidal uncertainty set of the steering vector Li et al. (2003). The AR and LR of Figure 3.8(c) show little improvement over TEA, where the LCR and ACR are both improved by approximately 2 dB. The E-RCB projects the RCB weighting vectors onto the signal subspace to further suppress interference, as the noise subspace is orthogonal to the signal subspace Lu et al. (2018). The parameter α is generally specified as 0.1 to 0.5 to determine the threshold of the signal subspace that relates to the largest eigenvalues corresponding to the inertial cavitation energy Asl and Mahloojifar (2010). The procedures to select parameter α for E-RCB are the same as those suggested by Lu et al. (2018) and Asl and Mahloojifar (2010). In the present study, α was chosen as 0.1, and Figure 3.8(d) shows the significant improvements in LCR (46 dB), ACR (37 dB), LR (0.1 mm) and AR (1.3 mm) when compared with RCB. For WE-RCB, the Wiener post-filter optimises the E-RCB weighting vector to modify the output power of E-RCB to closer to the true signal power if the estimates of the signal power and output noise power are accurate Nilsen and Holm (2010); Zeng et al. (2012). Here, the estimate is developed by eigen-decomposition using the signal and noise covariance matrix constructed by signal and noise subspaces. Figure 3.8(e) shows a reduction in LR (0.1 mm) and AR (0.3 mm) and an increase in LCR (3 dB) and ACR (5 dB) when compared with E-RCB.

The proposed RCB-DC method works as an unbiased image estimator applied with robust weighting vectors that is approximately 7 s to 8 s faster than E-RCB and WE-RCB per intensity-based image, as it does not introduce the complexity of the covariance matrix eigen-decomposition and the Wiener post-filter. Moreover,

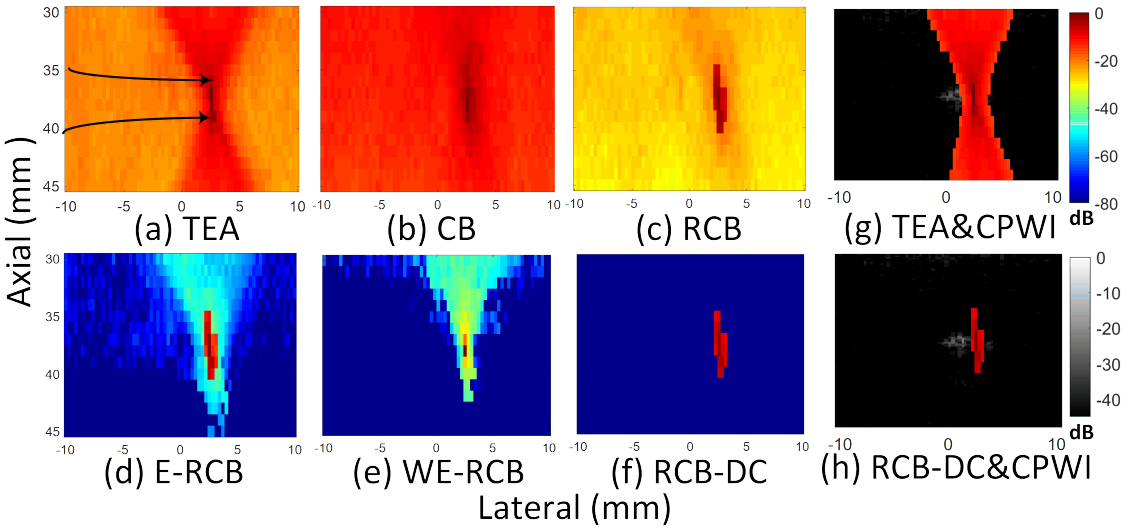

Figure 3.8: The representative PAM frame at 142.45 ms on gel phantoms, beamformed by (a) TEA (the cure arrow indicates the HIFU beam), (b) CB, (c) RCB, (d) E-RCB, (e) WE-RCB and (f) the proposed algorithm RCB-DC, at PNP 7 MPa. (g) and (h) are TEA and RCB-DC overlapped with B-mode (CPWI), respectively.

the LCR of RCB-DC increased by 348.6 % (122 dB) when compared with RCB, 93.8 % (76 dB) when compared with E-RCB and 86.9 % (73 dB) when compared with WE-RCB. Similarly, the ACR of RCB-DC improved by 685 % (137 dB) when compared with RCB, 175.4 % (100 dB) when compared with E-RCB and 153.3 % (95 dB) when compared with WE-RCB. The LR and AR of RCB-DC measured in the gel phantoms were not improved over E-RCB and WE-RCB, which already had a satisfactory value of approximately 0.3 mm. The PSF sizes estimated by A_{50} show smaller values for RCB than TEA, which is consistent with the results reported by Coviello et al. (2015). For WE-RCB, one pixel size is slightly superior to E-RCB, which is expected because the Wiener post-filter further improved suppression. The PSF size with RCB-DC remained the same as with RCB. The reason for this is that RCB-DC only mitigates the background noise from DC components, retaining the same inertial cavitation information. Figure 3.8(h) contrasts with Figure 3.8(g); due to the improved tail artefact suppression of RCB-DC, the cavitation dose information with PAM more aligned with the hyperechogenicity with B-mode, facilitating more potential for further analyzation related to physical meaning.

	Algorithm	CT (s)	LR (mm)	AR (mm)	LCR (dB)	ACR (dB)	A_{50} (mm^2)
Gel	TEA	0.07 ± 0.01	0.3 ± 0.1	3.2 ± 1.1	33 ± 11	18 ± 6	1.5 ± 0.3
	CB	92.7±0.2	1.7 ± 0.9	8.9 ± 3.9	13 ± 1	9 ± 3	1.8 ± 0.3
	RCB	98.1±0.5	0.3 ± 0.1	3.1 ± 1.2	35 ± 4	20 ± 5	1.2 ± 0.3
	E-RCB	104.8 ± 0.9	0.2 ± 0.1	1.8 ± 0.8	81 ± 25	57 ± 9	1.2 ± 0.3
	WE-RCB	106.5 ± 1.8	0.1±0.04	1.5 ± 1.0	84 ± 26	62 ± 12	0.6 ± 0.3
	RCB-DC	98.4±0.6	0.3 ± 0.1	2.5 ± 1.2	157 ± 0.5	157±0.5	1.2 ± 0.3

Table 3.3: Computation time (CT) per intensity-based image, lateral resolution (LR), axial resolution (AR), lateral contrast ratio (LCR), axial contrast ratio (ACR) and A_{50} when beamforming with different PAM algorithms for HIFU on a gel phantom.

3.3.5 Experiment: *ex vivo* bovine liver tissue

Due to its potential for monitoring drug delivery and similar applications, PAM is commonly demonstrated in studies with the introduction of external cavitation nuclei (e.g. microbubbles) Gyöngy and Coussios (2009); Haworth et al. (2016a, 2012, 2016b); Lu et al. (2018). In this study, PAM was used for monitoring during qCW exposures in tissue, approaching the experimental conditions used for clinical thermal applications Ebbini and Ter Haar (2015). This scenario presents additional experimental challenges for PAM algorithms, such as a lower SNR due to greater tissue scattering and weaker acoustic cavitation activity.

Table 3.4 for PAM beamformers in *ex vivo* tissue shows a similar trend to that seen in the gel phantom experiments (see Table 3.3). The Computation Time (CT) per intensity-based image of the proposed method, RCB-DC, on *ex vivo* liver was faster than that of E-RCB (by approximately 4 s) and WE-RCB (by approximately 7 s). It should be noted that in this research, the CT is an indicator only of the relative efficiency of the algorithms. The LCR of RCB-DC showed increases of 441.4 % (128 dB) over RCB and 93.8 % (76 dB) over E-RCB and WE-RCB. The ACR of RCB-DC showed improvements of 685 % (137 dB) over RCB and 109.3 % (82 dB) over E-RCB and WE-RCB. The A_{50} varied by no more than 25 % between RCB and RCB-DC methods and TEA, which demonstrates the consistency of the available inertial cavitation information in the proposed method.

Notably, the metrics (excluding CT) in Table 3.4 are the same for E-RCB and WE-RCB. The reason for this is that the parameter α for the eigen-decomposition was 0.4, which may give an accurate estimation of the signal and noise subspace. While the power of the signal subspace was much larger than the power of the noise subspace, which resulted in the output for E-RCB- and WE-RCB-based PAM, both were close to the real signal power (see Appendix 3.6). Figure 3.9(h) contrasts with Figure 3.9(g), as discussed in Section 3.3.4. Figure 3.9(h) is overlaid with the corresponding B-mode image to provide spatial information for the cavitation location, as the tail artefacts and background noise were been greatly mitigated by RCB-DC. Furthermore, the inertial cavitation activity presented in Figure 3.9(h) was approximately 1 mm away from the focal spot, which may be due to the occurrence of a boiling-bubble cluster (presented as the hyperechoic region in B-mode) caused by the asymmetrically ablated region. Figure 3.9(i) shows asymmetric liver lesion formation with typical 'tadpole' appearance under 5 s qCW HIFU exposure, laying the foundation for revealing the quantitative re-

	Algorithm	CT(s)	LR(mm)	AR(mm)	LCR(dB)	ACR(dB)	$A_{50}(mm^2)$
Tissue	TEA	0.07 ± 0.01	0.9 ± 0.3	4.4 ± 1.7	26 ± 9	19 ± 7	1.8 ± 0.3
	CB	93.1±1.1	2.2 ± 1.3	7.9 ± 2.8	9 ± 3	8 ± 2	2.4 ± 0.6
	RCB	99.2±0.9	0.5 ± 0.2	2.4 ± 1.1	29 ± 5	20 ± 4	1.5 ± 0.3
	E-RCB	103.3 ± 1.2	0.3 ± 0.2	1.3 ± 0.6	81 ± 30	75 ± 34	1.5 ± 0.3
	WE-RCB	106.3 ± 1.4	0.3 ± 0.2	1.3 ± 0.6	81 ± 30	75 ± 34	1.5 ± 0.3
	RCB-DC	99.3±1.0	0.3 ± 0.2	1.2 ± 0.6	157 ± 0.5	157±0.5	1.5 ± 0.3

Table 3.4: Metrics for the comparison of different PAM algorithms for HIFU on *ex vivo* liver tissue.

lationship between the sizes of the *ex vivo* ablation lesion, PAM cavitation region and hyperechoic area in B-mode.

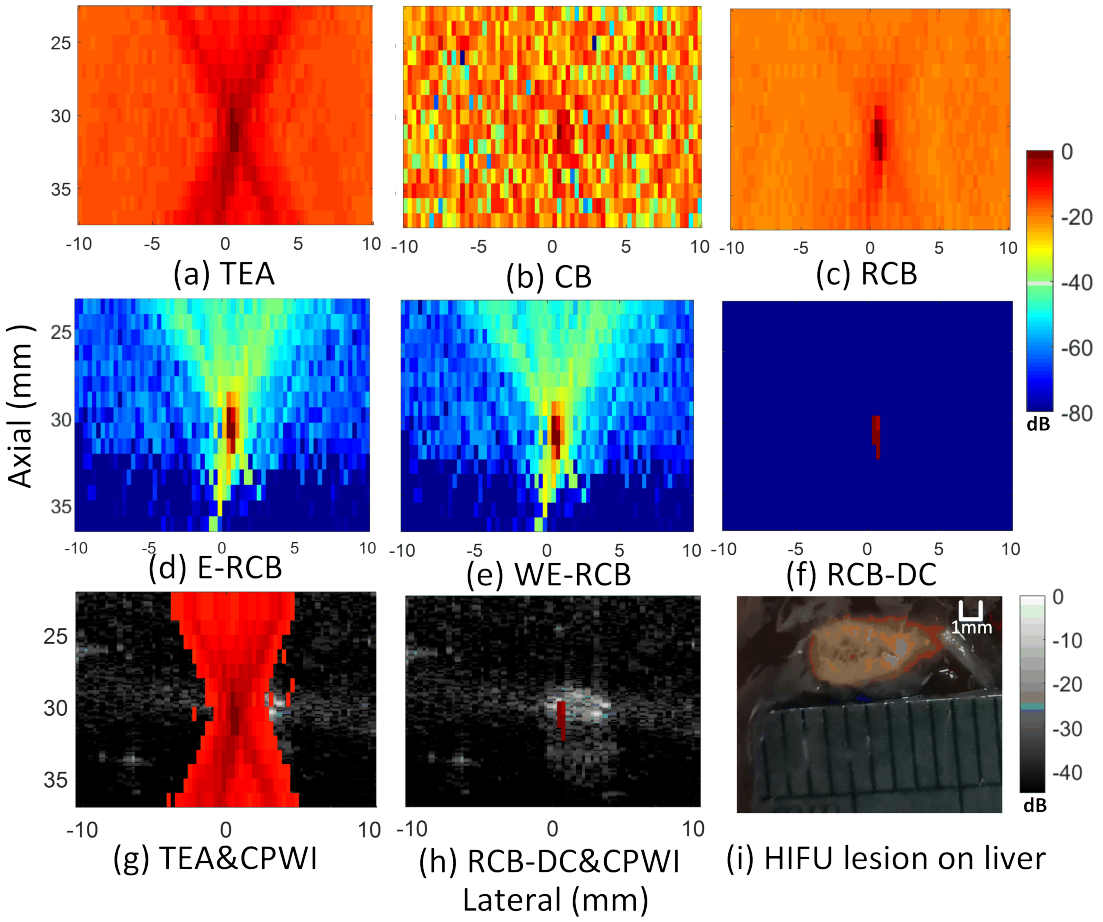

Figure 3.9: The representative PAM frame at 142.45 ms on *ex vivo* tissue, beamformed by (a) TEA, (b) CB, (c) RCB, (d) E-RCB, (e) WE-RCB and (f) the proposed algorithm RCB-DC at PNP 7 MPa. (g) and (h) are TEA and RCB-DC overlaid with B-mode (CPWI), respectively. (i) is the HIFU lesion on *ex vivo* liver tissue.

3.4 Discussion

3.4.1 Analysis of cavitation-related phenomena

Figure 3.6(f)–(i) show the inertial cavitation activity in *ex vivo* tissue with an exposure level below 7 MPa, with greater side-lobe interference than the equivalent exposure in gel phantoms (see Figure 3.6[a]–[d]). This is likely due to the *ex vivo* tissue generally having higher attenuation McLaughlan et al. (2017) than the gel phantom. Thus, it is easier to cause a temperature rise in *ex vivo* tissue, which results in a reduction in the pressure threshold required to generate acoustic cavitation McLaughlan (2008). Furthermore, unlike the gel phantoms, the *ex vivo* liver samples represent an inhomogeneous highly vascular medium, which may result in the presence of nuclei within the focal region, increasing the cavitation activity.

In addition to the presence of inertial cavitation shown in Section 3.3.1, the strong harmonics in Figure 3.4(c) and the hyperechogenicity in the interleaved CPWI shown in Figure 3.8(g) and (h) and Figure 3.9(g) and (h) (i.e. acquired at the end of each HIFU exposure repetition with certain time gaps, see Figure 3.3), demonstrate that boiling may have occurred after HIFU at 142 ms with 7 MPa in the BSA phantom. This phenomenon coincides with the findings of Khokhlova et al. (2011), which showed that boiling can occur from HIFU exposure in less than 2 ms, especially when the targeted depth is shallow. With PNP of 5–6 MPa in the BSA phantom, there was no inertial cavitation detected, as shown in Figure 3.6(c) and (d). This may be due to the relative insensitivity of PAM in this context (according to the beamforming step setting). Further research could be validated by combining a confocal PCD with the H-102 HIFU transducer for cavitation analysis. It should be noted that the image of a HIFU lesion on liver shown in Figure 3.9(i) was produced after full HIFU exposure.

3.4.2 Passive acoustic mapping image characteristics

Three PAM image characteristics are of concern in this research: tail artefacts, image pixelisation and negative artificial pixels. In addition to the factors mentioned in Section 3.3.3, the reasons for the generation of the tail artefacts are complex, and the axial tail artefact could be understood as the nature of summation of the point spread functions from the targeting sources. Additionally, as mentioned by Li et al. (2019), a correct time origin leads to reconstruct PAM with a point-

shaped pattern. Essentially, this is to reduce the averaging intensity-based bins with diverging-pattern axial side lobes into one frame; however, confirmation of the optimal time origin point for PAM monitored clinical surgery still needs to more efforts to be achieved.

The binary PAM structure is demonstrated in discrete jumps or pixelisation (especially along the axial direction), which are obvious in Figures 3.6, 3.7, 3.8 and 3.9. This phenomenon largely depends on the beamforming step setting. A relatively small beamforming step can give the image a smooth appearance. The theoretical optimal step size (the distance between pixel centres) should be larger than the spatial coherence length of noise (this can be approximated by the speed of sound divided by the noise bandwidth) which can improve the spatial resolution Norton and Won (2000). The axial beamforming step in this research was 1 mm, which may be too sparse that generate discrete jumps for the beamforming output and may have degraded the image quality, as a step size of 1 mm may cause the realigned waveform to have sparse density, which may hinder the realigned data being summed constructively. The degraded image quality could further impact the sensitivity in distinguishing cavitation activity of variable energy levels for quantitative analysis. Conversely, although the optimal step size could mitigate the above situations, the computation cost would increase exponentially. A compromise to optimise the parameters to mitigate the related impact deserves further investigation.

When computing the proposed method using Equation 3.11, the coherence is weak in the steered array data at the specific pixel, and subtraction of the DC component will result in artificial negative pixels. This is commonly seen in coherent beamforming calculations Haworth et al. (2016a); Stanziola et al. (2018). The reasons may lie in the off-axis echoes generated from the side lobes of the passively received data originating in the high-amplitude region (e.g. cavitation occurring zone), which reverberates with the ambient noise (e.g. from electronic system noise, omni-reflection of the HIFU beam via cavitation, etc.) in the lower-amplitude region (that is outside the cavitation region). The reverberation between the off-axis echoes and the ambient noise may generate incoherent noise in the echoes from the lower-amplitude region, thereby introducing artificial negative pixels. This coincides with the research by Stanziola et al. (2018), which recognised the negative correlation values from the contribution of side and grating lobes as interference. Consequently, Stanziola et al. (2018) set all the negative correlated artificial values at zero for the decibel displaying convenience and noise

suppression. Alternatively, Haworth et al. (2016a) replaced the negative phenomena with the MATLAB eps function; this was also adopted in the present research. The impact of such replacement for this research was that the precision setting (double or single) of eps may have changed the results of the metrics in Tables 3.3 and 3.4; for example, the LCR and ACR were 156.5 dB for the eps double setting. For the eps single setting, the ACR and LCR would be about 69 dB. Under these circumstances, RCB-DC would be closer to a 35–50 dB than a 125–140 dB improvement. However, as long as all the beamformers are compared under identical conditions, the relative comparisons should be available (without representing any physical implications).

3.4.3 Computation complexity

The relative-time beamforming technique was applied in this research due to its high duty cycle and long HIFU exposure. Consequently, the averaging of the intensity-based images into one frame within the bubble-event time interval is one of the dominant reasons for the increased computation expense of time-domain PAM. For adaptive beamformers in the frequency domain, the spatial covariance matrix can be calculated directly from RF data and efficiently steered with fast matrix composition Polichetti et al. (2020). Also, the interested frequency bins can be selected to be superimposed into one frame. These factors may lead to a significant reduction in computation time Arvanitis et al. (2016); Haworth et al. (2016a). The computation time shown in Tables 3.3 and 3.4 demonstrates that the presented studies have some way to go before real-time implementation. Graphics processing unit (GPU)-accelerated sparse matrix-based beamforming has developed into time-domain TEA for real-time monitoring Kamimura et al. (2020), which indicates a possible complementary direction for the proposed method and for the next step in ongoing studies.

3.4.4 Algorithm perspectives

This research focused on the illustration of noise suppression via adaptive PAM beamformers and DC reduction. If the sensitivity and position of the imaging array per element were calibrated, the results would be improved without the need for time-consuming algorithms. Furthermore, by incorporating GPU-based techniques Kamimura et al. (2020), real-time PAM monitoring could be expected.

The size of the spread of cavitation energy is quantified in Tables 3.3 and 3.4;

the A_{50} was analysed to demonstrate the consistency of the available cavitation area. A complementary procedure is to set a PAM simulator (illustrated in chapter 4), which will enable the convenience of the quantitative comparison of simulated PAM results for different types of beamformers in case of over-suppression and give access to power quantification, specifically related to the precision with which algorithms appropriately map cavitation.

Finally, the current imaging system, seen in Figure 3.2, confines cavitation in a two-dimensional plane, whereas cavitation is naturally a three-dimensional phenomenon. The potential concern of this is that out-plane bubble activities may not only be missed but also generate spatial artefacts on the two-dimensional mapping, especially for the noise effects across planes from DC components, as can be generated as a large bias when more intensity-based bins need to be accumulated for PAM monitored long-pulse HIFU Norton et al. (2006). This again emphasises the need to investigate adaptive beamformers with DC reduction for the noise suppression of two-dimensional monitoring in this research and prepare for the three-dimensional monitoring for clinical use.

3.5 Conclusions

In the passive monitoring of CW and qCW HIFU exposure, averaging is an essential procedure for relative-time-delay beamformers, but the accumulation of DC components causes significant background noise in PAM images. This study has shown the potential of DC reduction combined with a robust beamformer for noise suppression as a tool for ultrasound therapy monitoring with high duty cycle. In addition to relevant comparisons between beamformers, complex quantitative analysis with metrics was performed on many related phenomena, including PAM image characteristics .etc. With further optimisation of beamformers, this research will be concerned with approaching real-time operation via integration into an in-house-developed ultrasound system for cavitation-relevant applications.

3.6 Appendix

The output power of the E-RCB-based beamformer for each intensity-based image (bin) can be developed as:

$$\begin{aligned} I_{\mathrm{E-RCB}} &= (s_n \mathbf{w}_{\mathrm{E-RCB}})^H s_n \mathbf{w}_{\mathrm{E-RCB}} \\ &= \mathbf{w}_{\mathrm{E-RCB}}^H s_n s_n \mathbf{w}_{\mathrm{E-RCB}} \\ &= \mathbf{w}_{\mathrm{E-RCB}}^H \boldsymbol{R} \mathbf{w}_{\mathrm{E-RCB}} \\ &= \mathbf{w}_{\mathrm{E-RCB}}^H \boldsymbol{U}_s \boldsymbol{U}_s^H (\boldsymbol{U}_s \Lambda_s^{-1} \boldsymbol{U}_s^H + \boldsymbol{U}_n \Lambda_n^{-1} \boldsymbol{U}_n^H) \mathbf{w}_{\mathrm{E-RCB}} \\ &= S_{\mathrm{E-RCB}}^2 + \mathbf{w}_{\mathrm{E-RCB}}^H \boldsymbol{U}_s \boldsymbol{U}_s^H \boldsymbol{U}_n \Lambda_n^{-1} \boldsymbol{U}_n^H \boldsymbol{U}_s \boldsymbol{U}_s^H \mathbf{w}_{\mathrm{E-RCB}} \\ &= S_{\mathrm{E-RCB}}^2 + \underbrace{\mathbf{w}_{\mathrm{E-RCB}}^H \boldsymbol{R}_s \mathbf{w}_{\mathrm{E-RCB}}}_{\text{suppressed component}}, \end{aligned} \tag{3.15}$$

The eigenvalues are sorted in descending order. We select $\alpha = 0.4$ (usually between 0.1 to 0.5) times-largest eigenvalues for the signal subspace $S_{\mathrm{E-RCB}}^2$ to beamform each intensity-based bin, which determines that the $S_{\mathrm{E-RCB}}^2$ is comparatively much larger than the $\mathbf{w}_{\mathrm{E-RCB}}^H \boldsymbol{R}_s \mathbf{w}_{\mathrm{E-RCB}}$ (noise subspace).

The output power of the WE-RCB-based beamformer for each intensity-based bin can be expressed as:

$$I_{\mathrm{WE-RCB}} = \mathbf{w}_{\mathrm{WE-RCB}}^H \, \boldsymbol{R} \, \mathbf{w}_{\mathrm{WE-RCB}}, \tag{3.16}$$

The apodisation function related to WE-RCB in equation 3.10 can be re-formulated as:

$$\begin{aligned}\mathbf{w}_{\mathrm{WE-RCB}} &= \frac{\mathbf{w}_{\mathrm{E-RCB}}{}^{H}\, \boldsymbol{R}_s\, \mathbf{w}_{\mathrm{E-RCB}}}{\mathbf{w}_{\mathrm{E-RCB}}{}^{H}\, \boldsymbol{R}\, \mathbf{w}_{\mathrm{E-RCB}}}\mathbf{w}_{\mathrm{E-RCB}} \\ &= \frac{S^2_{E-RCB}}{S^2_{E-RCB} + \mathbf{w}_{\mathrm{E-RCB}}{}^{H}\, \boldsymbol{R}\, \mathbf{w}_{\mathrm{E-RCB}}}\mathbf{w}_{\mathrm{E-RCB}},\end{aligned} \tag{3.17}$$

To substitute equation 3.17 into 3.16, the formulation can be shown as:

$$\begin{aligned}I_{\mathrm{WE-RCB}} &= \left(\frac{S^2_{E-RCB}}{S^2_{E-RCB} + \mathbf{w}_{\mathrm{E-RCB}}{}^{H}\, \boldsymbol{R}\, \mathbf{w}_{\mathrm{E-RCB}}}\right)^2 \\ &\quad \times \mathbf{w}_{\mathrm{E-RCB}}\, \boldsymbol{R}\, \mathbf{w}_{\mathrm{E-RCB}} \\ &= \left(\frac{S^2_{E-RCB}}{S^2_{E-RCB} + \mathbf{w}_{\mathrm{E-RCB}}{}^{H}\, \boldsymbol{R}\, \mathbf{w}_{\mathrm{E-RCB}}}\right)^2 \\ &\quad \times \left(S^2_{E-RCB} + \mathbf{w}_{\mathrm{E-RCB}}{}^{H}\, \boldsymbol{R}\, \mathbf{w}_{\mathrm{E-RCB}}\right) \\ &= \frac{S^4_{E-RCB}}{S^2_{E-RCB} + \mathbf{w}_{\mathrm{E-RCB}}{}^{H}\, \boldsymbol{R}\, \mathbf{w}_{\mathrm{E-RCB}}} \\ &= S^2_{E-RCB} - \frac{\mathbf{w}_{\mathrm{E-RCB}}{}^{H}\, \boldsymbol{R}\, \mathbf{w}_{\mathrm{E-RCB}}}{1 + \frac{\mathbf{w}_{\mathrm{E-RCB}}{}^{H}\, \boldsymbol{R}\, \mathbf{w}_{\mathrm{E-RCB}}}{S^2_{E-RCB}}},\end{aligned} \tag{3.18}$$

As the S^2_{E-RCB} is relatively much larger than $\mathbf{w}^H_{\mathrm{E-RCB}}\boldsymbol{R}_s\mathbf{w}_{\mathrm{E-RCB}}$, the component $\frac{\mathbf{w}_{\mathrm{E-RCB}}{}^{H}\, \boldsymbol{R}\, \mathbf{w}_{\mathrm{E-RCB}}}{S^2_{E-RCB}}$ is approximately identical to 0. Therefore, equation 3.18 can be simply expressed as:

$$I_{\mathrm{WE-RCB}} = S^2_{E-RCB} - \underbrace{\mathbf{w}_{\mathrm{E-RCB}}{}^{H}\, \boldsymbol{R}\, \mathbf{w}_{\mathrm{E-RCB}}}_{\text{much smaller component}} \approx S^2_{E-RCB}, \tag{3.19}$$

which is approximately identical to equation 3.15:

$$I_{\mathrm{WE-RCB}} \approx S^2_{E-RCB} = I_{\mathrm{E-RCB}}. \tag{3.20}$$

Chapter References

Abadi S.H., Haworth K.J., Mercado-Shekhar K.P. and Dowling D.R. (2018). Frequency-sum beamforming for passive cavitation imaging. *The Journal of the Acoustical Society of America*, **144**(1), pp. 198–209.

Al-Bataineh O., Jenne J. and Huber P. (2012). Clinical and future applications of high intensity focused ultrasound in cancer. *Cancer treatment reviews*, **38**(5), pp. 346–353.

Arvanitis C.D., Crake C., McDannold N. and Clement G.T. (2016). Passive acoustic mapping with the angular spectrum method. *IEEE transactions on medical imaging*, **36**(4), pp. 983–993.

Arvanitis C.D., Livingstone M.S. and McDannold N. (2013). Combined ultrasound and mr imaging to guide focused ultrasound therapies in the brain. *Physics in Medicine & Biology*, **58**(14), p. 4749.

Arvanitis C.D. and McDannold N. (2013). Integrated ultrasound and magnetic resonance imaging for simultaneous temperature and cavitation monitoring during focused ultrasound therapies. *Medical physics*, **40**(11), p. 112901.

Asl B.M. and Mahloojifar A. (2010). Eigenspace-based minimum variance beamforming applied to medical ultrasound imaging. *IEEE transactions on ultrasonics, ferroelectrics, and frequency control*, **57**(11), pp. 2381–2390.

Bailey M., Khokhlova V., Sapozhnikov O., Kargl S. and Crum L. (2003). Physical mechanisms of the therapeutic effect of ultrasound (a review). *Acoustical Physics*, **49**(4), pp. 369–388.

Blana A., Walter B., Rogenhofer S. and Wieland W.F. (2004). High-intensity focused ultrasound for the treatment of localized prostate cancer: 5-year experience. *Urology*, **63**(2), pp. 297–300.

Boulos P., Varray F., Poizat A., Ramalli A., Gilles B., Bera J.C. and Cachard C. (2018). Weighting the passive acoustic mapping technique with the phase coherence factor for passive ultrasound imaging of ultrasound-induced cavitation. *IEEE transactions on ultrasonics, ferroelectrics, and frequency control*, **65**(12), pp. 2301–2310.

Bull V., Civale J., Rivens I. and ter Haar G. (2013). A comparison of acoustic cavitation detection thresholds measured with piezo-electric and fiber-optic hydrophone sensors. *Ultrasound in medicine & biology*, **39**(12), pp. 2406–2421.

Burgess M., Apostolakis I. and Konofagou E. (2018). Power cavitation-guided blood-brain barrier opening with focused ultrasound and microbubbles. *Physics in Medicine & Biology*, **63**(6), p. 065009.

Chan A.H., Fujimoto V.Y., Moore D.E., Martin R.W. and Vaezy S. (2002). An image-guided high intensity focused ultrasound device for uterine fibroids treatment. *Medical physics*, **29**(11), pp. 2611–2620.

Choi J.J., Carlisle R.C., Coviello C., Seymour L. and Coussios C.C. (2014). Non-invasive and real-time passive acoustic mapping of ultrasound-mediated drug delivery. *Physics in Medicine & Biology*, **59**(17), p. 4861.

Choi J.J. and Coussios C.C. (2012). Spatiotemporal evolution of cavitation dynamics exhibited by flowing microbubbles during ultrasound exposure. *The Journal of the Acoustical Society of America*, **132**(5), pp. 3538–3549.

Coussios .C., Farny C., Ter Haar G. and Roy R. (2007). Role of acoustic cavitation in the delivery and monitoring of cancer treatment by high-intensity focused ultrasound (hifu). *International Journal of Hyperthermia*, **23**(2), pp. 105–120.

Coviello C., Kozick R., Choi J., Gyöngy M., Jensen C., Smith P.P. and Coussios C.C. (2015). Passive acoustic mapping utilizing optimal beamforming in ultrasound therapy monitoring. *The Journal of the Acoustical Society of America*, **137**(5), pp. 2573–2585.

Cowell D., Carpenter T., Smith P., Adams C., Harput S. and Freear S. (2016). Performance of switched mode arbitrary excitation using harmonic reduction pulse width modulation (hrpwm) in array imaging applications. In: *2016 IEEE International Ultrasonics Symposium (IUS)*. IEEE, pp. 1–4.

Crake C., de Saint Victor M., Owen J., Coviello C., Collin J., Coussios C.C. and Stride E. (2015). Passive acoustic mapping of magnetic microbubbles for cavitation enhancement and localization. *Physics in Medicine & Biology*, **60**(2), p. 785.

Ebbini E.S. and Ter Haar G. (2015). Ultrasound-guided therapeutic focused ultrasound: current status and future directions. *International journal of hyperthermia*, **31**(2), pp. 77–89.

Farny C.H., Holt R.G. and Roy R.A. (2009). Temporal and spatial detection of hifu-induced inertial and hot-vapor cavitation with a diagnostic ultrasound system. *Ultrasound in medicine & biology*, **35**(4), pp. 603–615.

Gyongy M., Arora M., Noble J.A. and Coussios C.C. (2008). Use of passive arrays for characterization and mapping of cavitation activity during hifu exposure. In: *2008 IEEE Ultrasonics Symposium*. IEEE, pp. 871–874.

Gyöngy M. and Coussios C.C. (2009). Passive spatial mapping of inertial cavitation during hifu exposure. *IEEE Transactions on Biomedical Engineering*, **57**(1), pp. 48–56.

Harput S., Arif M., McLaughlan J., Cowell D.M. and Freear S. (2013). The effect of amplitude modulation on subharmonic imaging with chirp excitation. *IEEE transactions on ultrasonics, ferroelectrics, and frequency control*, **60**(12), pp. 2532–2544.

Haworth K.J., Bader K.B., Rich K.T., Holland C.K. and Mast T.D. (2016a). Quantitative frequency-domain passive cavitation imaging. *IEEE transactions on ultrasonics, ferroelectrics, and frequency control*, **64**(1), pp. 177–191.

Haworth K.J., Mast T.D., Radhakrishnan K., Burgess M.T., Kopechek J.A., Huang S.L., McPherson D.D. and Holland C.K. (2012). Passive imaging with pulsed ultrasound insonations. *The Journal of the Acoustical Society of America*, **132**(1), pp. 544–553.

Haworth K.J., Radhakrishnan K. and Mast T.D. (2014). Frequency-sum passive cavitation imaging. *The Journal of the Acoustical Society of America*, **135**(4), pp. 2310–2310.

Haworth K.J., Raymond J.L., Radhakrishnan K., Moody M.R., Huang S.L., Peng T., Shekhar H., Klegerman M.E., Kim H., McPherson D.D. et al. (2016b). Transstent b-mode ultrasound and passive cavitation imaging. *Ultrasound in medicine & biology*, **42**(2), pp. 518–527.

Haworth K.J., Salgaonkar V.A., Corregan N.M., Holland C.K. and Mast T.D. (2015). Using passive cavitation images to classify high-intensity focused ultrasound lesions. *Ultrasound in medicine & biology*, **41**(9), pp. 2420–2434.

Jensen C.R., Ritchie R.W., Gyöngy M., Collin J.R., Leslie T. and Coussios C.C. (2012). Spatiotemporal monitoring of high-intensity focused ultrasound therapy with passive acoustic mapping. *Radiology*, **262**(1), pp. 252–261.

Johansen K., Song J.H. and Prentice P. (2018). Performance characterisation of a passive cavitation detector optimised for subharmonic periodic shock waves from acoustic cavitation in mhz and sub-mhz ultrasound. *Ultrasonics sonochemistry*, **43**, pp. 146–155.

Kamimura H.A., Wu S.Y., Grondin J., Ji R., Aurup C., Zheng W., Heidmann M., Pouliopoulos A.N. and Konofagou E.E. (2020). Real-time passive acoustic mapping using sparse matrix multiplication. *IEEE Transactions on Ultrasonics, Ferroelectrics, and Frequency Control*, **68**(1), pp. 164–177.

Kennedy J., Wu F., Ter Haar G., Gleeson F., Phillips R., Middleton M. and Cranston D. (2004). High-intensity focused ultrasound for the treatment of liver tumours. *Ultrasonics*, **42**(1-9), pp. 931–935.

Khokhlova T.D., Canney M.S., Khokhlova V.A., Sapozhnikov O.A., Crum L.A. and Bailey M.R. (2011). Controlled tissue emulsification produced by high intensity focused ultrasound shock waves and millisecond boiling. *The Journal of the Acoustical Society of America*, **130**(5), pp. 3498–3510.

Köhler M.O., Mougenot C., Quesson B., Enholm J., Le Bail B., Laurent C., Moonen C.T. and Ehnholm G.J. (2009). Volumetric hifu ablation under 3d guidance of rapid mri thermometry. *Medical physics*, **36**(8), pp. 3521–3535.

Kwan J.J., Myers R., Coviello C.M., Graham S.M., Shah A.R., Stride E., Carlisle R.C. and Coussios C.C. (2015). Ultrasound-propelled nanocups for drug delivery. *Small*, **11**(39), pp. 5305–5314.

Li J., Stoica P. and Wang Z. (2003). On robust capon beamforming and diagonal loading. *IEEE transactions on signal processing*, **51**(7), pp. 1702–1715.

Li M., Lan B., Sankin G., Zhou Y., Liu W., Xia J., Wang D., Trahey G., Zhong P. and Yao J. (2019). Simultaneous photoacoustic imaging and cavitation mapping

in shockwave lithotripsy. *IEEE transactions on medical imaging*, **39**(2), pp. 468–477.

Li T., Chen H., Khokhlova T., Wang Y.N., Kreider W., He X. and Hwang J.H. (2014). Passive cavitation detection during pulsed hifu exposures of ex vivo tissues and in vivo mouse pancreatic tumors. *Ultrasound in medicine & biology*, **40**(7), pp. 1523–1534.

Lu S., Hu H., Yu X., Long J., Jing B., Zong Y. and Wan M. (2018). Passive acoustic mapping of cavitation using eigenspace-based robust capon beamformer in ultrasound therapy. *Ultrasonics sonochemistry*, **41**, pp. 670–679.

Lyka E., Coviello C., Kozick R. and Coussios C.C. (2016). Sum-of-harmonics method for improved narrowband and broadband signal quantification during passive monitoring of ultrasound therapies. *The Journal of the Acoustical Society of America*, **140**(1), pp. 741–754.

Lyka E., Coviello C.M., Paverd C., Gray M.D. and Coussios C.C. (2018). Passive acoustic mapping using data-adaptive beamforming based on higher order statistics. *IEEE transactions on medical imaging*, **37**(12), pp. 2582–2592.

McLaughlan J., Cowell D. and Freear S. (2017). Gold nanoparticle nucleated cavitation for enhanced high intensity focused ultrasound therapy. *Physics in Medicine & Biology*, **63**(1), p. 015004.

McLaughlan J., Rivens I., Leighton T. and ter Haar G. (2010). A study of bubble activity generated in ex vivo tissue by high intensity focused ultrasound. *Ultrasound in medicine & biology*, **36**(8), pp. 1327–1344.

McLaughlan J.R. (2008). *An investigation into the use of cavitation for the optimisation of high intensity focused ultrasound (HIFU) treatments*. Ph.D. thesis, Institute of Cancer Research (University Of London).

McLaughlan J.R. (2018). Controllable nucleation of cavitation from plasmonic gold nanoparticles for enhancing high intensity focused ultrasound applications. *JoVE (Journal of Visualized Experiments)*, (140), p. e58045.

Montaldo G., Tanter M., Bercoff J., Benech N. and Fink M. (2009). Coherent plane-wave compounding for very high frame rate ultrasonography and transient

elastography. *IEEE transactions on ultrasonics, ferroelectrics, and frequency control*, **56**(3), pp. 489–506.

Neppiras E. (1969). Subharmonic and other low-frequency emission from bubbles in sound-irradiated liquids. *The Journal of the Acoustical Society of America*, **46**(3B), pp. 587–601.

Nilsen C.I.C. and Holm S. (2010). Wiener beamforming and the coherence factor in ultrasound imaging. *IEEE transactions on ultrasonics, ferroelectrics, and frequency control*, **57**(6), pp. 1329–1346.

Norton S.J., Carr B.J. and Witten A.J. (2006). Passive imaging of underground acoustic sources. *The Journal of the Acoustical Society of America*, **119**(5), pp. 2840–2847.

Norton S.J. and Won I. (2000). Time exposure acoustics. *IEEE Transactions on Geoscience and Remote Sensing*, **38**(3), pp. 1337–1343.

Nyborg W.L. and Ziskin M.C. (1985). Biological effects of ultrasound.

O'Reilly M.A., Jones R.M. and Hynynen K. (2014). Three-dimensional transcranial ultrasound imaging of microbubble clouds using a sparse hemispherical array. *IEEE Transactions on Biomedical Engineering*, **61**(4), pp. 1285–1294.

Polichetti M., Varray F., Gilles B., Béra J.C. and Nicolas B. (2020). Use of the cross-spectral density matrix for enhanced passive ultrasound imaging of cavitation. *IEEE Transactions on Ultrasonics, Ferroelectrics, and Frequency Control*, **68**(4), pp. 910–925.

Rabkin B.A., Zderic V. and Vaezy S. (2005). Hyperecho in ultrasound images of hifu therapy: involvement of cavitation. *Ultrasound in medicine & biology*, **31**(7), pp. 947–956.

Salgaonkar V.A., Datta S., Holland C.K. and Mast T.D. (2009). Passive cavitation imaging with ultrasound arrays. *The Journal of the Acoustical Society of America*, **126**(6), pp. 3071–3083.

Shaw A., Martin E., Haller J. and ter Haar G. (2016). Equipment, measurement and dose—a survey for therapeutic ultrasound. *Journal of Therapeutic Ultrasound*, **4**(1), p. 7.

Stanziola A., Leow C.H., Bazigou E., Weinberg P.D. and Tang M.X. (2018). Asap: Super-contrast vasculature imaging using coherence analysis and high frame-rate contrast enhanced ultrasound. *IEEE transactions on medical imaging*, **37**(8), pp. 1847–1856.

Stoica P., Wang Z. and Li J. (2002). Robust capon beamforming. In: *Conference Record of the Thirty-Sixth Asilomar Conference on Signals, Systems and Computers, 2002.*, vol. 1. IEEE, pp. 876–880.

Ter Haar G. (1995). Ultrasound focal beam surgery. *Ultrasound in medicine & biology*, **21**(9), pp. 1089–1100.

Wu F., Wang Z.B., Chen W.Z., Bai J., Zhu H. and Qiao T.Y. (2003). Preliminary experience using high intensity focused ultrasound for the treatment of patients with advanced stage renal malignancy. *The Journal of urology*, **170**(6), pp. 2237–2240.

Zeng X., Chen C. and Wang Y. (2012). Eigenspace-based minimum variance beamformer combined with wiener postfilter for medical ultrasound imaging. *Ultrasonics*, **52**(8), pp. 996–1004.

Chapter 4

Dynamic F-number and shading weights determined by element directivity for PAM

Among types of relative time-flight beamformers (BF) (i.e. data-independent and adaptive BFs), the conventional BFs, such as time exposure acoustics (TEA) based techniques for passive acoustic mapping (PAM), demonstrate that their implementation can be simplified by sparse-matrix, GPU-running, etc., methods Kamimura et al. (2020), and therefore compatible with real-time monitoring. General assumptions for the derivation of TEA-based PAM are: the employment of pixewise shading weight is approximated by linear assumption Wettergren (2004), and the acoustic emissions are received omnidirectionally with whole aperture Friis and Feldman (1937). The consequent concerns about the general assumptions: the linear assumed weight are always not efficiently for clutter suppression and the whole aperture data can contribute to the generation of side lobes to degrade the image quality. To address the aforementioned, a strategy was proposed based on a soft-baffle Element Directivity (ED) model (related to the conformal nature of the receiving array) for Dynamic F-number and Shading Weight (DFSW) to maintain and shape the top hyperbola part of the realigned receiving wavefront, and then apply into TEA and coherent TEA (CTEA) BF, due to their potential real-time feasibility. Final results from TEA and proposed methods (ED TEA, ED CTEA) demonstrate that the DFSW strategy developed from ED is more efficient on the image quality improvement (FWHM, CNR) of near-field, which is explained and verified by simulated and experimental data.

4.1 Introduction

TEA-based PAM is with computation simplicity among relative time-flight BFs due to its weighting vectors are data-independent. However, the presence of the grating or side lobes limits the output performance of conventional BFs. Adaptive methods could mitigate these issues but are impractical due to the exponentially increased computation cost and can suffer the loss of the statistical properties of the original data phase information Destrempes and Cloutier (2010); Salles et al. (2014). To reduce the side lobes and ambient noise clutters for conventional BFs without gaining the computation complexity, more concerns were raised to the conformal nature of the array by appealing the receiving goal beam-pattern yield to the array response.

The ED is one of the important array characteristics that is determined by the geometry of constituent elements and the wavelength of the acoustic wave in the propagating medium Selfridge et al. (1980). When the element size is comparable to the wavelength of the interrogating wave, the impact of ED will play an important role on the wave field generation and reception Tasinkevych et al. (2013, 2012). Aspects of techniques considering ED have been investigated in the context of radar and active acoustic fields Pompei and Wooh (2002); Skobelev (1998); Tasinkevych et al. (2013, 2012), but not too much attention has been paid to PAM in the area of cavitation monitoring.

Inspired by the aforementioned, a soft-baffle ED model, proposed in this chapter for TEA-derived PAM algorithms aims to provide a strategy of pixelwise F-number and shading weight to apodize the RF data acquired from the dynamic aperture size, finally, to improve PAM image resolution and contrast. This chapter is organised as follows. In section 4.2, the numerical data is presented, which was simulated via point spread function (PSF) (or termed as bubble scatterer/source) located at fixed sites and PSFs in bubble-cluster format randomly located within circle areas at different depths, respectively. Each PSF was simulated via coated-bubble model with radius ranging randomly within $1.25 \pm 0.2\ \mu m$ and stimulated by 30 cycles ultrasound wave with 3.3 MHz and ambient pressure of 3 MPa. The simulation was set with the same datasets in experimental data that repeated on *ex vivo* bovine liver tissues. A brief introduction is provided about TEA, ED TEA and ED CTEA algorithms combing with DFSW strategy. In sections 4.3 and 4.4, final PAM results from simulation and experiments are illustrated and discussed at near and distal fields, and the conclusion of this work is summarised in section

4.5.

4.2 Methods

4.2.1 Simulation

The simulated acoustic emissions from a single bubble or cluster-format bubbles which can be expressed by:

$$\boldsymbol{P}_{total} = \sum_{m=1}^{M} \boldsymbol{S}_m(t) * \boldsymbol{Tr}_m(t) * \boldsymbol{P}_m(t) + \boldsymbol{q}. \tag{4.1}$$

The $\boldsymbol{P}_{total}$ represents the total bubble pressure output with array response for passive received energy estimation and beamforming. $*$ is the convolution operator. M is the total number of simulated bubble sources. $\boldsymbol{S}(t)$ is the spatial response for propagation path, it is assumed that the propagation travelled in the ideal environment without attenuation, phase aberration, etc., factors, and is illustrated as $\boldsymbol{\delta}(t)$ (i.e., the identity matrix). $\boldsymbol{q}$ is for the additive random noise.

The $\boldsymbol{Tr}(t)$ is the spatial response with element sensitivity from the conformal transducer, which is approximated by the Fresnel-Kirchhoff diffraction formula Lu et al. (1994); Mast (2007). Basic principles about the analysing of diffraction pattern was originated in optics Huggins (2007), and now have been introduced into ultrasound to predict the pressure or velocity response at any spatial point that generate by a finite aperture Lu et al. (1994).

The $\boldsymbol{P}(t)$ is the pressure wave field from a single bubble source or multi-bubble sources. The $\boldsymbol{P}(t)$ from a single bubble source is simulated via coated-bubble model with non-linear propagation characters Morgan et al. (2000). For the bubble-cluster simulation, the pressure field from multi-bubble sources (i.e., each one simulated via coated-bubble model) is located at different random sites that are linearly added together to form the final output.

The coated-bubble model used for the simulation of each bubble source is based on the modified Herring equation, which can be expressed as:

$$\begin{aligned}\rho R\ddot{R} + \frac{3}{2}\rho\dot{R}^2 = \left(P_0 + \frac{2\sigma}{R_0} + \frac{2\chi}{R_0}\right)\left(\frac{2R_0}{R}\right)^{3\gamma}\left(1 - \frac{3\gamma}{c}\dot{R}\right) - \frac{4\mu\dot{R}}{R} - \frac{2\delta}{R}\left(1 - \frac{1}{c}\dot{R}\right) \\ - \frac{2\chi}{R}\left(\frac{R_0}{R}\right)^2\left(1 - \frac{3}{c}\dot{R}\right) - 12\mu_{sh}\xi\frac{\dot{R}}{R(R-\xi)} - (P_0 + P_{driv}(t)),\end{aligned} \tag{4.2}$$

Symbol/Unit	Physical meaning	Number
$c/m.s^{-1}$	Speed of sound	1480
$\rho/kg.m^{-3}$	Liquid density	998
P_0/KPa	Hydrostatic pressure	101
$\delta/N.m^{-1}$	Interfacial tension coefficient	0.051
γ	Polytropic gas exponent	1.07
$\mu/Pa.s$	Viscosity	0.001
$\mu_{sh}/Pa.s$	Viscosity of lipid shell	2.865
ε/nm	Thickness of lipid shell	1
$\chi/N.m^{-1}$	Elasticity modulus of lipid shell	0.26
$R_0/\mu m$	Initial bubble radius	1.25 $\mu m \pm$ 0.2

Table 4.1: Parameters for coated-bubble model

The coated-bubble model was solved by fourth-order Runge-Kutta algorithm via ode45 function with an absolute tolerance of $1e-11$ in MATLAB, then the bubble dynamic results, including the instantaneous bubble radius R, wall velocity of bubble $\dot{R}$ and acceleration of bubble wall $\ddot{R}$, were calculated into the predicted echo wave Morgan et al. (2000); Versluis et al. (2020):

$$\mathrm{P} = \rho \mathrm{r}^{-1}\left(\mathrm{R}^2\ddot{\mathrm{R}} + \mathrm{R}\dot{\mathrm{R}}^2\right). \tag{4.3}$$

r is distance from the bubble center equals for the predicted scattered pressure wave P. The related parameters about coated-bubble model are illustrated in Table 4.1, and the specification of parameters' settings can be reviewed in Greis (2004); Haynes et al. (2016); Morgan et al. (2000).

A bubble-cluster simulation was presented for the illustration of equation 4.1. Twenty bubble sources were randomly distributed in the circle with 2 mm radius and centre located at (0, 26)mm. Each bubble was simulated by coated-bubble model (e.g. parameters are shown in Table 4.1), and the cluster was set to be driven by a 30 cycle ultrasound wave $\mathrm{P}_{\mathrm{driv}}(\mathrm{t})$ at a frequency of 3.3 MHz and the ambient pressure of 3 MPa. The initial bubble radius was Gaussian distributed within $1.25\mu m \pm 0.2$.

Figure 4.1 illustrates the random location of bubble sources (a) and its radius distribution following a Gaussian pattern (b). Figure 4.2 shows one single bubble source located at (-0.189, 24.7)mm in Figure 4.1 that was taken randomly as

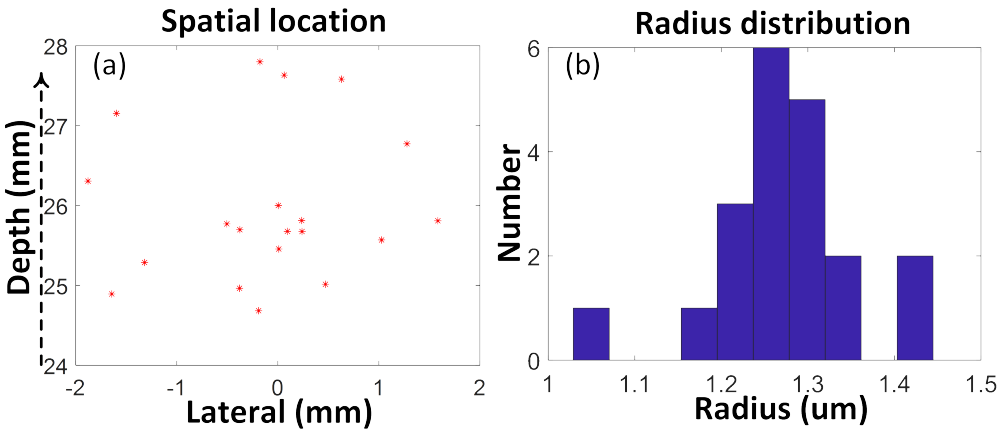

Figure 4.1: Coated-bubble model simulating the bubble-cluster. (a) The random spatial distribution of 20 bubble sources. (b) The Gaussian distributed bubble radii of 20 bubble sources.

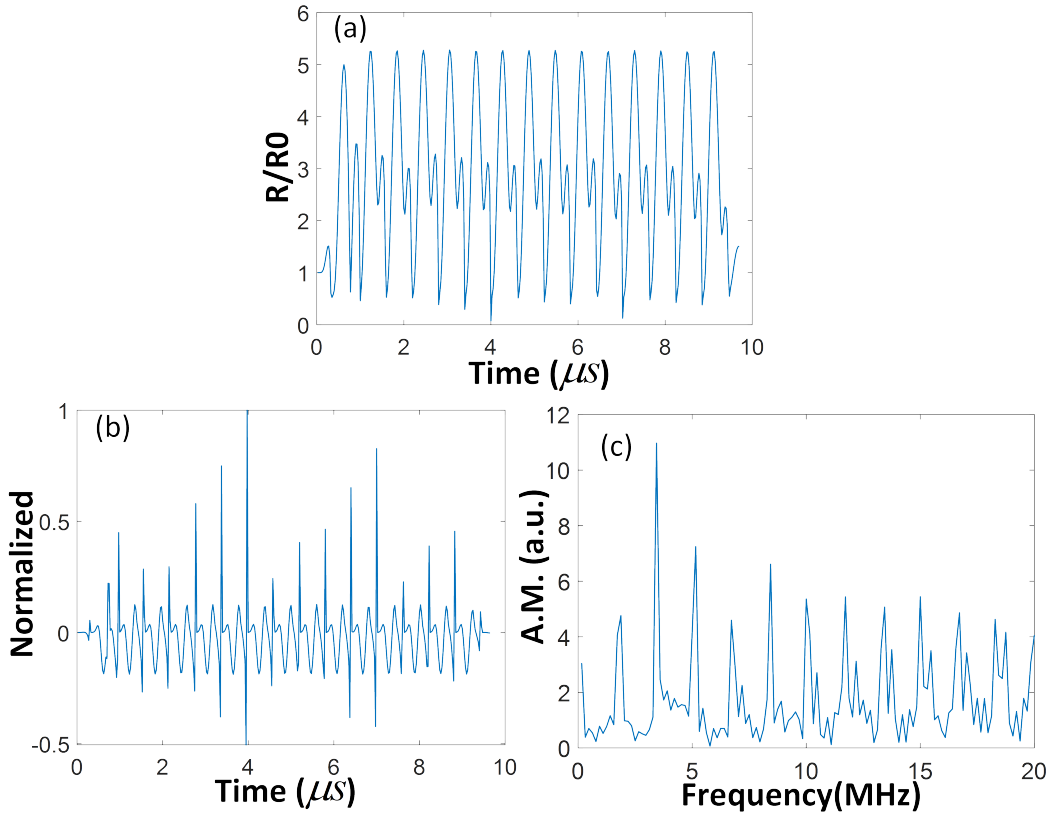

Figure 4.2: Simulated single bubble dynamics with radius 1.25μm at (-0.189, 24.7) in Figure 4.1. (a) Instantaneous bubble radius. (b) Normalised predicated scattered pulse. (c) The frequency spectrum of the predicated scattered pulse.

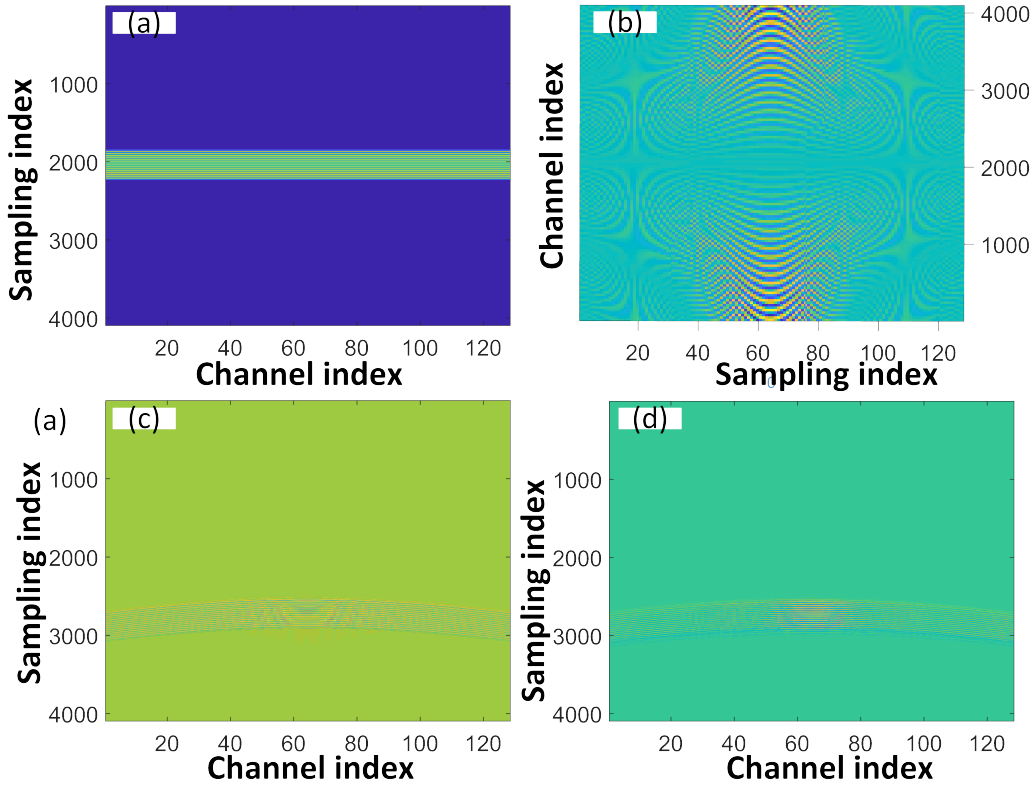

Figure 4.3: The illustration of equation 4.1. (a) Single bubble simulated pressure wave located at (-0.189, 24.7)mm in Figure 4.1. (b) The transducer response for the single bubble located at (-0.189, 24.7)mm. (c) RF data of single bubble at (-0.189, 24.7)mm for receiving. (d) The RF data of 20 bubble sources for final output.

an example to show the bubble dynamics simulated by the coated-bubble model. Figure 4.2(a) is the instantaneous bubble radius ratio (R/R_0, non-dimensional), Figure 4.2(b) indicates the scattered pulse P with normalised amplitude (non-dimensional) and Figure 4.2(c) is the Fourier frequency transformation of the normalised P and displayed with arbitrary unit. Due to the frequency response of each element in the imaging array, the signal will be recorded within the available bandwidth. To achieve that, a bandpass filter with corresponding bandwidth would generally be applied to pre-filter the received emissions. However, this process can cause the cavitation energy loss due to the removal of frequency components outsides the bandwidth of the imaging array, while, with levels of spectral leakage (i.e., filtering techniques in MATLAB can generate the phenomenon of residual (low-amplitude) lobes damping outside the interested frequency bandwidth which termed as spectral leakage) results in the cavitation energy mis-interpretation. Hence, all frequency components of the normalised P are maintained to simulate the case of infinite bandwidth (not achievable in reality), which allows the pressure-to-voltage signal relationship to be identical to 1 for all frequencies Lyka (2016). In Figure 4.3, the data acquisition duration and sampling rate were set as 30 μm and 40 MHz, respectively. Figure 4.3(a) is the passive received emissions of $\boldsymbol{P}(t)$ generated from the single bubble located at (-0.189, 24.7)mm. The point source was assumed to be generated by the predicted scatter pulse P with isotropic nature via an omnidirection, and being received identically by each channel with a set depth to form the matrix format of $\boldsymbol{P}(t)$. Figure 4.3(b) shows the imaging array response of $\boldsymbol{Tr}(t)$ estimated by by the Fresnel-Kirchhoff diffraction, and facilitating the phase information for the received emissions $\boldsymbol{P}(t)$. The convolution operation calculated between $\boldsymbol{P}(t)$ and $\boldsymbol{Tr}(t)$ generated the results in Figure 4.3(c) for RF data of the single point source to be received by the imaging array. Finally, following the above procedures, the RF data of 20 randomly distributed point sources are generated separately, and being linearly summed together as shown in Figure 4.3(d).

4.2.2 Element Directivity for DFSW

Side lobes increase and spread out in PAM which diminishes the contrast of the cavitation monitoring on the image. The presence of the side lobe as ambient clutters or axial tails commonly has relatively small amplitudes outside the location of cavitation regions and existing over a long time Jeong and Choi (2022). Possible

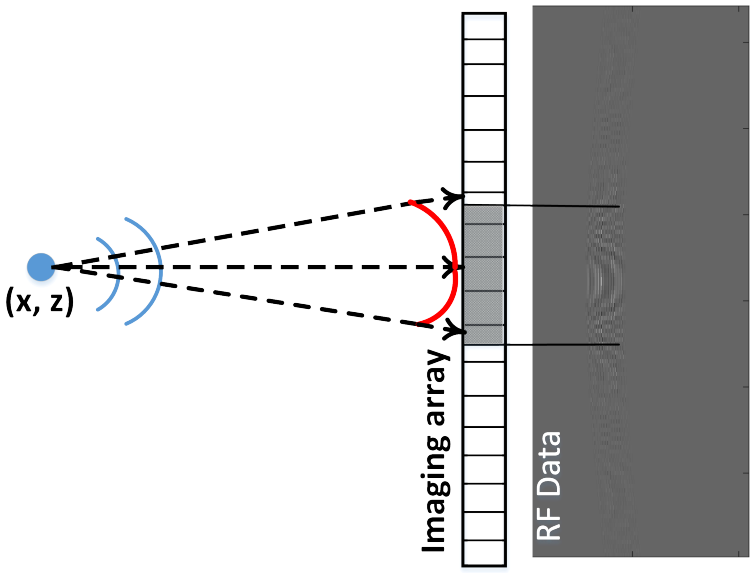

Figure 4.4: The acoustic pulse emitted from pixel (x, z) and the red part indicates the main lobe (or top part of the hyperbolic signature) received by an available aperture.

ways related to beamforming process to mitigate the impacts of side lobes with time efficiency, which can be achieved by selecting the interested cavitation duration for integration due to the main lobe always emerges with a short time. Another suggested way is only to beamform the data received by an available pixelwise aperture within the top part of the hyperbolic signature (i.e. the red part in Figure 4.4), so that the bias-variance trade-off can be optimised when summing the signals along the hyperbolas to improve the image quality Perrot et al. (2021).

The implementation of the DSFW strategy is developed based on the element directivity which governs the signal amplitude along the hyperbolas with the aim to identify the pixelwise aperture and reduce the side lobes. Specifically, the scattered emissions are isotropic while the elements are indeed not omnidirectional, as a result, the emissions are not received uniformly in all directions Perrot et al. (2021). A modified ED model Li et al. (2020a); Selfridge et al. (1980) was presented to maintain the top hyperbolas part as the main lobes within its available aperture sizes for beamforming and to illustrate its relationship with F-number.

The ED for element n located at $(x_n, 0)$ can be expressed as:

$$A(\theta_n) = \begin{cases} 1, & \theta_n = 0 \\ \dfrac{\sin\left(\pi \times {}^{w}/_{l} \times \sin(\theta_n)\right)}{\pi \times {}^{w}/_{l} \times \sin(\theta_n)} \cos(\theta_n), & Otherwise \end{cases} \tag{4.4}$$

The θ_n term in equation 4.4 can be expressed as per equation 4.5, where w is the width of each array element, and l is the ultrasound wavelength in the medium.

$$\theta_n = \tan^{-1}\left(\frac{x - x_n}{z}\right). \tag{4.5}$$

The element pitch of the linear array is 0.3 mm, but the width of each transducer element is unknown. Therefore, the element width was assumed to be 0.25 mm for the simulated and experimental data. The ultrasound wavelength l defined in both simulation and experiments was $\frac{c}{3.3\text{MHz}} = 0.449\mu m$, and c is the speed of sound 1480 m/s. Figure 4.5 illustrates the ED values for all the receiving elements that varied with depth. As a result, when the emission depth is shallow, the ED at pixel (0, 1)mm has high directivity, which indicates the imaging array predominantly receives emissions in front of it with a narrow field of view. With increasing depth, for the BF pixels at (0, 20)mm, (0, 40)mm, respectively, the ED turns more becomes omnidirectional which presents the emissions can be received with more apertures gradually.

For the consideration of image quality (i.e., contrast to noise ratio and lateral resolution), an available aperture was selected based on the normalised $A(\theta_n)$ to discard its amplitudes below values of –3dB (approximately 0.7), –6dB (approximately 0.5) and –20dB (approximately 0.1) (i.e., options for the discarding threshold), and the schematic of discarding implementation is shown in Figure 4.6. Therefore, a dynamic aperture size for each BF pixel was proposed for received beamforming. The F-number is the ratio between the pixel depth z and the width of the available aperture diameter, which for imaging is generally set as a constant, such as 2 Li et al. (2004). The proposed dynamic aperture size updates the F-number from a constant number to be varied with ED for each beaformed pixel.

Incorporating a dynamic F-number into the conventional TEA, ED TEA and ED CTEA beamformers at pixel (x_0, z_0) can be expressed as:

$$I_{\text{ED TEA}}(x_0, z_0) = \int_{t_0}^{t_0+T} \left[\sum_{n=i}^{q} \mathbf{w}\, s_n(x_0, z_0, t)\right]^2 dt. \tag{4.6}$$

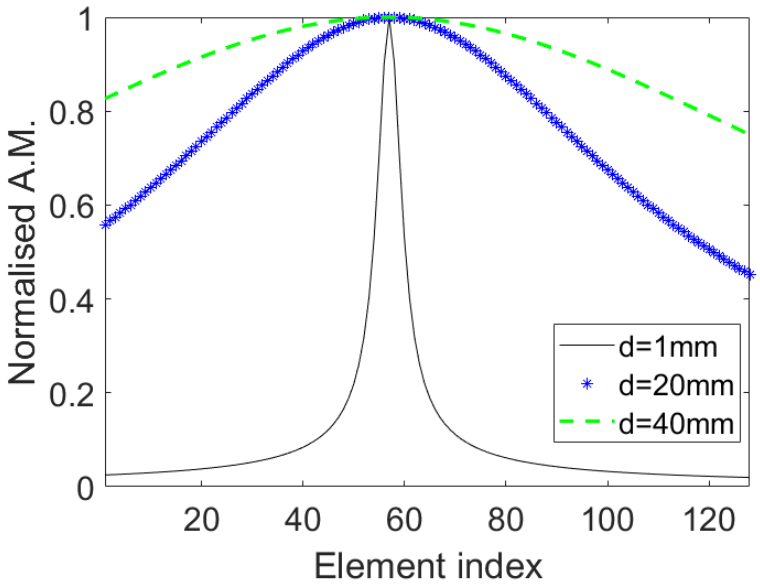

Figure 4.5: The ED values for all receiving elements at BF pixel (0, 1)mm, (0, 20)mm, (0, 40)mm, respectively.

$$I_{\text{ED CTEA}}(x_0, z_0) = \int_{t_0}^{t_0+T} \left(\left[\sum_{n=i}^{q} \mathbf{w}\ sign(s_n(x_0, z_0, t))\ \sqrt{|s_n(x_0, z_0, t|} \right]^2 - \sum_{n=i}^{q} \left[\mathbf{w}\ sign(s_n(x_0, z_0, t))\ \sqrt{|s_n(x_0, z_0, t|} \right]^2 \right) dt. \tag{4.7}$$

With i and q are subjected to $\frac{z_0}{x_i - x_q} = F_{num}$ (i.e. related to the final selected discarding threshold following the schematic shown in Figure 4.6), where i indicates the starter element index of available aperture size, and q is the final element index of available aperture size. The **w** represents the shading weight which can be illustrated as:

$$\mathbf{w} = \frac{A(\theta_n)}{max(A(\theta_n))}, \quad n = i : q \tag{4.8}$$

The $s_n(x_0, z_0, t)$ is the experimental or simulated RF data being spatially aligned, t is the relative time delay, and T is the integration time for each image.

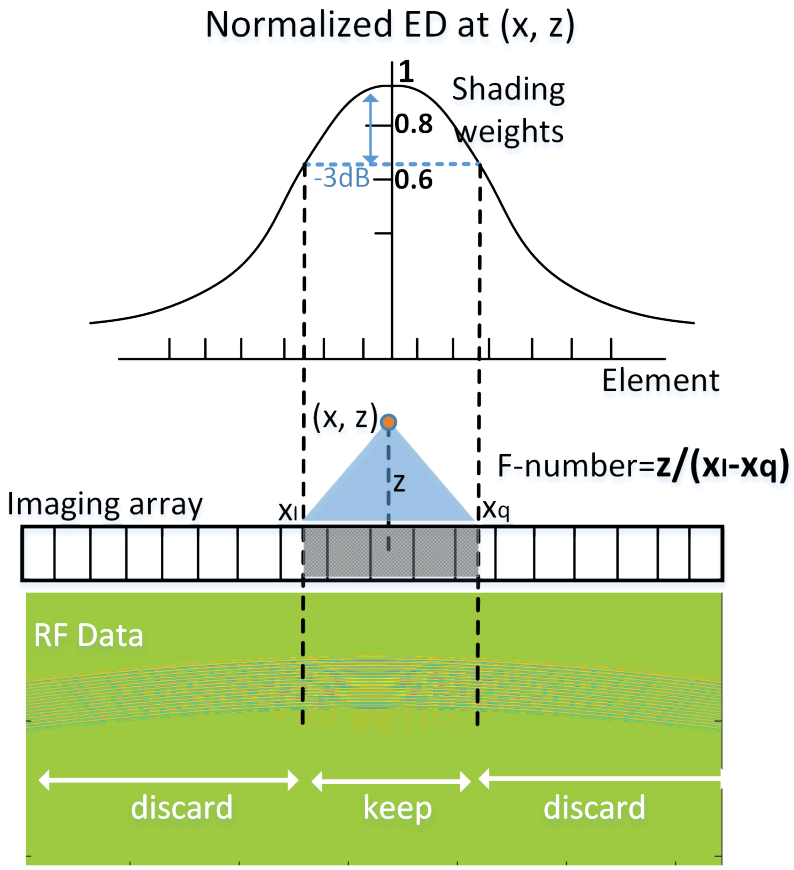

Figure 4.6: The schematic implementation of DFSW strategy into beamforming for pixels located at (x, z), when the threshold was selected as –3dB, as an example.

4.2.3 *Ex vivo* Experiments

The HIFU experiment was performed in *ex vivo* bovine liver tissue with 5 seconds exposure, centre frequency 3.3 MHz and peak negative pressure of 3 MPa. The RF data was stored in the house-developed Ultrasound Array Research Platform (UARP) Cowell et al. (2013); Smith et al. (2013, 2012) with 40 MHz sampling frequency for post processing. More details about the acquisition of PAM experimental data from the perpendicular setting system is presented in section 3.2.3.

4.3 Results

In this chapter, the simulation data was used to verify the influence of an ED-based DFSW strategy on targets at different depths beamformed by TEA, ED TEA and ED CTEA. For both the simulated and experimental datasets, all frequency components are used for beamforming and each of their integration time T was $15\mu s$ (e.g., simulated data) and $40\mu s$ (e.g., experimental data), respectively. The axial beamforming step is 1 mm, and the lateral beamforming step was set to the pitch size of the transducer, 0.3 mm.

The selection of discarding threshold

Figure 4.7 illustrates the spatial location of three simulated bubble scatterers located at (0, 5)mm, (0, 15)mm and (0, 30)mm with different depth, respectively. Each point scatterer was simulated by coated-bubble model with initial bubble radius at $1.25\mu m$. The red and black rectangular areas indicate the pixel intensity calculation of the signal area and noise area for contrast to noise ratio (CNR) calculation. Figure 4.8 is the simulated RF data beamformed by TEA with different discarding thresholds 0.1 (a), 0.5 (b) and 0.7 (c) for the implementation of ED-based DFSW strategy. The clutter was visually more mitigated for the point scatterer at near-field (0, 5)mm with the CNR increased from approximately 25.1dB (a) to 30.3dB (c). A compromise needs to be made between clutter alleviation and possible signal over-suppression, with the chosen discarding threshold getting higher (from 0.1 to 0.7). As the results shown in Figure 4.9, the point scatterer at (0, 5)mm can not be displayed from the contour map when the thresholds are 0.5 and 0.7, which indicates the possible occurrence of an over-suppression situation. Therefore, the discarding threshold for ED-based DFSW strategy was set as 0.1 for ED TEA and ED CTEA.

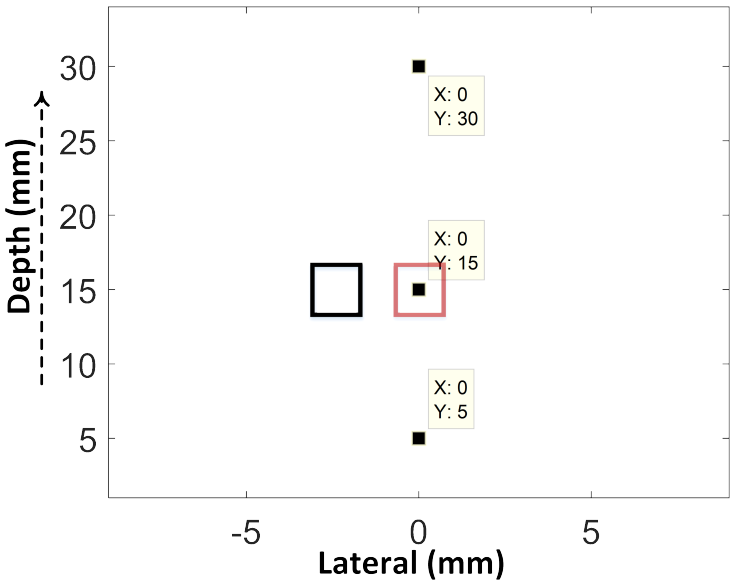

Figure 4.7: The spatial locations of three different simulated bubbles. The rectangular areas indicate the CNR calculation.

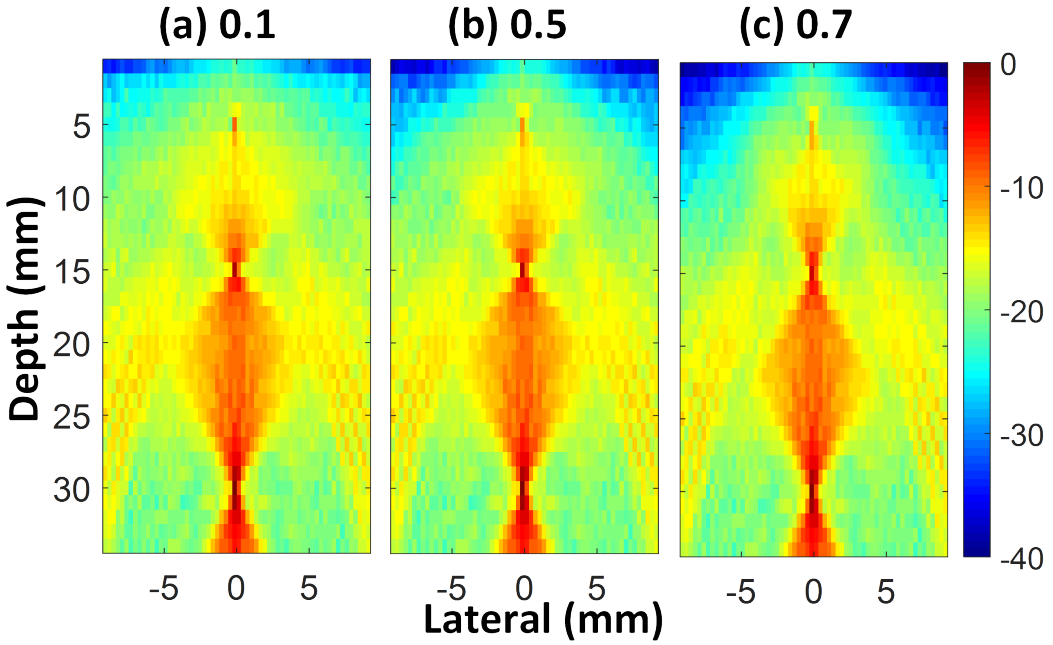

Figure 4.8: The simulated bubbles beamformed by ED TEA with different discarding thresholds of 0.1 (a), 0.5 (b) and 0.7 (c).

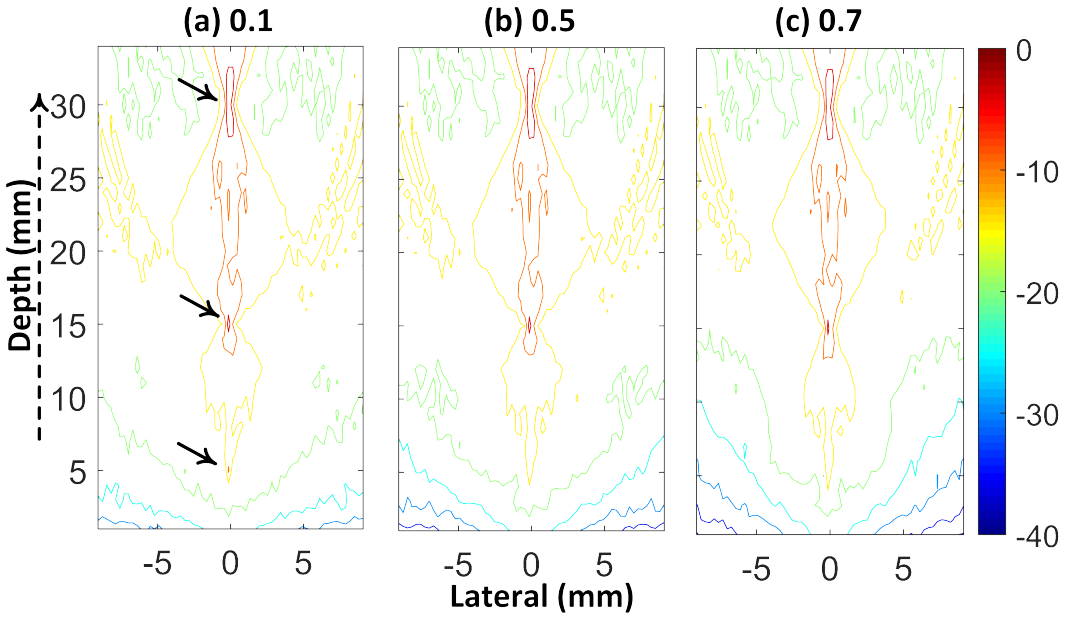

Figure 4.9: The contour displaying of the simulated bubbles (Figure 4.8).

Beamforming performance: simulation and experiments

Figure 4.10 is the simulated point scatterers at different depths beamformed by TEA (a), ED TEA (b) and ED CTEA (c). TEA compared with ED TEA, which can be understood as using the full aperture RF data for beamforming without considering the dynamic F-number (i.e., discarding threshold) and the shading weight **w**. The 'X type' side lobes at (0, 5)mm and the residual clutters around (0, 20)mm in Figure 4.10(b) were clearly suppressed compared with 4.10(a). The CNR and lateral resolution of ED TEA at proximal (i.e., 5, 15mm) were improved relative to the TEA beamformer, as shown in Table 4.2, and the metrics of simulated bubble at distal (i.e. 30mm) maintain nearly the same level. Moreover, the ED CTEA shows a prominent performance among all beamformers due to the contribution from the ED-based DFSW strategy and coherent calculation.

The bubble-cluster simulation was performed within two circle areas wherein each circle radius is 2mm and centre locations are (-2, 10)mm and (2, 30)mm, respectively. Twenty bubbles were randomly distributed inside each circle area, and their initial bubble radius were Gaussian distributed within $1.25 \pm 0.2 \mu m$, the details of which are shown in Figure 4.11. Figure 4.12 is the simulated bubble-clusters beamformed by TEA (a), ED TEA (b) and ED CTEA (c). The metrics illustrated in Table 4.3 show that CNR and resolution of ED TEA at depth 10mm

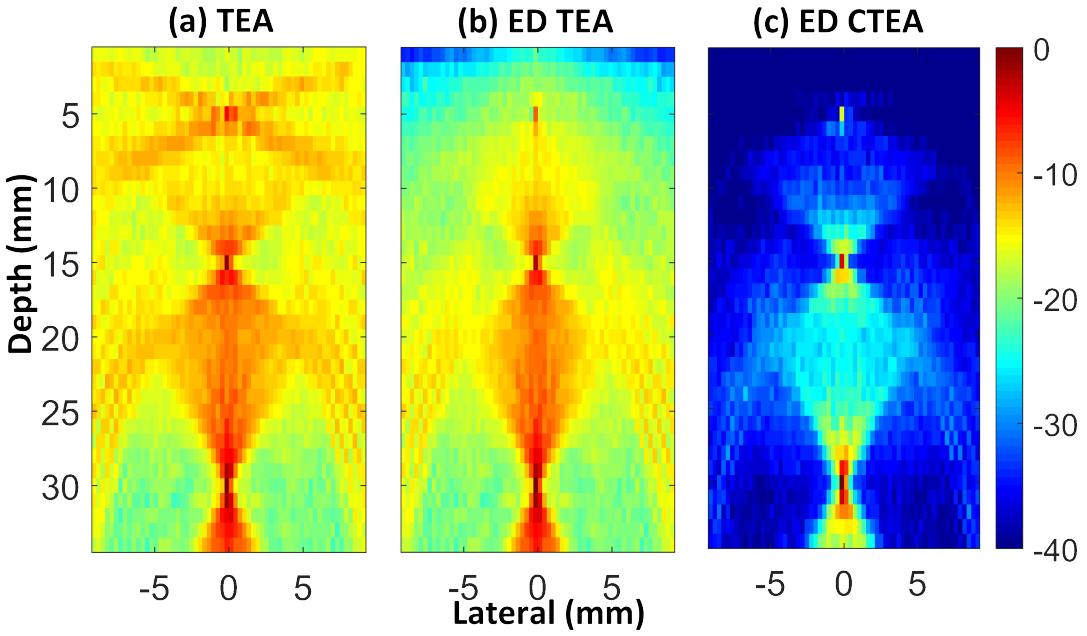

Figure 4.10: The simulated bubbles beamformed by TEA (a), ED TEA (b), ED CTEA (c).

	Depth	TEA	ED TEA	ED CTEA
Reso(mm)	(0, 5)mm	1.76	0.56	0.31
	(0, 15)mm	0.67	0.52	0.39
	(0, 30)mm	0.57	0.56	0.40
CNR(dB)	(0, 5)mm	21.7	25.1	51
	(0, 15)mm	30	31.6	62.5
	(0, 30)mm	40	40.1	74.3

[a] Reso indicates for resolution which was calculated by Full width at half-maximum -6dB.

Table 4.2: CNR and lateral resolution of simulated bubbles.

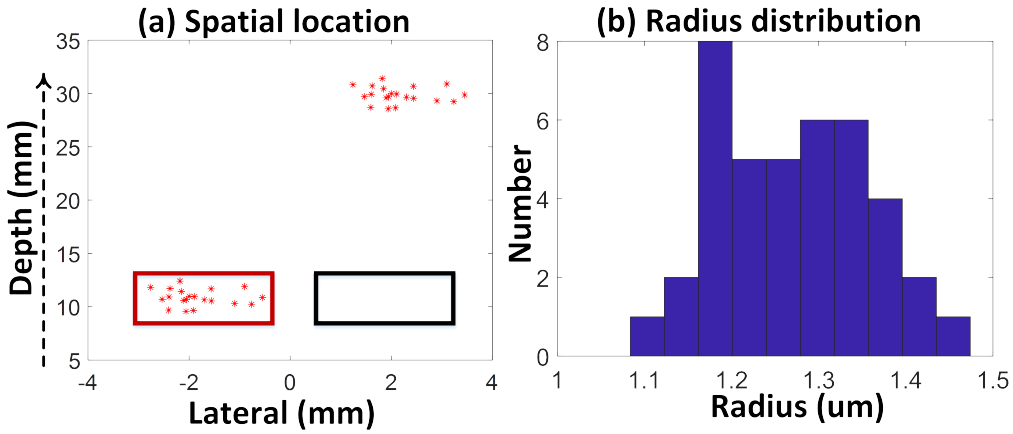

Figure 4.11: The simulated bubble-clusters randomly located inside two circle areas (a) and two 20 bubble radius distributions (b). The rectangular areas are the CNR calculations.

were improved 4dB and 0.7mm, respectively, relative to TEA, and the performance of bubble-clusters at depth 30mm was almost the same, which concedes to the results shown in Figure 4.10. The output from ED CTEA again demonstrates its superiority on the CNR and resolution of the overall image. The outputs beamformed by experimental data shown in Figure 4.13 illustrate a consistent trend with the simulated results that the ED-based DFSW strategy does not play a significant role in image quality when the depth becomes deeper. Besides the improvements in ED CTEA, the final performance of suspected cavitation cluster located approximately at depth 31mm that were beamformed by TEA and ED TEA are almost identical to each other.

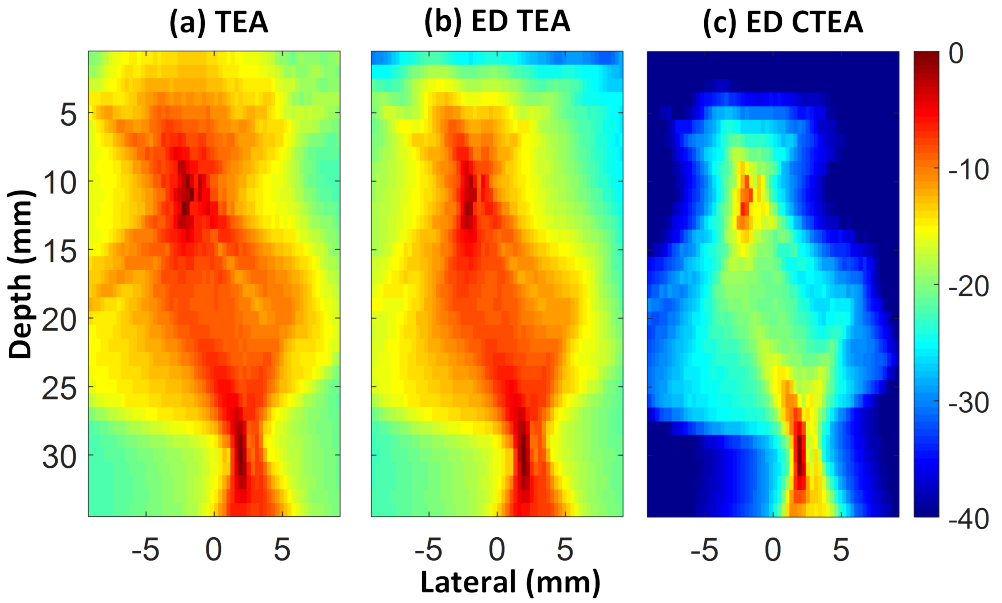

Figure 4.12: The simulated bubble-clusters beamformed by TEA (a), ED TEA (b), ED CTEA (c).

	Depth	TEA	ED TEA	ED CTEA
Reso(mm)	(0, 10)mm	1.90	1.20	0.31
	(0, 30)mm	2.00	2.10	1.20
CNR(dB)	(0, 10)mm	30.1	34	51
	(0, 30)mm	39	40	60

Table 4.3: CNR and lateral resolution of simulated bubble-clusters.

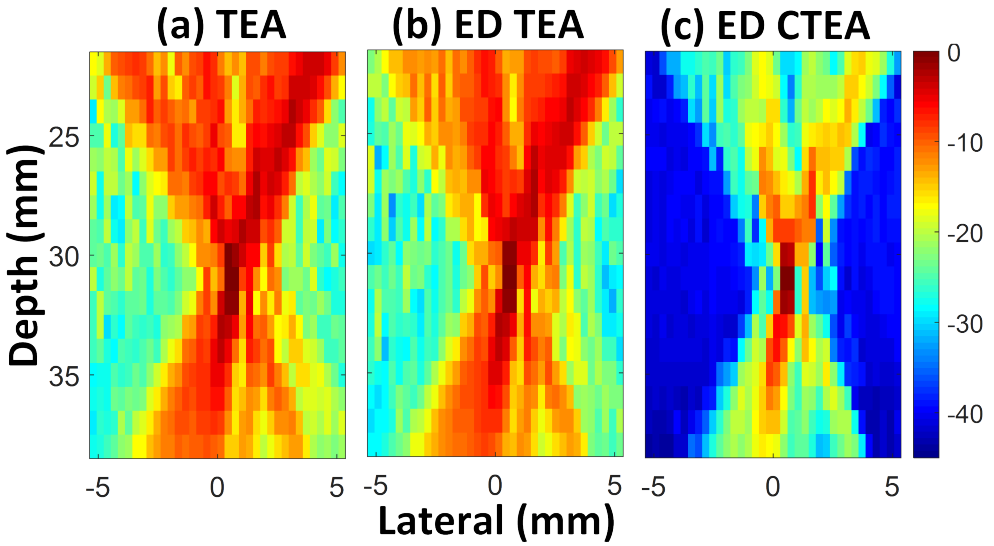

Figure 4.13: The experimental data beamformed by TEA (a), ED TEA (b), ED CTEA (c).

4.4 Discussions

An empirical constant parameter setting of F-number for the image targets at different depths might not maximally reduce the clutters, as the optimised available apertures (i.e., determined by F-number) to sum the received emissions along the hyperbolas are varied with different features (has not been clearly explained in the literature) Perrot et al. (2021), wherein the diagnostic array is one of the key factors to determine the receiving characters. Inspired by that, a pixelwise F-number strategy was developed based on one conformal nature of imaging array: element directivity, whilst the shading weight $\mathbf{w}$ was developed to reduce the width of the main lobe (i.e. that can affect the spatial resolution of the image). Adaptive beamforming methods have demonstrated the noise suppression capability for resolution improvement. However, besides the increased computation cost, the adaptive weights could largely change the original phase information of realigned RF data, which raises the concern when the phase information plays an important role, such as for Doppler applications Pouliopoulos et al. (2017, 2020). The shading weight developed by ED, which fits into the conformal nature of array that high possibly avoids the phased distortion and benefiting the resolution.

The ED modified PAM outputs in Figures 4.10, 4.12 and 4.13, particularly for

the simulated results, show that the image quality improves more in the proximal side (i.e, approximately with 4 dB increase in CNR at the depth between 5 mm and 10 mm) and loses its efficiency when depth becomes deeper. The reason for this is illustrated in Figure 4.5, where the ED at beamformed pixel (0, 1)mm is plotted in a quasi-Dirac delta geometry, and shows that as depth gets deeper, the ED becomes more flat at beamformed pixels (0, 20)mm and (0, 40)mm. When the ED are more flat with deeper depth, the selected available aperture size becomes larger and finally approaches an almost full aperture size (the discarding threshold of ED to determine the available aperture size for every beamformed pixel, as shown in Figure 4.9, which was chosen as 0.1 to find a compromise between side lobe rejection and bubble energy preservation). Therefore, the capability to reject the side lobe was gradually degraded with increasing depth. The potential clinical implementation of this proposed method could be emphasised on the HIFU therapy monitoring in superficial tissue, such as subcutaneous tumours Hectors et al. (2016); Hu et al. (2007); Yang et al. (1992); Zhang et al. (2014).

In this chapter, the ED-based DFSW strategy was introduced into TEA-related PAM, due to conventional PAM methods has more potential to be implemented for real-time monitoring. The ED modified PAM also explored the adaptive robust Capon beamformer (RCB) for cavitation monitoring. It was used to rectify the steering vector when transforming the RCB in an adaptive diagonal loading format Li et al. (2020b). The final results of rectified RCB show its superiority compared with RCB on the image quality improvement, without the concern about the depth. Further applications for the ED-based DFSW strategy for interlaced B-mode and its validations are described in section 4.6.

4.5 Conclusions

A soft-baffle element directivity model was introduced into PAM for the design of shading weights and to determine the available receiving apertures (i.e. dynamic F-number) based on the conformal nature of the diagnostic array. The simulated and experimental results have shown that the ED based DFSW strategy was more efficient on the proximal side. All these emphasise the necessity of ED modified PAM in monitoring the HIFU therapy for superficial tissues. Also, the conventional techniques based on ED TEA and ED CTEA can be implemented with real-time techniques as the next step, which enhance the potential feasibility for the clinical transformation.

4.6 Appendix

Figure 4.14 shows the interlaced B-mode beamformed by DAS (a), the ED based DFSW modified DAS (b) (ED DAS, shown in Equation 4.9), and the ED based DFSW modified coherent DAS (ED CDAS, shown in Equation 4.10) (c) (e.g., parameters' explanation in Equation 4.9 and 4.10 can be referred in Section 4.2.2). In Figure 4.15(a), there are two hyperechoic layers displayed in the interlaced B-mode: the top one is from the phantom holder, and the second is the top edge of *ex vivo* liver tissue. The dashed circle region indicates the hypergenicity phenomenon that occurred inside the HIFU focal zone. The discard threshold applied for ED DAS and ED CDAS is 0.1 as stated in PAM applications. After applying the DFSW strategy into ED DAS, as shown in Figure 4.14(b), the strong side lobes at the arrow pointing places (i.e. proximal side) were significantly suppressed relative to DAS in Figure 4.14(a). The ED CDAS in Figure 4.14(c) further improves the image quality, which can be clearly visualised by the clutter alleviation between the two hyperechoic layers.

$$I_{\text{ED DAS}}(x_0, z_0) = \sum_{n=i}^{q} \mathbf{w}\, s_n(x_0, z_0). \tag{4.9}$$

$$\begin{aligned} I_{\text{ED CDAS}}(x_0, z_0) = \Bigg(& \left[\sum_{n=i}^{q} \mathbf{w}\, sign(s_n(x_0, z_0)) \sqrt{|s_n(x_0, z_0|} \right]^2 \\ & - \sum_{n=i}^{q} \left[\mathbf{w}\, sign(s_n(x_0, z_0)) \sqrt{|s_n(x_0, z_0|} \right]^2 \Bigg). \end{aligned} \tag{4.10}$$

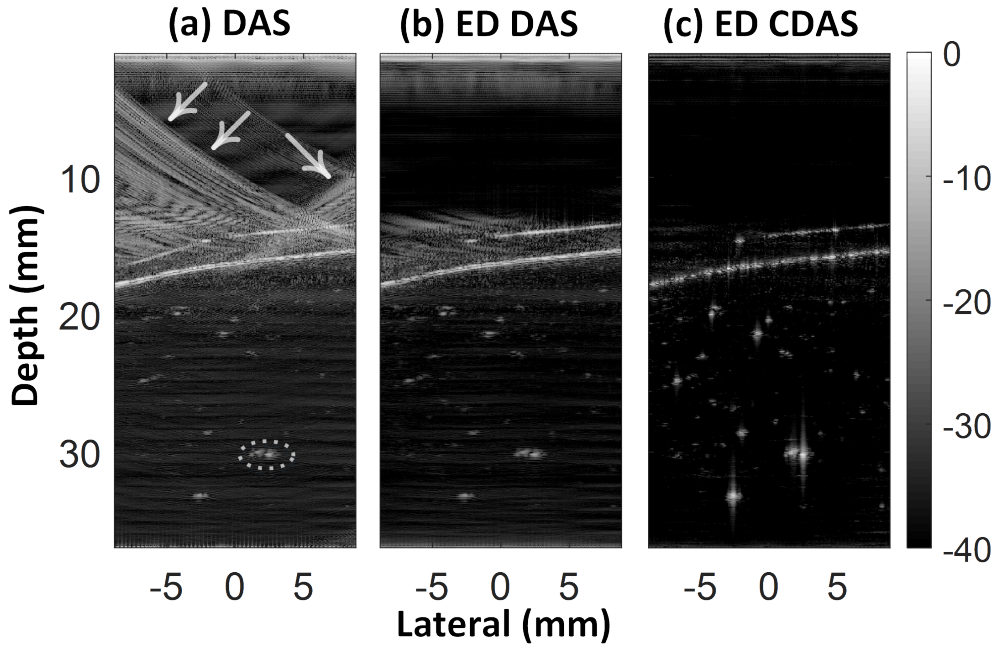

Figure 4.14: The interlaced B-mode acquired from HIFU on *ex vivo* liver tissues beamformed by DAS (a), ED DAS (b), ED CDAS (c).

Figure 4.15 shows the enlarged bottom part (i.e. distal side) of the interlaced B-mode and the rectangular areas as the CNR calculation. Comparing the ED DAS displayed in Figure 4.15(b) to the DAS in Figure 4.15(a), the noise in the horizontal stripes format (i.e. low frequency component noise, which are mostly caused by HIFU interference) and ambient noise (i.e. as indicated by the arrow point place which comes from the sonification reflections of the phantom holder bottom), were mitigated clearly. The CNR of DAS increased from 15.5dB (a) to 21dB (b) by ED DAS. The ED CDAS in Figure 4.15(c) shows an expected image quality that is better than other beamforming outputs, and its CNR reached approximately 40.1dB. It should be noted that the bandpass filter was not adopted for ED CDAS beamformer, aiming to emphasise the contribution only from the ED based DFSW strategy.

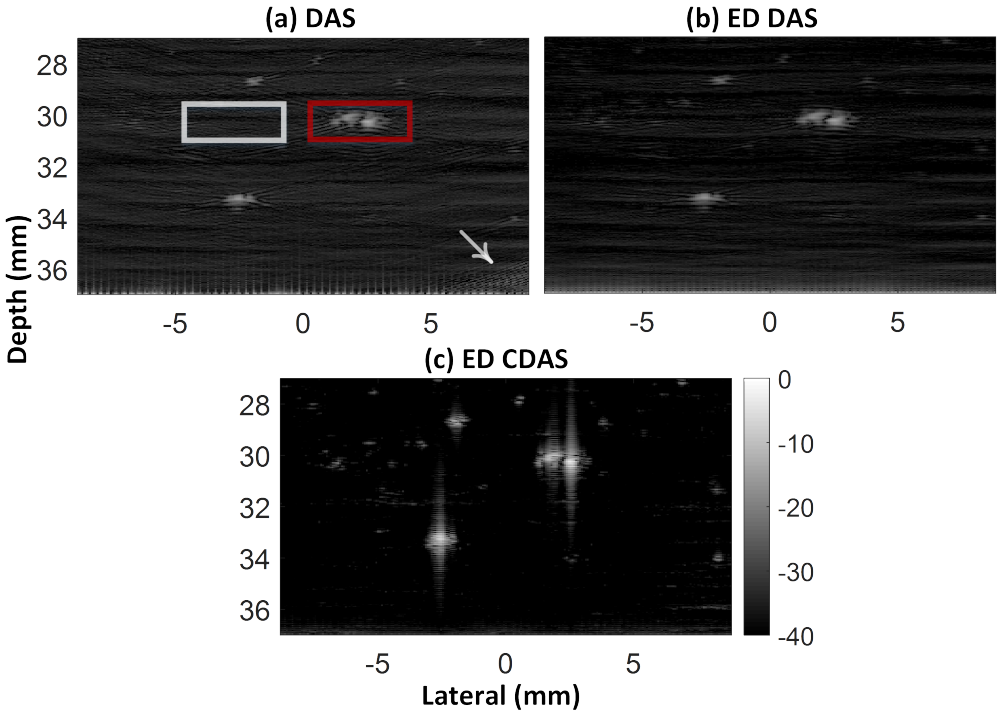

Figure 4.15: The bottom part of interlaced B-image by DAS (a), ED DAS (b), ED CDAS (c).

Chapter References

Cowell D.M., Smith P.R. and Freear S. (2013). Phase-inversion-based selective harmonic elimination (pi-she) in multi-level switched-mode tone-and frequency-modulated excitation. *IEEE transactions on ultrasonics, ferroelectrics, and frequency control*, **60**(6), pp. 1084–1097.

Destrempes F. and Cloutier G. (2010). A critical review and uniformized representation of statistical distributions modeling the ultrasound echo envelope. *Ultrasound in medicine & biology*, **36**(7), pp. 1037–1051.

Friis H.T. and Feldman C.B. (1937). A multiple unit steerable antenna for short-wave reception. *Proceedings of the Institute of Radio Engineers*, **25**(7), pp. 841–917.

Greis C. (2004). Technology overview: Sonovue (bracco, milan). *European radiology*, **14**, pp. P11–5.

Haynes W.M., Lide D.R. and Bruno T.J. (2016). *CRC handbook of chemistry and physics*. CRC press.

Hectors S.J., Jacobs I., Moonen C.T., Strijkers G.J. and Nicolay K. (2016). Mri methods for the evaluation of high intensity focused ultrasound tumor treatment: Current status and future needs. *Magnetic resonance in medicine*, **75**(1), pp. 302–317.

Hu Z., Yang X.Y., Liu Y., Sankin G.N., Pua E.C., Morse M.A., Lyerly H.K., Clay T.M. and Zhong P. (2007). Investigation of hifu-induced anti-tumor immunity in a murine tumor model. *Journal of translational medicine*, **5**(1), pp. 1–11.

Huggins E. (2007). Introduction to fourier optics. *The Physics Teacher*, **45**(6), pp. 364–368.

Jeong M.K. and Choi M.J. (2022). A novel approach for the detection of every significant collapsing bubble in passive cavitation imaging. *IEEE Transactions on Ultrasonics, Ferroelectrics, and Frequency Control*, pp. 1–1. doi: 10.1109/TUFFC.2022.3151882.

Kamimura H.A., Wu S.Y., Grondin J., Ji R., Aurup C., Zheng W., Heidmann M., Pouliopoulos A.N. and Konofagou E.E. (2020). Real-time passive acoustic

mapping using sparse matrix multiplication. *IEEE Transactions on Ultrasonics, Ferroelectrics, and Frequency Control*, **68**(1), pp. 164–177.

Li C., Clegg H.R., Carpenter T.M., Nie L., Freear S., Cowell D.M. and McLaughlan J.R. (2020a). Apodizing delay and auto-correlation reconstruction algorithm for high-frame-rate ultrasound imaging. In: *2020 IEEE International Ultrasonics Symposium (IUS)*. IEEE, pp. 1–4.

Li C., Clegg H.R., Carpenter T.M., Nie L., Freear S., Cowell D.M. and McLaughlan J.R. (2020b). Modified passive acoustic mapping with diagnostic-array angular response for cavitation monitoring during hifu ablation in ex vivo tissue. In: *2020 IEEE International Ultrasonics Symposium (IUS)*. IEEE, pp. 1–4.

Li M.L., Guan W.J. and Li P.C. (2004). Improved synthetic aperture focusing technique with applications in high-frequency ultrasound imaging. *IEEE transactions on ultrasonics, ferroelectrics, and frequency control*, **51**(1), pp. 63–70.

Lu J.y., Zou H. and Greenleaf J.F. (1994). Biomedical ultrasound beam forming. *Ultrasound in medicine & biology*, **20**(5), pp. 403–428.

Lyka E. (2016). *Passive acoustic mapping for improved detection and localisation of cavitation activity*. Ph.D. thesis, University of Oxford.

Mast T.D. (2007). Fresnel approximations for acoustic fields of rectangularly symmetric sources. *The Journal of the Acoustical Society of America*, **121**(6), pp. 3311–3322.

Morgan K.E., Allen J.S., Dayton P.A., Chomas J.E., Klibaov A. and Ferrara K.W. (2000). Experimental and theoretical evaluation of microbubble behavior: Effect of transmitted phase and bubble size. *IEEE transactions on ultrasonics, ferroelectrics, and frequency control*, **47**(6), pp. 1494–1509.

Perrot V., Polichetti M., Varray F. and Garcia D. (2021). So you think you can das? a viewpoint on delay-and-sum beamforming. *Ultrasonics*, **111**, p. 106309.

Pompei F.J. and Wooh S.C. (2002). Phased array element shapes for suppressing grating lobes. *The Journal of the Acoustical Society of America*, **111**(5), pp. 2040–2048.

Pouliopoulos A., Smith C., El Ghamrawy A., Tang M. and Choi J. (2017). Doppler passive acoustic mapping for monitoring microbubble velocities in ultrasound therapy. *The Journal of the Acoustical Society of America*, **141**(5), pp. 3491–3491.

Pouliopoulos A.N., Smith C.A., Bezer J.H., El Ghamrawy A., Sujarittam K., Bouldin C.J., Morse S.V., Tang M.X. and Choi J.J. (2020). Doppler passive acoustic mapping. *IEEE Transactions on Ultrasonics, Ferroelectrics, and Frequency Control*, **67**(12), pp. 2692–2703.

Salles S., Liebgott H., Basset O., Cachard C., Vray D. and Lavarello R. (2014). Experimental evaluation of spectral-based quantitative ultrasound imaging using plane wave compounding. *IEEE Transactions on Ultrasonics, Ferroelectrics, and Frequency Control*, **61**(11), pp. 1824–1834.

Selfridge A., Kino G. and Khuri-Yakub B. (1980). A theory for the radiation pattern of a narrow-strip acoustic transducer. *Applied Physics Letters*, **37**(1), pp. 35–36.

Skobelev S.P. (1998). Methods of constructing optimum phased-array antennas for limited field of view. *IEEE Antennas and Propagation Magazine*, **40**(2), pp. 39–50.

Smith P.R., Cowell D.M. and Freear S. (2013). Width-modulated square-wave pulses for ultrasound applications. *IEEE transactions on ultrasonics, ferroelectrics, and frequency control*, **60**(11), pp. 2244–2256.

Smith P.R., Cowell D.M., Raiton B., Ky C.V. and Freear S. (2012). Ultrasound array transmitter architecture with high timing resolution using embedded phase-locked loops. *IEEE transactions on ultrasonics, ferroelectrics, and frequency control*, **59**(1), pp. 40–49.

Tasinkevych Y., Klimonda Z., Lewandowski M., Nowicki A. and Lewin P. (2013). Modified multi-element synthetic transmit aperture method for ultrasound imaging: A tissue phantom study. *Ultrasonics*, **53**(2), pp. 570–579.

Tasinkevych Y., Trots I., Nowicki A. and Lewin P. (2012). Modified synthetic transmit aperture algorithm for ultrasound imaging. *Ultrasonics*, **52**(2), pp. 333–342.

Versluis M., Stride E., Lajoinie G., Dollet B. and Segers T. (2020). Ultrasound contrast agent modeling: a review. *Ultrasound in Medicine & Biology*, **46**(9), pp. 2117–2144.

Wettergren T.A. (2004). Element directivity compensation for beamforming a curved array. *IEEE Signal Processing Letters*, **11**(10), pp. 845–848.

Yang R., Reilly C.R., Rescorla F.J., Sanghvi N.T., Fry F.J., Franklin Jr T.D. and Grosfeld J.L. (1992). Effects of high-intensity focused ultrasound in the treatment of experimental neuroblastoma. *Journal of pediatric surgery*, **27**(2), pp. 246–251.

Zhang X., Zheng Y., Wang Z., Huang S., Chen Y., Jiang W., Zhang H., Ding M., Li Q., Xiao X. et al. (2014). Methotrexate-loaded plga nanobubbles for ultrasound imaging and synergistic targeted therapy of residual tumor during hifu ablation. *Biomaterials*, **35**(19), pp. 5148–5161.

Chapter 5

Convoluted dual modes to enhance polar coordinate PAM with the coaxial phased array setup

Passive acoustic mapping (PAM) has been implemented for cavitation localisation, quantification and detection in therapeutic ultrasound research. Having coaxial imaging and therapeutic transducers would help move this purely laboratory technique towards clinical relevance. In this chapter, a phased-array transducer was co-aligned in the middle of a single element high-intensity focused ultrasound (HIFU) transducer. Due to the limited dimensions of the imaging array, Cartesian coordinate PAM via phased array may not meet the demands of cavitation monitoring (e.g., such as for the wobbling HIFU that cavitation high possibly can be occurred inside a larger area along with the long steered beam). Therefore, polar coordinate PAM is proposed for a competent monitoring field of view in preparation for further related applications. Additionally, to address concerns about the image quality of PAM in monitoring high-duty-cycle HIFU therapy, a dual modes to mutually convoluted with each other between interlaced B-mode and PAM are discussed, following work published by Gray et al. Gray et al. (2020). Furthermore, as a hyperechoic area may occur after hundreds of sonification cycles, the A_{50} Abadi et al. (2018) of focal pressure area with the occurrence of primary cavitation activities was detected as a complementary spatial filter in the absence of hyperechogenicity in the B-mode for convolution.

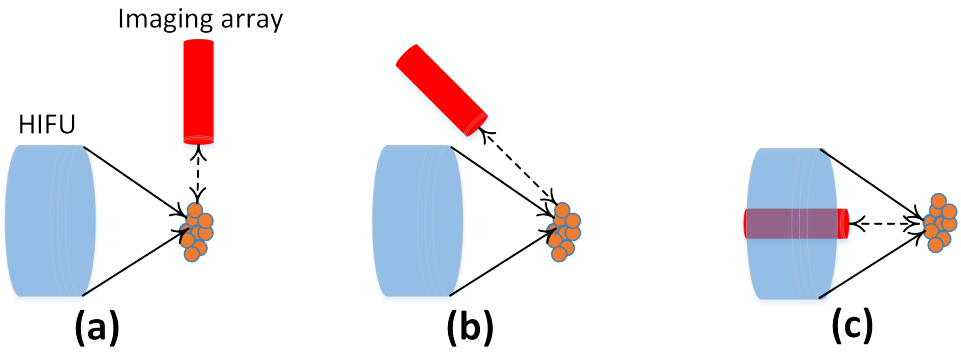

Figure 5.1: The schematic of HIFU system with different alignment geometries (a) perpendicular, (b) acute and (c) coaxial.

5.1 Introduction

Three typical ultrasound-guided high-intensity focused ultrasound (HIFU) therapy systems with different alignment geometries can be seen in the literature. First, the perpendicular arrangement sets the imaging array orthogonal to the axial of the HIFU transducer (as shown in figure 5.1(a)) Haworth et al. (2015). This system can provide a competitive lateral resolution of PAM to resolve cavitation along the HIFU axial beam. Second, the acute type may be able to achieve a compromise to take care of spatial resolution and system setting (as shown in figure 5.1(b)) Choi and Coussios (2012). The third, the coaxial setting, involves orienting the diagnostic imaging array within an acoustic window in the middle of a HIFU transducer (as shown in figure 5.1(c)) Crake et al. (2015); Kennedy et al. (2004). This setting, despite concerns about possible diagnostic system saturation from the back-scattering from HIFU sonication, could achieve better performance for a target confined in the lateral direction of the diagnostic imaging array (such as in a flowing contrast agent phantom), while providing geometric convenience for clinical applications.

Phased arrays have long been explored for the transmission and reception of sound waves in different acoustic applications, including underwater acoustics, medical imaging, ultrasonic therapy and nondestructive evaluation Pompei and Wooh (2002). In this chapter, a 64-element phased array (IP-105, Sonic Concepts, Inc., WA, USA) was coaxially aligned with a HIFU transducer (H-102, Sonic Concepts, Inc., WA, USA) for ultrasound monitoring, including interlaced B-mode and PAM, as shown in Figure 5.2. However, the PAM algorithms with Cartesian coor-

Figure 5.2: The phased imaging array and single-element therapeutic transducer used for coaxial ultrasound monitoring for HIFU therapy.

dinates to be implemented on current phased transducers, which can be possibly restricted by the limited array dimensions. Therefore, PAM with polar coordinates is desirable to facilitate a competent field of view to monitor the whole sonicated region.

Recently, Gray et al. Gray et al. (2020) suggested a way to overcome the fundamental physical limits of the conventional diagnostic array aperture that always results in point spread functions (PSFs) with axial/lateral beamwidth ratios nearly an order of magnitude greater. Two separate PAM frames were acquired simultaneously from two perpendicular imaging arrays to filter each other; this demonstrated that the spatial resolution could be better than 1 mm in both dimensions of the imaging plane. Inspired by this strategy, an alternative methods was applied which could be illustrated as the polar coordinate PAM weighted by the A_{50} of the hyperechoic area in interlaced divergent B-mode for spatial resolution improvement. Moreover, as the hyperechoic area may occur only after hundreds of sonification cycles, if at all, the A_{50} of focal pressure area with the occurrence of primary cavitation activities was detected as a complementary spatial filter in the absence of hyperechogenicity in the B-mode image Li et al. (2021a). The convenience of the proposed imaging strategy compared with the method proposed by Gray et al. (2020) is demonstrated in the following observations: the pulse–echo beamformers

used for B-mode had lower computation complexity than PAM, which reduced the computation cost of the convolution operation. Additionally, the interlaced imaging mode acquired by one diagnostic array contrasted with the dual arrays for the convolution of two PAM frames that mitigated the complexity of the monitoring system. Further discussion and validation are presented in the following sections.

5.2 Methods

5.2.1 Polar coordinate passive acoustic mapping via phased array

The simulated and experimental RF data for PAM were beamformed with all frequency components, and each integration duration was 15 μs (simulated) and 30 μs (experimental), respectively. The axial and lateral beamforming steps for the polar coordinate system are illustrated in the consequent explanations. To optimise the computation speed of the algorithms in this chapter, the implementation of PAM and interlaced B-mode were boosted via a parallel execution tool on a high-performance computer UOL (2022).

The receiving time delay τ in the polar coordinates was determined by r, as shown in Figure 5.3(a). The angle theta = θ was dependent on the lengths of z and x, such that the τ can be expressed as:

$$\tau = \sqrt{(r \times cos(\theta))^2 + (r \times sin(\theta) - x_i)^2}. \tag{5.1}$$

Equation 5.1 indicates the point (r, θ) received by element x_i: $x = r * sin(\theta)$ and $z = r * cos(\theta)$. The $beta = \beta$ in Figure 5.3(b) determines the span angle of PAM for the imaging field of view. For experimental and simulated data, the axial beamformed step along the polar line r was set as 1 mm to take into consideration about the compromise between beamforming speed and image smoothness. The lateral beamformed step was defined as 0.5^o as an interval within the span angle β. As cavitation activities generally occurred inside the predefined HIFU focal zone, the magnified region in Figure 5.3(c) can be pre-selected to benefit from either a higher frame rate or a finer lateral resolution beamformed with more narrowly spaced beams, or both. Finally, the beamformed output matrix will be adopted into polar coordinates for image display.

A simulation was performed to further describe the flexibility of polar coordinate PAM. Figure 5.4 and Figure 5.5 correspond to the images displayed in Figure 5.3(b) (flexible central span angle) and Figure 5.3(c) (close-up of the targeted re-

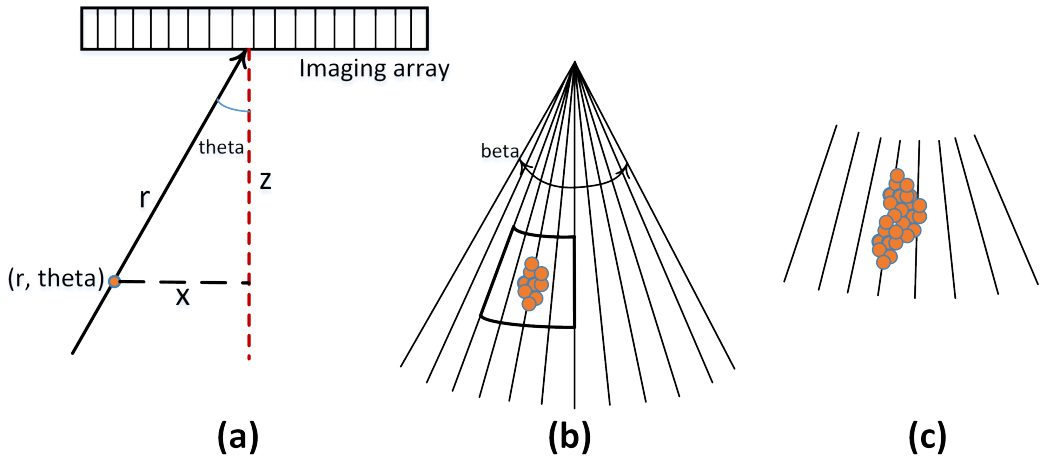

Figure 5.3: (a) Imaging plane for beamforming in polar coordinates, (b) the schematic of full-scope imaging area in polar coordinate and (c) a close-up of the targeted region.

gion), respectively. In the simulation, three scatterers were set at (-2, 18) mm, (0, 18) mm and (3, 18) mm. The sampling rate of the simulated data was 40 MHz, the imaging array was set with 64 elements and the pitch size was 0.15 mm, according to the geometric parameters of the phased array (IP-105, Sonic Concepts, Inc., WA, USA) in Figure 5.2. Each scatterer was simulated via a coated-bubble model; more details can be found in Section 4.2.1.

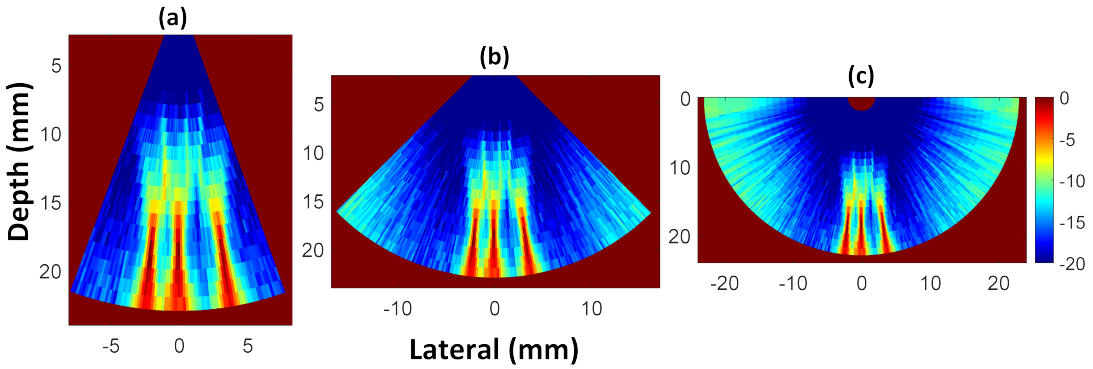

Figure 5.4: Polar coordinate PAM beamformed with different span angles (a) $\beta = 40^{o}$, (b) $\beta = 90^{o}$ and (c) $\beta = 180^{o}$.

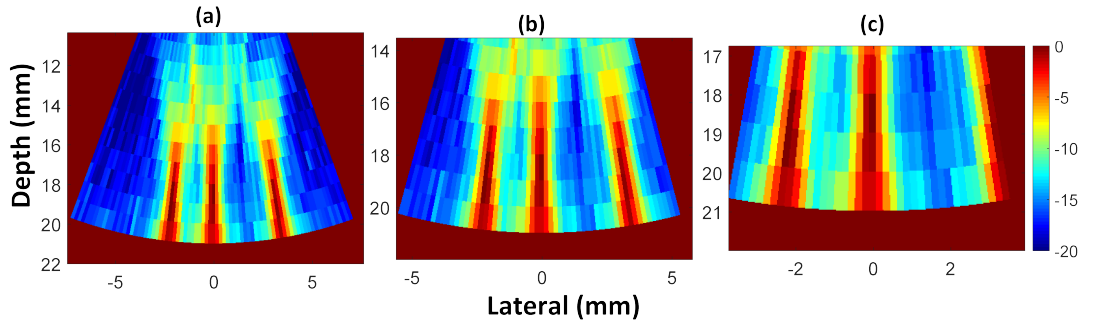

Figure 5.5: Polar coordinate PAM beamformed with different close-up area sizes (a) 972mm^2, (b) 549mm^2 and (c) 246mm^2.

5.2.2 Mutual convolution of dual modalities

An ultrasound imaging-guided therapeutic system including the Ultrasound Array Research Platform (UARP) Cowell et al. (2013); Smith et al. (2013, 2012) with a single-element HIFU transducer (H-102, Sonic Concepts, Inc., WA, USA) and a phased imaging array (IP-105, Sonic Concepts, Inc., WA, USA), was utilised for HIFU working on polyacrylamide phantom studies. The schematic coaxial setting is shown in Figure 5.6(a), the radio frequency data for PAM and B-mode were interleavingly received by the phased array with a sampling frequency 40 MHz, as illustrated in Figure 5.6(b). The total hybrid pulse duration was 5 s and its PNP was 3 MPa, more specific parameters relating to the settings in the hybrid pulse regime can be seen in Section 3.2.3.

In this chapter, interlaced B-mode and PAM were beamformed by delay-and-sum (DAS) Synnevag et al. (2007) and TEA Li et al. (2021b); Norton and Won (2000), taking into consideration the computation efficacy. The available size of hyperechogenicity, denoted by A_{50} Abadi et al. (2018), was estimated in the beamformed output matrix of the interlaced divergent B-mode then weighted on the beamformed output matrix of PAM. Additionally, the HIFU focal pressure field was defined as a complementary spatial filter for the initial stage of HIFU exposure in the possible absence of hyperechogenicity. The pressure field was measured by a National Physical Laboratory-calibrated differential membrane hydrophone (Precision Acoustics Ltd., Dorchester, UK) with an uncertainty of 14 %, and A_{50} size of the HIFU focal pressure field was estimated for weighting on PAM.

Figure 5.7 shows the schematic procedures about the implementation of the convolution of the dual modalities. Figure 5.7(a) and (b) show the spatial filters for PAM: (a) is the beamformed output matrix of the interlaced divergent B-mode (before envelope detection, log compression and polar coordinate transformation) and (b) is the HIFU focal pressure field. After extracting the A_{50} area in Figure 5.7(a) and (b) as the ROI to be convoluted with PAM (c) (A_{50} is aimed to select the ROI region for convolution, while suppressing the ambient clutters). Figure 5.7(c) is the beamformed output matrix of PAM (before log compression and polar coordinate transformation). Figure 5.7(d) is the proposed convolution result of PAM. After log compression and polar coordinate transformation, figure 5.7(d) is adapted to (e), with a flexible set about the field of view.

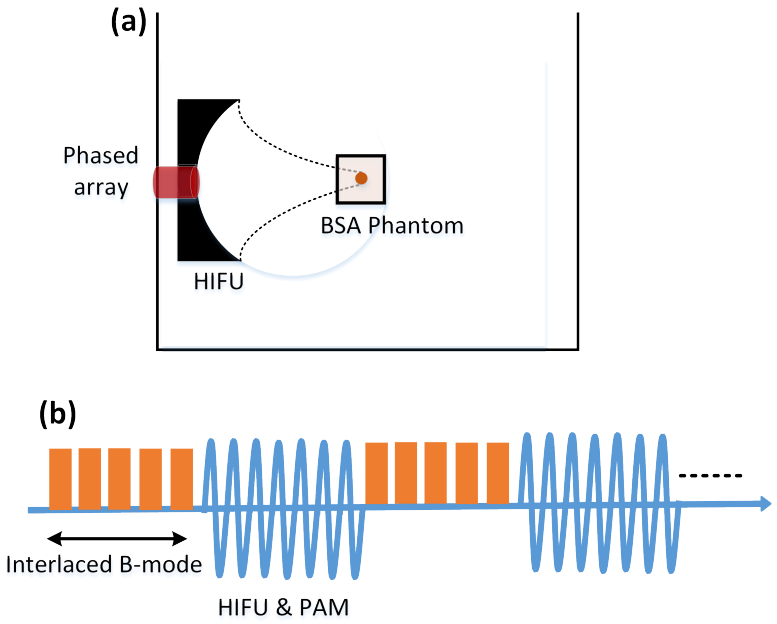

Figure 5.6: (a) Experimental setup for cavitation monitoring and (b) The hybrid pulse regimen for PAM and interlaced B-mode.

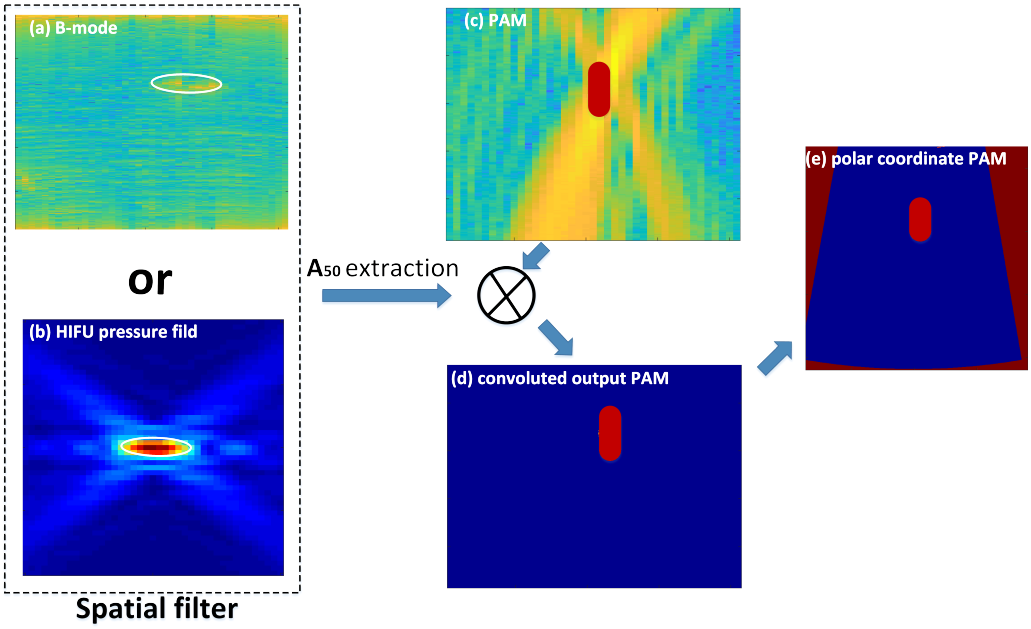

Figure 5.7: The schematic employment of the dual modality convolution strategy (the red ellipses in (c-e) indicate for the cavitation region).

5.3 Results and Discussion

5.3.1 Cartesian coordinates *versus* Polar coordinates

Figure 5.8 shows the positions of the simulated bubble scatterers. The simulated imaging array with a geometric setting follows the phased array (IP-105, Sonic Concepts, Inc. WA, USA), as illustrated in Section 5.2.1. Figure 5.9(a) shows beamforming with a full phased array in Cartesian dimensions (64 beamformed lines, lateral step of pitch size 0.15 mm and axial step of 1 mm). Figure 5.9(c) shows beamforming with span angle 31.5^o and lateral step 0.5^o (e.g., the axial step is 1 mm), so that the beamformed lines are 64 and therefore, the total beamforming time is equivalent to the Cartesian output shown in Figure 5.9(a). A comparison between Figure 5.9(a) and Figure 5.9(c) demonstrates that, with the identical total beamforming time, the polar coordinate image can contain more image targets due to the flexible central angle and the resulting flexible field of view. A wider field of view can be more convenient for monitoring unintended acoustic information from the entire sonicated field and benefit for the further exploration about the cavitation monitoring in wobbling HIFU applications, whilst the polar coordinate PAM can be flexibly adapted to the displaying of passive data acquired by different types of imaging array (phased, linear, curlinear), for the competent field of view and supporting the clinical use. However, there are concerns associated with polar coordinate display (transformation): more data storage space is needed, which raises the buffer size specification, and the lateral resolution is decreased as a function of the imaging depth and span angle, as illustrated by a comparison of Figure 5.9(b) and Figure 5.9(d), due to the peculiarity of polar coordinates.

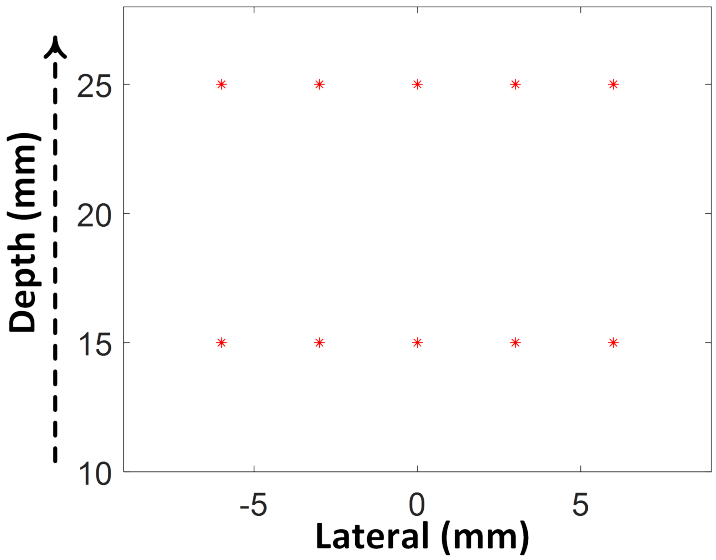

Figure 5.8: The positions of the simulated point spread functions.

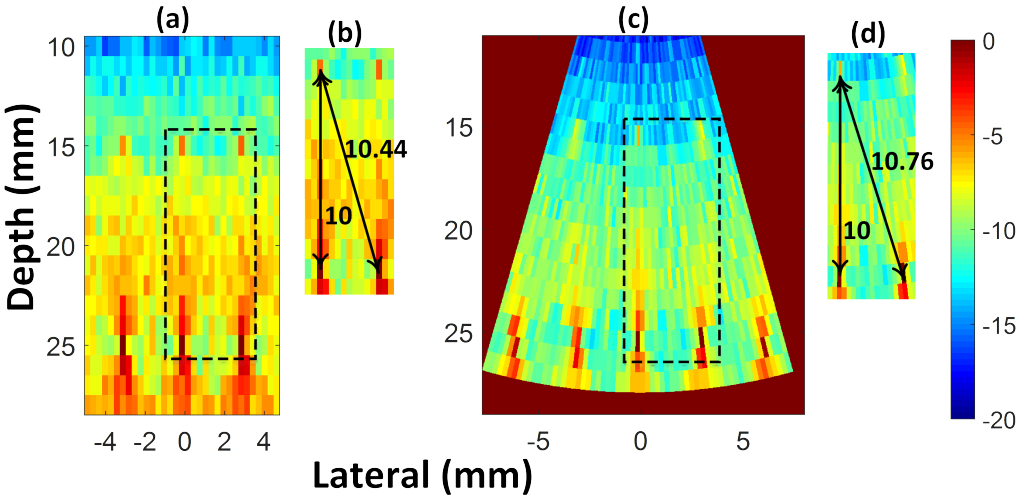

Figure 5.9: The simulated point spread functions beamformed in Cartesian coordinates: the rectangular region marked by the broken line in (a) is displayed in (b) and polar coordinates: the rectangular region marked by the broken line in (c) is displayed in (d).

5.3.2 Proposed convoluted output

Figure 5.10, showing the PAM output, demonstrates that the axial elongated region in (a) is reduced by a magnitude of one to two in (b) after convolution. When compared with the dual array for PAM monitoring Gray et al. (2020), several advantages can be observed. Due to the coaxial setting, the geometry is fixed and the varied experimental parameters, such as the distance between the imaging source and imaging array, and the angle between the HIFU transducer and the diagnostic array, are kept constant; it may, therefore, be easier to identify trends and sensitivities of the cavitation sources in the final PAM output. Moreover, the B-mode reduces the computation load of the convolution operation, and single diagnostic array for PAM and B-mode that reduced the system complexity and cost of the dual array.

However, several concerns related to the proposed strategy should be considered. The B-mode used for the spatial filter due to the energy difference with PAM (i.e. B-mode is an envelope-based output, whereas PAM is the output based on the integration of intensity bins), which determines the final convoluted output, suffers an energy difference when compared with the original PAM output. Therefore, this strategy is more suitable for the localisation of suspected cavitation than for the quantitative interpretation of cavitation energy.

Also, when to switch the spatial filter between the interlaced B-mode and focal pressure field gives rise to uncertainty about the proposed convolution strategy. Hyperechogenicity in interlaced B-mode may occur later than the information of suspected cavitation displayed by PAM. Therefore, the HIFU focal pressure field was detected and employed as a complementary spatial filter for the initial HIFU stage, but what is the optimal moment to switch them for filtering which is varied based on different thermal applications. Moreover, the later occurrence of the hyperechogenicity in B-mode and the possible migration of cavitation activities displayed by PAM could facilitate the asynchronous possibility (spatially and temporally) for the convolution between dual modes. The solution in future research would be to divide the HIFU exposure into more segments for hybrid ultrasound monitoring while keeping an identical duty cycle of 95%, thus maximising the synchronisation of the hyperechogenicity in B-mode for PAM filtering. Also, the implementation of the proposed convolution strategy for cavitation-involved or non-thermal HIFU therapy will be relatively simple, as in B-mode, there is a high probability of hyperechogenicity occurring throughout the whole therapy pro-

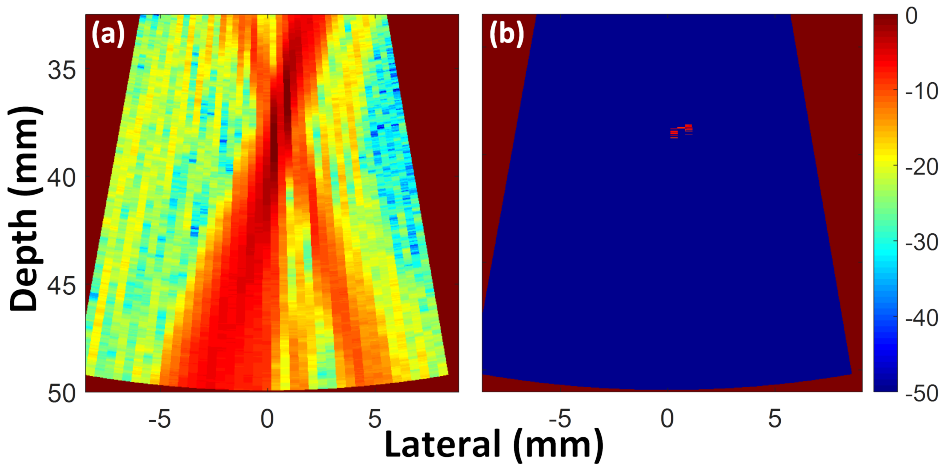

Figure 5.10: Polar coordinate PAM (a) beamformed by TEA and (b) after the proposed convolution strategy.

cess, for example, in non-thermal applications Arvanitis et al. (2016); Jones et al. (2020), drug delivery Choi et al. (2014); Paverd et al. (2019); Stride and Coussios (2019) and experiments involving contrast agents Abadi et al. (2018); Haworth et al. (2012).

Another concern is the operation of the proposed strategy in three-dimensional. The influence of the reverberation of the bubble cluster in the elevation direction may facilitate more stochastic and chaotic artefacts in PAM and interlaced B-mode, and therefore gain more uncertainty about the final output of the dual modes' convolution. Such concern again raises the necessity to enable three-dimensional PAM via a matrix transducer, with the aim of testing the proposed strategy through row–column B-mode and PAM imaging. One more related scenario, about the 3D monitoring of wobbling HIFU therapy via a multi-element therapeutic transducer and the coaxial matrix diagnostic array setup, particularly for the monitoring of steered therapeutic beam along the lateral/axial direction which required the competent monitored area for the possible occurrence of cavitation activities. The proposed convolution strategy with 3D polar coordinate PAM and 3D divergent mode B-mode as the next step can be a promising way for source localisation in the entire wobbling therapeutic field. Consequently, to ensure the real-time monitoring feature, a parallel executed beamformer on a high-performance computer with decimation for sparse array Inerfield et al. (2002) and sparse matrix-based GPU techniques Grondin et al. (2015); Hou et al. (2014);

Kamimura et al. (2020) are expected.

5.4 Conclusions

The contributions made in this chapter can be summarised as follows: The perpendicular setting was updated into a coaxial geometry more closely approximating the clinical experimental geometry. A polar coordinate PAM was developed with a flexible set field of view, which is more convenient for monitoring acoustic information from the entire sonicated field. Finally, a dual-modality convolution strategy with a significantly improved axial resolution was proposed for the localisation of suspected cavitation. All of these offer the potential to accelerate the translation of experimental ultrasound monitoring into clinical use for therapeutic ultrasound applications.

Chapter References

Abadi S.H., Haworth K.J., Mercado-Shekhar K.P. and Dowling D.R. (2018). Frequency-sum beamforming for passive cavitation imaging. *The Journal of the Acoustical Society of America*, **144**(1), pp. 198–209.

Arvanitis C.D., Vykhodtseva N., Jolesz F., Livingstone M. and McDannold N. (2016). Cavitation-enhanced nonthermal ablation in deep brain targets: feasibility in a large animal model. *Journal of neurosurgery*, **124**(5), pp. 1450–1459.

Choi J.J., Carlisle R.C., Coviello C., Seymour L. and Coussios C.C. (2014). Non-invasive and real-time passive acoustic mapping of ultrasound-mediated drug delivery. *Physics in Medicine & Biology*, **59**(17), p. 4861.

Choi J.J. and Coussios C.C. (2012). Spatiotemporal evolution of cavitation dynamics exhibited by flowing microbubbles during ultrasound exposure. *The Journal of the Acoustical Society of America*, **132**(5), pp. 3538–3549.

Cowell D.M., Smith P.R. and Freear S. (2013). Phase-inversion-based selective harmonic elimination (pi-she) in multi-level switched-mode tone-and frequency-modulated excitation. *IEEE transactions on ultrasonics, ferroelectrics, and frequency control*, **60**(6), pp. 1084–1097.

Crake C., de Saint Victor M., Owen J., Coviello C., Collin J., Coussios C.C. and Stride E. (2015). Passive acoustic mapping of magnetic microbubbles for cavitation enhancement and localization. *Physics in Medicine & Biology*, **60**(2), p. 785.

Gray M.D., Elbes D., Paverd C., Lyka E., Coviello C.M., Cleveland R.O. and Coussios C.C. (2020). Dual-array passive acoustic mapping for cavitation imaging with enhanced 2-d resolution. *IEEE Transactions on Ultrasonics, Ferroelectrics, and Frequency Control*, **68**(3), pp. 647–663.

Grondin J., Payen T., Wang S. and Konofagou E.E. (2015). Real-time monitoring of high intensity focused ultrasound (hifu) ablation of in vitro canine livers using harmonic motion imaging for focused ultrasound (hmifu). *JoVE (Journal of Visualized Experiments)*, (105), p. e53050.

Haworth K.J., Mast T.D., Radhakrishnan K., Burgess M.T., Kopechek J.A., Huang S.L., McPherson D.D. and Holland C.K. (2012). Passive imaging with

pulsed ultrasound insonations. *The Journal of the Acoustical Society of America*, **132**(1), pp. 544–553.

Haworth K.J., Salgaonkar V.A., Corregan N.M., Holland C.K. and Mast T.D. (2015). Using passive cavitation images to classify high-intensity focused ultrasound lesions. *Ultrasound in medicine & biology*, **41**(9), pp. 2420–2434.

Hou G.Y., Provost J., Grondin J., Wang S., Marquet F., Bunting E. and Konofagou E.E. (2014). Sparse matrix beamforming and image reconstruction for 2-d hifu monitoring using harmonic motion imaging for focused ultrasound (hmifu) with in vitro validation. *IEEE transactions on medical imaging*, **33**(11), pp. 2107–2117.

Inerfield M., Lockwood G.R. and Garverick S.L. (2002). A sigma-delta-based sparse synthetic aperture beamformer for real-time 3-d ultrasound. *IEEE transactions on ultrasonics, ferroelectrics, and frequency control*, **49**(2), pp. 243–254.

Jones R.M., McMahon D. and Hynynen K. (2020). Ultrafast three-dimensional microbubble imaging in vivo predicts tissue damage volume distributions during nonthermal brain ablation. *Theranostics*, **10**(16), p. 7211.

Kamimura H.A., Wu S.Y., Grondin J., Ji R., Aurup C., Zheng W., Heidmann M., Pouliopoulos A.N. and Konofagou E.E. (2020). Real-time passive acoustic mapping using sparse matrix multiplication. *IEEE Transactions on Ultrasonics, Ferroelectrics, and Frequency Control*, **68**(1), pp. 164–177.

Kennedy J., Wu F., Ter Haar G., Gleeson F., Phillips R., Middleton M. and Cranston D. (2004). High-intensity focused ultrasound for the treatment of liver tumours. *Ultrasonics*, **42**(1-9), pp. 931–935.

Li C., Clegg H.R., Carpenter T.M., Nie L., Freear S., Cowell D.M. and McLaughlan J.R. (2021a). Mutual convolution of dual modes to enhance passive acoustic mapping for high duty-cycle hifu exposures monitoring. In: *2021 IEEE International Ultrasonics Symposium (IUS)*. IEEE, pp. 1–4.

Li C., Clegg H.R., Carpenter T.M., Nie L., Freear S., Cowell D.M. and McLaughlan J.R. (2021b). Polar coordinate coherent passive acoustic beamforming for the modifiable improvement of image quality and field of view. In: *2021 IEEE International Ultrasonics Symposium (IUS)*. IEEE, pp. 1–4.

Norton S.J. and Won I. (2000). Time exposure acoustics. *IEEE Transactions on Geoscience and Remote Sensing*, **38**(3), pp. 1337–1343.

Paverd C., Lyka E., Elbes D. and Coussios C. (2019). Passive acoustic mapping of extravasation following ultrasound-enhanced drug delivery. *Physics in Medicine & Biology*, **64**(4), p. 045006.

Pompei F.J. and Wooh S.C. (2002). Phased array element shapes for suppressing grating lobes. *The Journal of the Acoustical Society of America*, **111**(5), pp. 2040–2048.

Smith P.R., Cowell D.M. and Freear S. (2013). Width-modulated square-wave pulses for ultrasound applications. *IEEE transactions on ultrasonics, ferroelectrics, and frequency control*, **60**(11), pp. 2244–2256.

Smith P.R., Cowell D.M., Raiton B., Ky C.V. and Freear S. (2012). Ultrasound array transmitter architecture with high timing resolution using embedded phase-locked loops. *IEEE transactions on ultrasonics, ferroelectrics, and frequency control*, **59**(1), pp. 40–49.

Stride E. and Coussios C. (2019). Nucleation, mapping and control of cavitation for drug delivery. *Nature Reviews Physics*, **1**(8), pp. 495–509.

Synnevag J.F., Austeng A. and Holm S. (2007). Adaptive beamforming applied to medical ultrasound imaging. *IEEE transactions on ultrasonics, ferroelectrics, and frequency control*, **54**(8), pp. 1606–1613.

UOL (2022). High performance computer cluster. https://arcdocs.leeds.ac.uk/welcome.html.

Chapter 6

Conclusions and Future Research

In this thesis, we have explored different algorithms for hybrid ultrasound modalities (verified by own set of simulated and experimental data) and applied for HIFU monitoring, which focused on interlaced high frame rate B-mode imaging and passive acoustic mapping.

For the final chapter, the overall conclusions of the research are summarised and presented following the thesis objective and outline in Section 1.4. Moreover, further suggestions and validation to inspire and warrant future studies as the next step are also discussed.

6.1 Conclusions

In chapter 2, three aspects of the foundational work with study details were investigated for the next few chapters including B-mode modality, the duty cycle of quasi continuous-wave HIFU exposure and an optimal beamforming technique for interlaced B-mode. The HIFU system in this thesis was finally implemented using clinically relevant geometry: the phased diagnostic array coaxial with a HIFU transducer. The interlaced B-mode acquired by phased array could raise two concerns about the monitoring of hyperechogenicity related to the image quality of high frame rate interlaced B-mode and its field of view. The phenomenon of hyperechogenicity always has a strong connection with the occurrence of boiling bubbles, particularly in a large population. Hence, catching the transient behaviours of bubble clusters during the interval of HIFU off and B-mode would be critical for a full analysis of the imaged hyperechogenicity in each specific HIFU trial. The plane wave as an ultrafast emerging imaging technique was considered for the rapid cavitation activities. However, the unfocused transmission feature would result in an unsatisfactory signal-to-noise ratio, consequently, the coherent compounding strategy was introduced to complement the plane wave to improve the final image quality. Additionally, considering the limited physical dimension of the phased array (64 elements and the pitch size is 0.15 mm), the divergent mode was further combined with coherent compounding techniques for the finer field of view. Finally, the linear, coherent plane wave, divergent and coherent divergent modes were tested using a consistent data acquisition time and demonstrated the coherent divergent mode to be the optimal choice.

The HIFU duty cycle is one of the key factors in determining correlated therapy bioeffects. The HIFU off period for duty cycles is composed of data acquisition time of the coherent compounding B-mode and a time gap (1ms). The time gap is aimed at minimising the interference of the HIFU beam in interlaced B-mode while potentially may sacrifice the hyperechogenicity evolution information. Finally, HIFU exposure fired with groups of duty cycles (80% - 100%) was tested on transparent polyacrylamide and BSA phantoms, and each duty cycle was repeated three times with groups of peak negative pressure (1.43 MPa, 1.69 MPa, 1.92 MPa, 2.13 MPa, and 2.34 MPa). The final thermal performance of each repeat was confirmed by the lesion size captured with an optical microscope, and duty cycle 95% was demonstrated to have the best compromise between thermal size and time for interlaced coherent compounded B-mode.

Even though the time gap was set, the residual interference in the interlaced B-mode could still be observed, which motivated the new beamforming technique for noise suppression and resolution improvement. The spectrum equalisation technique is essentially a whitening transformation projection that flattens the re-aligned spectral response within the bandwidth of interest, and in the time domain, the target could theoretically be formed as a quasi-Dirac shape and therefore, improve the spatial resolution. The proposed method whitened in the frequency domain that demonstrated the simulated results with an approximate 8% improvement in lateral resolution and an approximate 69% and 125% increase in the contrast-to-noise ratio and contrast-ratio with experimental data relative to the delay-multiply-and-sum algorithm. Consequently, each steered image can be improved and then reduced the total steered number for compounded output, finally minimise the HIFU-off time and ensure the HIFU thermal efficacy with best.

In chapter 3, an optimal time-domain PAM beamformer based on the robust Capon algorithm was developed that was mainly related to the reduction in the DC components generated by the beamforming process that could be recursively accumulated into strong background noise and diminish the whole image quality. Types of adaptive beamformers combined with robust Capon techniques, including Eigen-subspace and scaled Wiener methods, were also presented. The aim was to mitigate the residual interference displayed by robust Capon-based PAM, particularly in the axial direction. The final results were validated by using gel phantom and *ex vivo* liver phantoms with more complex tissue structures.

The performance of different beamformers was firstly compared in gel phantom. The passive emission was demonstrated without the ultrasound platform being saturated, which ensured no artificial broadband emission was generated for the inertial cavitation monitoring. Then, the HIFU pressure field was measured to outline the focal zone where the primary cavitation activities occurred, and the peak negative pressure of 7 MPa, which has a relatively more significant inertial bubble phenomenon, was selected for the algorithm comparison that followed. Robust Capon subtracting DC component-based PAM demonstrated more than a 100 dB improvement compared with other beamforming techniques. However, the improvement in metrics was illustrated to be changed depending on the RF data precision setting. A similar trend in the proposed method was observed in the *ex vivo* liver experiments. Additionally, the Eigen-subspace and scaled Wiener-based robust PAM achieved similar performances, explained by both of their outputs being close to the real signal power when the power of the signal subspace is much

larger than the power of the noise subspace. Finally, the parallelisation of the PAM algorithm with multi-cores of central processing units or a graphics processing unit was discussed in terms of higher frame rate for the real-time source localisation.

In chapter 4, the modified element directivity model that was considered a 'referee' in determining the pixelwise F-number, while, the normalised coefficients of the element directivity model for each pixel was applied as weighting vectors. The aims of this research are straightforward; the optimal pixelwise F-number would reject the side lobes and, therefore, improve the signal-to-noise ratio. Simultaneously, the normalised coefficients of the element directivity model could appeal to the intrinsic characteristic of the diagnostic array and maximally maintain the phase information while suppressing noise interference.

The final results were demonstrated in simulation with single point scatterer and bubble clusters at different depths, indicating that the element directivity plays a major role in the near field (i.e., at a depth of 5 mm to 10 mm). At a depth of around 5 mm, the contrast-to-noise ratio of element directivity modified TEA improved by approximately 4 dB compared with TEA in both simulation settings. At deeper depths, the impact of element directivity lost its efficiency. This is further verified by the *ex vivo* liver data; the cavitation activities occurred at a depth of approximately 31 mm, and the performance of TEA and the element directivity modified TEA are nearly identical to each other. This phenomenon occurred due to the element directivity becoming flattened with depth; therefore, the available aperture size became larger and lost the efficient ability to reject the side lobes. Further relevance of PAM source localisation considering the element directivity would be expected in monitoring, such as the transcranial therapy, where the reflection from the skull and phased aberrations disturbance factors could generally cause a non-negligible near-field noisy phenomenon for imaging.

Finally, in chapter 5, based on the clinically relevant experimental setting that used a phased array coaxially mounted in the middle of the HIFU transducer, the first concern was the limited physical dimension of the phased array, 64 elements and small pitch size. Therefore, the PAM was beamformed using a polar coordinate system and demonstrated with equivalent beamforming time, the field of view of the polar coordinate PAM was nearly two times that of the Cartesian coordinate PAM due to the flexible central angle. The subsequent problem regarding the polar coordinate transformation was illustrated; the lateral resolution could degrade a bit with depth grows. Additionally, a strategy was proposed to improve the PAM localisation capability for cavitation. The A_{50} of hyperechogenicity in

the interlaced B-mode was first extracted with two aims: to suppress the ambient noise in the B-mode, and then to apply the A_{50} area of interest to weight on the PAM, whilst the B-mode and PAM were beamformed with, respectively, DAS and TEA, with the simplest computation complexity and then boosted via the paralleled running tool in MATLAB. The final convoluted PAM results were observed with improved resolution; however, several concerns should be considered such as the energy difference between the interlaced B-mode and PAM, which could result in the energy loss of final convoluted PAM output. Therefore, this strategy is only suitable for the localisation of cavitation sources, and not for quantitative analysing of cavitation does calculation. Further *ex vivo* and *in vivo* experiments with the proposed strategy could be implemented with cavitation-involved HIFU experiments and hence, the spatial location of hyperechogenicity could be maximally synchronised with the cavitation sources and result in an accurate convoluted output.

6.2 Future Research

This thesis is dedicated to the feasibility of HIFU monitoring via passive and active acoustic mapping, and various related results have been illustrated that could stimulate points for future studies, which are summarised below.

Chapter 2 investigated many parameters of hybrid exposure (e.g., duty cycle (95%) .etc) based on the groups of testing on the polyacrylamide and BSA phantoms as the basis for the study detailed in this thesis. However, it should be noted that such parameters could be varied for different applications with complex tissue characteristics (e.g., inhomogeneousity, attenuation and diffraction). Therefore, further experimentation is required to validate these initial parameter settings based on each specific scenario. Chapter 3 detailed a data-adaptive PAM beamformer with an enhanced spatial resolution achieved by subtracting the recursively accumulated DC components in the time domain, termed RCB-DC, and the results were verified in gel and *ex vivo* liver phantoms. A complementary study to further validate the localisation ability of RCB-DC-based PAM could be achieved by simulation work (presented in chapter 4). In the simulation, the single scatterer could be defined and illustrated as either the inertial or stable cavitated source to estimate the ultimate limit of spatial resolution of RCB-DC-based PAM and hence, could be compared with the theoretical resolution limits of PAM achieved by the linear array. Also, the simulated cavitation cluster could be set with a varied number of bubbles (such as in chapter 4, 20 bubbles are randomly distributed inside a circle with a 2 mm radius) in order to quantitatively verify the different level of influence on PAM to map and distinguish types of cavitation sources, whilst providing an already known ground truth to ensure the PAM beamformer has excellent noise-mitigation capability without over-suppression.

The accuracy of modified element directivity model applied in chapter 4 is expected to be tested by more experimental work as the next step, including the verification of the actual element directivity coefficients of the linear, phased and curve-linear arrays, and the validation of the difference between the theoretical values and experimental coefficients. Then, the experimental results can be considered in PAM and used to improve the monitoring efficacy of ultrasound therapy, such as in the scenarios of a subcutaneous tumour or a microbubble-mediated blood–brain barrier opening, where the near-field image quality is important. Additionally, the PAM simulator presented in this chapter can be enhanced by incorporating more factors, such as attenuation and diffraction, in order to simulate

the more complicated spatial response of multi-featured tissue structures. Another step is to update the Fresnel–Kirchhoff diffraction of diagnostic array response into three dimensions and provide three-dimensional standardised simulated data for the quantitative analyses of row-column PAM images. One more added value of simulation is about the key parameter practice such as the ϵ in RCB-based PAM. Numerous trials of ϵ for each corresponding simulated situation (e.g., the various uncalibrated array situations) could be conducted and hence, offer the choice of pre-optimised values of ϵ for parameter settings in experimental work.

Finally, the validation of the beamforming ability of interlaced B-mode and PAM can be further demonstrated with the RF data acquired by the clinically relevant system (in chapter 5) for more specific applications. Meanwhile, the receiver operating characteristic analysis should be achieved for an approximate array calibration and generate the transformation coefficients of each array element so that the PAM can be presented with the actual energy unit. Currently, all the beamforming algorithms are two-dimensional, revealing cavitation behaviours in the lateral and axial directions. A three-dimensional beamformer is needed to provide the information in the elevation direction and facilitate a full-scope illustration of the stochastic and chaotic characteristics of cavitation activities. The consequent high computation demand requires the beamforming algorithms (active and passive) to run in parallel via multi-cores of the central processing units or a graphics processing unit for real-time monitoring. Moreover, all the beamformers in this thesis are programmed in the time domain, as it is more convenient to implant the time domain techniques into the house-developed ultrasound array research platform. However, complex tissue structures can cause changes in the speed of sound during propagation, and this phenomenon is more significant for transcranial imaging. A time-domain beamformer cannot efficiently account for the phase changes (displayed as a change in the speed of sound), which raises concerns regarding the frequency domain beamformer or the beamforming techniques, with complex weighting for the correction of phase dispersion as the next step to meet more restricted *in vivo* conditions.